BIORESORBABLE INTRACRANIAL PRESSURE SENSORS FOR CLINICAL APPLICATIONS

BY

JIHO SHIN

DISSERTATION

Submitted in partial fulfillment of the requirements
for the degree of Doctor of Philosophy in Chemical and Biomolecular Engineering
in the Graduate College of the
University of Illinois at Urbana-Champaign, 2018

Urbana, Illinois

Doctoral Committee:

Professor Paul J. A. Kenis, Chair
Professor John A. Rogers, Director of Research
Professor Hyunjoon Kong
Professor Hong Yang

ABSTRACT

Monitoring pressure in organ systems such as the brain, eye, and blood vessels form an essential diagnostic basis for assessment of patient health and progression of diseases such as traumatic brain injury, hydrocephalus, glaucoma, and hypertension. Conventional sensor technologies designed for precise, continuous monitoring of pressure are available in the form of accurate, implantable devices that must be surgically extracted after use, the procedures of which are costly and can expose the patient to significant pain and risks for complications. These permanent electronic hardware may also act as a nidus for infection, via biofilm formation along percutaneous wires, and provoke immune-mediated inflammatory responses. Here, we report materials, device structures, and fabrication strategies for bioresorbable pressure sensors, in which all of the constituent materials dissolve in biofluids over well-defined periods of time, with biologically benign end products, that can address these disadvantages.

ACKNOWLEDGEMENTS

I would like to thank my advisor, Prof. John A. Rogers, for giving me the opportunity to work in his group and for guiding and inspiring me throughout the years, to improve both as a researcher and as a person. It was an honor to work with him for so many years, which presented some of the most challenging moments of my life. I'm grateful for the times here and will remember them for the rest of my life. I would like to express my sincere gratitude to my committee members, Dr. Paul J. A. Kenis, Dr. Hong Yang, and Dr. Hyun-Joon Kong for providing me with invaluable comments and guidance for the direction of my research.

My research wouldn't have been possible without help of others. I'd like to express my gratitude to collaborators, Dr. Ying Yan and Dr. Wilson Z. Ray in Washington University School of Medicine in St. Louis for their efforts to achieve surgical and experimental perfection. I thank undergraduate students Minseok, Yechan, Jonathan, and Hangyu for their hard work. I'm grateful to group members, Dr. Wubin Bai, Dr. Seung-Kyun Kang, Dr. Daeshik Kang, Dr. Gun Chul Shin, Dr. Jang Yeol Yoon, Dr. Yoon Kyeung Lee, and Sang Min Won for their advice and inspiration every day.

My sincere gratitude goes to my parents, Dr. Hyung-Shik Shin and Dr. Hye-Won Cho, for their unconditional love and support throughout my life. I especially thank my fiancé Yun-Hee Kim for her understanding, friendship, and encouragement throughout my Ph.D. years. Her constant support and advice helped me endure through the most difficult times. Lastly, I thank God for giving me health, wisdom, friendship, and love.

To my parents and family, for their love and support

TABLE OF CONTENTS

INTRODUCTION

Bioresorbable, Implantable Devices

A defining characteristic of modern silicon electronics is its ability to remain physically invariant almost indefinitely. An emerging class of technology known as 'transient electronics' demonstrates the opposite behavior; here, all of the components completely disappear at prescribed times and controlled rates when exposed to water or biofluids[1-10]. Fabrication of such devices involve biodegradable electronic materials such as nanomembranes of monocrystalline silicon (semiconductors), magnesium (metals), and silicon dioxide (insulators) and polymers such as poly(lactic-co-glycolic acid) (PLGA; device substrates), the degradation of which yield biocompatible end products. Recently published examples of transient electronics include circuits[3], radios[9], and power supply systems[3,10] for physical sensors of pressure, temperature, flow rate, and motion[6], chemical sensors[1,6], thermal actuators[3,9], and controlled drug-delivery vehicles[1,7] for use in areas of the body such as the intracranial space, abdominal cavity, intramuscular regions of the lower extremity, and subdermal implantation at the dorsolateral area[3,6,8].

The transient behavior of these devices enables potential application possibilities that cannot be addressed with conventional electronics. Examples include environmental sensors that dissolve via exposure to moisture over time to eliminate the need for recovery, consumer electronic devices that naturally decompose to minimize costs and health risk associated with recycling and management of waste streams, and implantable diagnostic and therapeutic devices that naturally resorb (i.e. become disintegrated, then absorbed) in the body after clinically useful

timeframes to minimize costs and risks of complications associated with surgical extraction procedures.

Bioresorbable, implantable devices capable of active sensing, electronic processing, communication and/or actuation within the body are of particular interest, as they represent an unaddressed technological opportunity in which they can, in some cases, replace conventional technologies only available in the form of permanent hardware, such as deep brain electrical stimulators[11], cardiac pacemakers[12], programmable drug delivery systems[13], and pressure monitoring systems[14], as examples. The devices may operate for some finite periods of time, as defined by management and healing process of a disease, after which they resorb to eliminate unnecessary device load to avoid surgical extraction.

Intracranial Pressure Monitoring

Monitoring of pressures in various organ systems in the body such as the brain[14], eye[15], blood vessels, abdomen[16], and bladder[17] have proven clinical utility in diagnosis and management of traumatic brain injury, glaucoma, hypertension, abdominal compartment syndrome, and neurogenic bladder hypertension, respectively. Among these, intracranial pressure (ICP) monitoring is of particular interest due to the clinical impact of traumatic brain injury (TBI). Defined as sudden damage to the brain caused by a blow or jolt to the head, commonly caused by car or motorcycle crashes, sports injuries, and assaults, TBI is the leading cause of death and disability among people aged 1 to 44, responsible for the death and hospitalization of 50,000 and 235,000 Americans respectively every year[11].

Clinicians typically employ ICP monitoring techniques throughout clinical, surgical, and rehabilitation steps for patients with severe TBI[18]. Capabilities in precise, continuous monitoring

of pressure by invasive monitoring techniques using implantable biomedical devices can, therefore, be critically important in defining treatment protocols that decrease the rate of morbidity and increase the pace of recovery[15,19,20]. Conventional, standard permanent electronic hardware, however, acts as a nidus for infection: bacteria form biofilms along percutaneous wires, or seed haematogenously, with the potential to migrate within the body and to provoke immune-mediated pathological tissue reactions[21,22]. The associated surgical retrieval procedures, meanwhile, subject patients to the distress associated with re-operation and expose them to additional complications[23]. Electronic devices that naturally resorb/dissolve in biofluids provide the ultimate solution to these problems, thus motivating the research on bioresorbable pressure monitors.

Overview of Thesis

Chapter 1 describes recent study on bioresorbable implantable silicon sensors for monitoring ICP, with wireless data and power communication capabilities in both fully and partially implantable platforms. *In vitro* hydrolysis studies demonstrate complete disappearance of the device structures over time in simulated biofluids. *In vivo* demonstrations in rats illustrate capability to continuously monitor ICP up to 3 days.

Chapter 2 describes unpublished (recently submitted) work on bioresorbable ICP monitors with thermally-grown silicon dioxide biofluid barriers with improved stable operation lifetime, capable of operation in biofluids up to 25 days. *In vivo* analyses of biodistribution of dissolved silicon, hematology (complete blood count), blood chemistry, and histology demonstrate nontoxicity and biodegradability of the sensor.

Chapter 3 describes recent work on bioresorbable, Fabry-Perot ICP sensors interconnected with optical fibers to enable fully optics-based operation, eliminating issues of current leakage or magnetic resonance compatibility associated with electronic sensor implants. *In vitro* hydrolysis study results demonstrate biodegradability of these platforms. Data on *in vitro* and *in vivo* ICP measurements illustrate their accuracy.

Chapter 4 provides perspectives on bioresorbable device technologies, with details about on-going studies regarding biopolymer optical fibers that may go along with optical ICP sensors in Chapter 3 for fully bioresorbable optical platforms.

References

1 Hwang, S.-W. *et al.* Biodegradable Elastomers and Silicon Nanomembranes/Nanoribbons for Stretchable, Transient Electronics, and Biosensors. *Nano Letters* **15**, 2801-2808 (2015).

2 Hwang, S.-W. *et al.* High-Performance Biodegradable/Transient Electronics on Biodegradable Polymers. *Advanced Materials* **26**, 3905-3911 (2014).

3 Hwang, S.-W. *et al.* A Physically Transient Form of Silicon Electronics. *Science* **337**, 1640-1644 (2012).

4 Kang, S.-K. *et al.* Dissolution Behaviors and Applications of Silicon Oxides and Nitrides in Transient Electronics. *Advanced Functional Materials* **24**, 4427-4434 (2014).

5 Kang, S.-K. *et al.* Biodegradable Thin Metal Foils and Spin-On Glass Materials for Transient Electronics. *Advanced Functional Materials* **25**, 1789-1797 (2015).

6 Kang, S.-K. *et al.* Bioresorbable silicon electronic sensors for the brain. *Nature* **530**, 71 (2016).

7 Lee, C. H. *et al.* Wireless Microfluidic Systems for Programmed, Functional Transformation of Transient Electronic Devices. *Advanced Functional Materials* **25**, 5100-5106 (2015).

8 Yu, K. J. *et al.* Bioresorbable silicon electronics for transient spatiotemporal mapping of electrical activity from the cerebral cortex. *Nature Materials* **15**, 782 (2016).

9 Tao, H. *et al.* Silk-based resorbable electronic devices for remotely controlled therapy and in vivo infection abatement. *Proceedings of the National Academy of Sciences* **111**, 17385-17389 (2014).

10 Lee, G. *et al.* Fully Biodegradable Microsupercapacitor for Power Storage in Transient Electronics. *Advanced Energy Materials* **7**, 1700157-n/a (2017).

11 Kringelbach, M., Green, A. & Aziz, T. Balancing the Brain: Resting State Networks and Deep Brain Stimulation. *Frontiers in Integrative Neuroscience* **5** (2011).

12 Schoenfeld, M. H. Contemporary Pacemaker and Defibrillator Device Therapy. *Challenges Confronting the General Cardiologist* **115**, 638-653 (2007).

13 Farra, R. *et al.* First-in-Human Testing of a Wirelessly Controlled Drug Delivery Microchip. *Science Translational Medicine* **4**, 122ra121-122ra121 (2012).

14 Yuan, Q. *et al.* Impact of intracranial pressure monitoring on mortality in patients with traumatic brain injury: a systematic review and meta-analysis. *Journal of Neurosurgery* **122**, 574-587 (2015).

15 Sit, A. J. Continuous Monitoring of Intraocular Pressure: Rationale and Progress Toward A Clinical Device. *Journal of Glaucoma* **18**, 272-279 (2009).

16 Kirkpatrick, A. W. *et al.* Intra-abdominal hypertension and the abdominal compartment syndrome: updated consensus definitions and clinical practice guidelines from the World

Society of the Abdominal Compartment Syndrome. *Intensive Care Medicine* **39**, 1190-1206 (2013).

17 Coosemans, J. & Puers, R. An autonomous bladder pressure monitoring system. *Sensors and Actuators A: Physical* **123-124**, 155-161 (2005).

18 Brain Trauma, F. *et al.* Guidelines for the management of severe traumatic brain injury. VI. Indications for intracranial pressure monitoring. *J Neurotrauma* **24 Suppl 1**, S37-44 (2007).

19 Jiang, G. Design challenges of implantable pressure monitoring system. *Frontiers in Neuroscience* **4** (2010).

20 Yu, L., Kim, B. & Meng, E. Chronically Implanted Pressure Sensors: Challenges and State of the Field. *Sensors* **14**, 20620 (2014).

21 Chamis, A. L. *et al.* Staphylococcus aureus Bacteremia in Patients With Permanent Pacemakers or Implantable Cardioverter-Defibrillators. *Circulation* **104**, 1029-1033 (2001).

22 Hall-Stoodley, L., Costerton, J. W. & Stoodley, P. Bacterial biofilms: from the Natural environment to infectious diseases. *Nature Reviews Microbiology* **2**, 95 (2004).

23 Boutry, C. M. *et al.* Towards biodegradable wireless implants. *Philosophical Transactions of the Royal Society A: Mathematical, Physical and Engineering Sciences* **370**, 2418-2432 (2012).

CHAPTER 1: BIORESORBABLE SILICON SENSORS FOR THE BRAIN

1.1 Introduction

Many procedures in modern clinical medicine rely on the use of electronic implants in treating conditions that range from acute coronary events to traumatic injury[1,2]. However, standard permanent electronic hardware acts as a nidus for infection: bacteria form biofilms along percutaneous wires, or seed haematogenously, with the potential to migrate within the body and to provoke immune-mediated pathological tissue reactions[3,4]. The associated surgical retrieval procedures, meanwhile, subject patients to the distress associated with re-operation and expose them to additional complications[5–8]. Here, we report materials, device architectures, integration strategies, and *in vivo* demonstrations in rats of implantable, multifunctional silicon sensors for the brain, for which all of the constituent materials naturally resorb via hydrolysis and/or metabolic action[9–12], eliminating the need for extraction. Continuous monitoring of intracranial pressure and temperature illustrates functionality essential to the treatment of traumatic brain injury[2,13]; the measurement performance of our resorbable devices compares favourably with that of non-resorbable clinical standards. In our experiments, insulated percutaneous wires connect to an externally mounted, miniaturized wireless potentiostat for data transmission. In a separate set-up, we connect a sensor to an implanted (but only partially resorbable) data-communication system, proving the principle that there is no need for any percutaneous wiring. The devices can be adapted to sense fluid flow, motion, pH or thermal characteristics, in formats that are compatible with the body's abdomen and extremities, as well

---

S.-K. Kang, R.K.J. Murphy, S.-W. Hwang, S.M. Lee, D.V. Harburg, N.A. Krueger, J. Shin, P. Gamble, H. Cheng, S. Yu, Z. Liu, J.G. McCall, M. Stephen, H. Ying, J. Kim, G. Park, R.C. Webb, C.H. Lee, S. Chung, D.S. Wie, A.D. Gujar, B. Vemulapalli, A.H. Kim, K.-M. Lee, J. Cheng, Y. Huang, S.H. Lee, P.V. Braun, W.Z. Ray and J.A. Rogers, "Bioresorbable Silicon Electronic Sensors for the Brain," *Nature* 530, 71-76 (2016). Reprinted with permission from NPG.

as the deep brain, suggesting that the sensors might meet many needs in clinical medicine.

1.2 Experiments

Fabrication of bioresorbable silicon pressure sensor began with solid-state diffusion of boron at 950^{o}C of a silicon-on-insulator wafer (SOI; top Si ~ 300 nm, buried SiO2 ~1 μm, Si wafer ~ 600 μm; SOITEC, France) to obtain doped p-type silicon. Patterning with an array of holes (diameter ~3 μm, distance between holes ~30 μm), reactive ion etching (Plasma-Therm RIE; 50 mTorr, 100 W, 40 sccm SF_6) to etch holes through the Si NM and expose buried SiO_2, and immersing the wafer in hydrofluoric acid removed the buried oxide and allowed transfer of the Si NM onto a bilayer of diluted polyimdie (poly(poly(pyromellitic dianhydride-co-4,4′-oxydianiline)), ~300 nm)/PMMA (poly(methyl methacrylate), ~300 nm) on a temporary silicon carrier substrates.

Photolithography and RIE process patterned the Si NM into serpentine elements. Electron-beam (e-beam) evaporation, patterning, and wet etching in buffered oxide etchant formed a thin film of SiO_2 (~100 nm) for electrical passivation. Spin-coating a layer of D-PI (~300 nm), curing in an oven at ~200^{o}C for an hour, patterning and dry etching (March RIE; 200 mTorr, 150 W, 20 sccm O_2) etched through all of the layers (D-PI/SiO_2/D-PI/PMMA), which could then be immersed in a warm bath of acetone (~50^{o}C) to dissolve the PMMA sacrificial layer and release the individual serpentine Si NM elements sandwiched between layers of D-PI. D-PI was removed by March RIE first while the device was on the poly(dimethylsiloxane) (PDMS) stamp during transfer, then again after device was transferred on a biopolymer film of poly(lactic-co-glycolic acid) (PLGA, ~30 μm).

Fabrication of nano-porous silicon (np-Si, ~80 μm thick) substrate involved double-side polished, highly doped p-type Si wafers at current density of 160 mA cm^{-2}, as reported previously[1]. Careful transfer of released np-Si to a glass wafer spin-coated with a thin film of PDMS allowed microfabrication processes to be carried out without damaging the np-Si. Fabrication of trench (i.e. square regions of etched relief of dimensions 2.5 mm x 2.5 mm x 40 μm) on the np-Si substrate involved deposition of ~300 nm-thick film of PECVD (plasma-enhanced chemical vapor deposition) SiO_2 mask, patterning and wet etching using BOE, dry etching using RIE, and removing the oxide mask by wet etching. Fabrication of magnesium trench structures involved patterning and wet etching Mg foil (~100 μm thick, Goodfellow, USA) in a mixture of acetic acid (CH_3COOH, Transene Company Inc., USA) and deionized (DI) water (20 ml : 250 ml), stirred using a magnetic bar, until trench is ~40 um deep, followed by aligned laser cutting to define outer dimensions of the substrate (rectangular or pointed-end designs). Final step of fabrication involved transferring the PLGA films with Si NM elements onto the np-Si or Mg trench structures, heating the samples near glass transition temperature of PLGA (~65 ^oC) to bond the PLGA to the substrate and form a sealed air cavity.

1.3 Results and Discussion

Figures 1.1a and 1.2 show a bioresorbable pressure sensor with a magnified illustration of the active region and its cross-sectional side view. The construction involves a membrane of poly(lactic-co-glycolic acid) (PLGA, with a thickness of 30 μm), sealed against a supporting substrate of nanoporous silicon (60-80 μm thick; 71% porosity) or magnesium foil (60–80 μm thick; see Figs 1.3, 1.4). The substrate has a square structure of relief (with a depth of 30–40 μm) etched onto its surface. The associated air cavity allows the membrane to deflect in response to

pressure in the fluid surroundings. A silicon nanomembrane in a serpentine geometry serves as a piezoresistive element that rests on the surface of the membrane near one of the edges of the cavity, where deflection- induced strains are largest (Fig. 1.1b). The resistance of this sensing element increases monotonically in a linear fashion across the full range of pressures that are relevant to intracranial monitoring (that is, 0–70 mm Hg). An overcoat of silicon oxide (SiO_2, about 100 nm thick) provides electrical passivation and a barrier against biofluids. Figures 1.1c and 1.5 show photographs of two representative devices of different dimensions to illustrate the scalability of fabrication; the total sizes and weights are 1 mm × 2 mm × 0.08 mm (trench size: 0.67 mm × 0.8 mm × 0.03 mm) and about 0.4 mg; and 3 mm × 6 mm × 0.11 mm (trench size: 2 mm × 2.4 mm × 0.04 mm) and roughly 1 mg, respectively. The mechanics of the system can be captured quantitatively by three-dimensional finite element analysis (FEA). Distributions of principal strains and vertical displacements evaluated at an external pressure of 50 mm Hg appear in Figure 1.1d. The maximum strain for any applied pressure over the range of interest occurs at the midpoint of the left (and right) edge of the trench, thus motivating this choice of location for the silicon-nanomembrane piezoresistive element (see Methods and Figures 1.6 and 1.7 for details)[14]. The calibration between pressure and resistance is linear, with a slope of 83 Ω/mmHg), consistent with modelling results and a gauge factor of about 30, which lies within a range of expected values for monocrystalline silicon (Fig. 1.8)[15].

Evaluations in set-ups that resemble the intracranial cavity reveal measured pressure responses that agree quantitatively with those of clinical- standard, non-bioresorbable sensors (Figs. 1.1e and 1.9-1.11). With various simple modifications, this same platform can be used for precision measurement of other parameters of interest in biomedicine and clinical care. Examples include: motion sensors built with a cantilevered test mass of PLGA (that is, a single-

axis accelerometer, Fig. 1.1f); temperature sensors that exploit the temperaturedependent resistance of silicon-nanomembrane elements set apart from the cavity structure (Fig. 1.1g); flow sensors in which the silicon nanomembranes serve simultaneously as heating elements and temperature sensors (Fig. 1.1h); thermal conductivity/diffusivity sensors that exploit related concepts (Fig. 1.1i); and pH sensors that rely on electrostatic gating of transport through the silicon nanomembrane (Fig. 1.1j). In addition, chemically functionalizing the surface of the silicon of this last device provides a route to biomolecular sensing, using schemes similar to those in conventional silicon biosensors[16–18]. The fabrication methods and operating principles for each of the modalities in Fig. 1.1f–j appear in Methods and Figures 1.12-1.16.

The uniqueness of these devices is their ability to dissolve completely into biocompatible end products when immersed in aqueous solutions, including biofluids such as cerebrospinal fluid (CSF). Hydrolysis of the silicon nanomembranes, the layers of SiO_2, the thin wafers of nanoporous silicon and the magnesium foils causes loss of material at rates of 23 nm day^{-1}, 8 nm day^{-1}, 9 μm day^{-1} and 4 μm day^{-1}, respectively, in artificial CSF (ACSF) at physiological temperature (37 °C) (Fig. 1.17). Separate studies indicate that PLGA (75:25 (lactide:glycolide) composition) dissolves in biofluids within four to five weeks[19]. To illustrate the various stages of dissolution of a completed system, Fig. 1k shows a sequence of images of a bioresorbable pressure sensor inserted into a transparent cha zber designed for accelerated testing (polydimethylsiloxane (PDMS) enclosure filled with buffer solution at pH 12 and room temperature), in which fluid exchange can occur through an array of openings around the perimeter (Fig. 1.18). Figure 1.19 presents images of nanoporous silicon and silicon nanomembranes observed by scanning electron microscopy at different times during hydrolysis. The silicon nanomembrane dissolves uniformly, without fracture. By comparison, nanoporous

silicon dissolves less uniformly, with a tendency to form fragments. Here, the silicon-nanomembrane and SiO_2 components dissolve first, within 15 hours, followed by the nanoporous silicon, which disappears within 30 hours. In all cases, the dissolution kinetics depends strongly on the materials and the composition of the surrounding solution[20–22]. Table 1.1 summarizes the hydrolysis mechanisms and dissolution rates of these materials in a representative solution. As described below, the encapsulation material and its thickness define the operational lifetimes.

Figure 1.20 illustrates a strategy for using these types of bioresorbable systems for wireless pressure and temperature monitoring in the intracranial space of rats. Figure 1.20a shows a photograph of a device like the one in Fig. 1.1c, but configured to allow simultaneous sensing of both pressure and temperature. The measured temperature can also be used to calibrate against parasitic effects of this parameter on the pressure determination (see Methods and Fig. 1.21). Biodegradable molybdenum wires (10 μm thick) serve as an interface to wireless communication systems. Pressing the interconnect wires (molybdenum, 10 μm thick, or magnesium, 50 μm thick) against the PLGA at elevated temperatures (65 °C) embeds them near the surface but leaves the top regions exposed, thereby allowing for deposition of biodegradable metals (molybdenum, 2 μm thick) to form electrical contact pads through stencil masks (made from the polyimide Kapton, 12.5 μm thick; Fig. 1.22). The deposited molybdenum forms stable interconnects between metal wires and silicon nanomembranes that are fully embedded on PLGA. Encapsulation with a bioresorbable polymer (polyanhydride, discussed in more detail below) enhances system robustness by reducing the stress concentrations at the interconnections. Narrow strips of PLGA laminated onto the front and back sides of the wires along their entire lengths act as electrical insulation. These insulated wires connect to an externally mounted, miniaturized wireless potentiostat for transmission of data thorough percutaneous wiring.

Figure 1.20b provides a diagram of such a system in the intracranial space of a rat model. The sensor subsystem connects via molybdenum wires to the wireless module, which is mounted on the top of the skull. Figure 1.20c–e summarizes the surgical process. A PLGA sheet (about 80 μm thick) and a dissolvable surgical glue (Fig. 1.20c) seal the craniectomy defect to close the intracranial cavity. Conventional sutures hold the surgical site closed, in a standard process[23] that retains points at which the dissolvable wires emerge from the skin to allow electrical connection (Fig. 1.20d). These wires have dimensions comparable to those of the surgical threads, and therefore pose little additional risk. Figure 1.20e shows a healthy, freely moving rat with a complete system. Figure 1.23 presents image of the connections.

Figure 1.24 summarizes the results of a comprehensive set of wireless measurements of intracranial pressure (ICP) and intracranial temperature (ICT), recorded in rats with percutaneous wired systems. The ICP traces reveal features that correspond to periodic manual abdominal compression activating the Valsalva manoeuvre, which yields rapid increases or decreases in ICP (Fig. 1.24a)[24]. Gentle changes in the rat's position—that is, Trendelenburg (30° head-down position) and reverse Trendelenburg (30° head-up position)—produce gradual increases and decreases in ICP, respectively (Fig. 1.24b), as would be expected because of the corresponding accumulation and depletion of blood in the brain[25]. The pressure values compare well with those determined using a clinical-standard, wired ICP sensor implanted in the same region of the same animal.

The wireless, bioresorbable ICT sensors perform to levels of accuracy similar to those of commercial sensors: Figs. 1.24c and d show comparative data collected by modulating the cranial temperature with a heating or cooling blanket placed beneath the animal. The operational lifetimes of the devices are defined by dissolution of the encapsulation layers and the permeation

of fluids through them. *In vitro* experiments using a bioresorbable pressure sensor encapsulated with a film of a specially synthesized polyanhydride (about 120 μm thick; Fig. 1.25) show expected performance and accurate readings with an appropriately modified calibration factor (50 Ω/mmHg). The slow dissolution rate of the polyanhydride (about 1.3 μm day^{-1})—together with the modest change in sensitivity that occurs depending on the thickness of this material (about 0.34 $\Omega(mmHg)^{-1}$ μm^{-1})—leads to a loss of accuracy of only a few per cent when operated over several days. This error falls within standards defined by the Association for the Advancement of Medical Instrumentation (AAMI) for pressure monitoring, that is, ±2 mm Hg (from 0 to 20 mm Hg) and ±10% (from 20 to 100 mm Hg)[2]. (Methods and Figs. 1.26-28 present information on the synthesis/hydrolysis chemistry, dissolution kinetics, water permeability, and biocompatibility of the polyanhydride.) Stable, continuous operation is possible for up to three days (Fig. 1.29). Beyond this period, water tends to pass through the polyanhydride and PLGA into the electrically active regions of the device and the air cavity. The resistance remains relatively constant for seven days, and then begins to increase markedly, mainly because of dissolution of the molybdenum wires and interconnection metal (Figs 1.30 and 1.31). Figure 1.24e illustrates *in vivo* operation for three days without notable degradation in absolute accuracy or sensitivity, as benchmarked against a standard, non-resorbable wired sensor. Figure 1.32 shows similar data from the temperature sensor, where the absence of an air cavity affords enhanced stability, and accurate measurements for six days of operation. These timeframes are relevant for clinical use: ICP and ICT are typically monitored continuously for several days after traumatic brain injury. The chemistry, thickness and composition of the encapsulating layers can be selected to extend the functional lifetimes[26].

Biocompatibility of the devices through all stages of their life cycle is essential. Comprehensive studies of the immunohistochemistry of brain tissues at several times after implantation (two, four and eight weeks) demonstrate that the sensors and the by-products of their dissolution in the intracranial space are biocompatible. Representative confocal fluorescence images (see Fig. 1.24f for nanoporous silicon and Fig. 1.33 for magnesium foil) indicate no overt reaction of brain glial cells to the sensor, and no focal aggregation of glial cells at the implantation site for all time ranges. Astrocytosis (an increase in the number of astrocyte cells) and microglial activity at the cortical surface are within normal limits, indicating no overt immune reaction to the device and its by-products.

Although the percutaneous wiring does not noticeably affect animal behaviour (see Methods and Fig. 1.34), a miniaturized, fully implantable wireless communication system might offer advantages, by removing the possibility of secondary infection at the wires. A wireless system constructed mostly, but not entirely, of resorbable materials (~85% by mass and ~86% by volume)—using an advanced near-field communication-technology approach, with fully bioresorbable metal coils, substrates and encapsulation layers—appears in Figure 1.35, Methods, and Figures 1.36-1.41. Given that these devices function successfully in the intracranial space, they could also be used in other organs and body compartments. As an example, Fig. 1.42a and b illustrate ICP monitoring using the same bioresorbable device in modes with relevance to acute abdominal compartment syndrome and acute compartment syndrome of the extremity[27,28]. Furthermore, modifying the devices to allow them to be injected deep into tissues could address other needs in clinical treatment. For example, monitoring physiological parameters of the deep brain with intraparenchymal sensors could yield data that are unavailable from the surface or the intracranial space. In addition, because electrophysiological and metabolic abnormalities often

emanate from infarcts, contusions and haematomas that damage adjacent intact tissue, sensors of pressure, temperature, pH and other physical/chemical parameters that are placed into the parenchyma within the blood-deprived (ischaemic) penumbra could advance our knowledge of secondary brain injury[29–31]. Such considerations apply not only to injured brain tissue, but also to acute or chronic ischaemia that threatens the heart, limbs, intra-abdominal organs or grafts.

Modifying the geometry of the supporting structures introduced in Figure 1.1 enables delivery of bioresorbable sensors into the depths of brain tissue, for direct measurements of injury or status. Figure 1.42c shows an example that integrates a bioresorbable ICP sensor onto a magnesium foil, formed with a tip region that allows injection into tissues of interest (Fig. 1.43). Mounting the device on a stereotactic frame and fixture allows accurate positioning and controlled penetration (Fig. 1.44). Figures 1.42d and e summarize pressure and temperature data collected at a site about 5 mm beneath the surface of the rat brain. The Valsalva manoeuvre yields data that quantitatively agree with those obtained using conventional sensors at a similar location. The device detected changes in temperature during anaesthesia (the temperature decreased, owing to reduced blood circulation) and waking up (the temperature returned to normal), as expected of intraparenchymal tissue.

1.4 Conclusion

The biomedical sensors reported here enable wireless data collection in body cavities and in deep tissues, with platforms that are fully bioresorbable, thereby allowing patients to be monitored until homeostasis has been achieved, and avoiding the risks associated with chronically implanted devices or their removal[32,33]. *In vivo* and *in vitro* experiments demonstrate precision measurements of pressure, temperature, motion, flow, thermal properties and pH, with

possible extensions to biomolecular binding events. These features will be useful in diagnosing and treating a diverse range of medical conditions, from acute traumatic injuries such as extremity compartment syndrome, to chronic medical diseases such as diabetes. The materials, manufacturing methods and design layouts should be relevant to many other sensor modalities, with the potential for co-integration of advanced silicon-based integrated circuits, radio communication technologies, power supply and energy harvesters—each adapted from advances in transient electronics. Thus, it is realistic to expect that these devices could be used in sensing, recording, stimulating, and electrical control for medical monitoring and treatment, not only for the body regions explored here but also for areas such as the cardiac space and spinal system. Translating these technologies into clinical settings should provide patients and medical professionals with a vital set of tools for combating human disease.

1.5 Methods

Fabrication of bioresorbable silicon pressure sensors. Procedures involved integration of silicon-based, piezoresistive sensing elements onto substrates of PLGA, bonded over cavities etched into the surfaces of nanoporous Si (np-Si) substrates or magnesium foils. Solid-state diffusion of boron yielded highly doped p-type monocrystalline silicon nanomembranes (Si NMs) on silicon-on-insulator (SOI) wafers (top silicon ~300 nm thick, p-type; SOITEC, France). Eliminating the buried oxide with hydrofluoric acid allowed transfer of the Si-NMs onto a bilayer of D-PI (diluted polyimide (poly(pyromellitic dianhydride-co-4,4′-oxydianiline)), ~200 nm)/PMMA (poly(methyl methacrylate), ~300 nm) on temporary silicon carrier substrates. Photolithography and etching patterned the Si NMs into structures with serpentine designs. Electron-beam evaporation and spin-casting defined uniform layers of SiO_2 (~100 nm) and D-PI,

respectively, to serve the purpose of passivation. Selective dry etching through all of the layers (D-PI/SiO2/D-PI/PMMA) formed a mesh structure that enabled release in acetone, for transfer to a film of PLGA (~30 μm). Heating these films to temperatures near the glass transition of the PLGA (65 °C) and laminating them onto np-Si substrates (or magnesium foils, ~60–80 μm) with square regions of etched relief (~30–40 μm) formed sealed air cavities upon cooling to room temperature.

Calibration of the pressure response. Responses of commercial sensors under environments similar to those in the intracranial cavity allowed absolute pressure calibration for the bioresorbable devices. The experiments involved placin a bioresorbable pressure sensor inside the barrel of a syringe partially filled with ACSF (Ecocyte BioScience, USA) and with a commercial sensor (NeuLog, USA) located at its open end (orifice). Moving the plunger component of the syringe allowed reversible access to well controlled pressures throughout a range relevant to intracranial monitoring (Fig. 1.10). Comparison of the electrical resistance of the bioresorbable sensor (via data acquisition (DAQ) system USB-4065, National Instruments, USA) with pressures from the commercial sensor yielded calibration curves.

Connections to wireless data-transmission systems. Laser cutting of foils of molybdenum (~10 μm thick) or magnesium (~50 μm thick) yielded dissolvable narrow metal strips (that is, interconnection wires, 80 μm × 30 mm). Pressing these wires against PLGA substrates using a PDMS stamp at 65 °C embedded them into the surface of the PLGA. Sputter deposition of molybdenum (~2 μm) through high-resolution stencil masks (12.5 μm, Kapton; Dupont, USA) yielded electrical connections between the wires and contact pads on the PLGA (Fig. 1.22). The opposite ends of the wires connected to externally mounted wireless communication systems (Pinnacle Technology, USA) (Fig. 1.23).

Evaluation of the kinetics of device dissolution. Measurements of time-dependent changes in the thicknesses of square (100 μm × 100 μm) Si-NMs (~200 nm thick), electron-beam evaporated layers of SiO_2 (~100 nm), free-standing nanoporous silicon substrates (np-Si, ~80 μm) and magnesium foils (~80 μm) due to immersion in ACSF at body temperature (37 °C) established the dissolution kinetics of the key materials. Removing samples from the ACSF every other day, rinsing them with deionized water, and measuring the thicknesses by profilometry (Dektak, USA) yielded the dissolution rate, as in Figure 1.17. Sealed reservoirs of PDMS with viewing windows allowed for observation of dissolution behaviour at the level of the completed devices. These engineered structures included access channels around the periphery to allow passive fluid exchange and diffusion with a surrounding bath (Figure 1.18).

Evaluation in animal models. Studies were performed in strict accordance with the recommendations in the Guide for the Care and Use of Laboratory Animals of the National Institutes of Health. The protocol was approved by the Institutional Animal Care and Use Committee (IACUC) of Washington University in St Louis (protocol number 20140207). Male Lewis rats weighing 250–350 g (Charles River, Wilmington, MA) received subcutaneous injections of buprenorphine hydrochloride (0.05 mg kg^{-1}; Reckitt Benckiser Healthcare Ltd, USA) for pain management, and of ampicillin (50 mg kg^{-1}; Sage Pharmaceuticals, USA) to prevent infection at the implantation site before the surgical process. Animals were anaesthetized with isoflurane gas and held in a stereotaxic frame for the duration of the surgical procedure and measurements. Opening a craniectomy and dural, implanting bioresorbable sensors on the cortical surface, sealing the craniectomy with a PLGA sheet (~80 μm thick) and/or biodegradable surgical glue, and suturing the skin implanted the fully resorbable biosensing system in intracranial space. Comparison testing with a clinical intracranial pressure sensor

(Integra LifeSciences, USA) and commercial thermistor (DigiKey Electronics, USA) implanted in parallel to bioresorbable sensors demonstrated the functionality of the bioresorbable sensors. To implant the injectable device, the same procedure of opening a craniectomy and dural was performed. Injecting needle-shaped biosensors into the brain parenchyma (~5 mm deep) with a stereotactic frame and arm enabled monitoring of pressure and temperature in the deep-brain parenchyma. The immunohistochemistry tests used five individual rats per stage (2, 4 and 8 weeks) and device type (np-Si and magnesium-foil substrates). *In vivo* functionality tests of pressure and temperature sensors involved three trials using different batches of devices and animals, to establish reproducibility.

Implantable near-field-communication wireless system. The sensor introduced in Fig. 1.20a can be integrated with sub-dermal wireless data-transmission systems, constructed largely of bioresorbable materials, via thin, bioresorbable wires that pass through the skull. Figure 1.35a and b show an illustration of a chipscale, near-field-communication (NFC) technology that includes bioresorbable coils, polymer substrates, encapsulation layers and resistors, a partially bioresorbable NFC chip, and non-resorbable capacitors, and a picture of this system integrated with a bioresorbable pressure sensor via biodegradable wiring. Here, micro-patterned magnesium coils (50 μm thick, outer diameter 15 mm) allow inductive coupling to an external data reader for power transfer and data transmission. A silicon-based logic chip (RF430FRL152H, Texas Instruments, USA; 4 mm × 4 mm × ~300 μm) captures the measured data at a high acquisition rate, then digitizes and processes the information for transmission to the external reader. Passive components include Si-NM resistors and capacitors. PLGA serves as the substrate and electrical passivation layer. Figure 1.35c summarizes the operating principles. The external reader wirelessly delivers power for operating the logic chip and provides the small currents needed to

assess the response of the piezoresistive and thermoresistive sensors. In particular, changes in resistance associated with changes in pressure and temperature register as voltages that can be recorded and transmitted to the external reader by the NFC chip through the associated coil antenna. This NFC system is far more sophisticated than a conventional radio-frequency-identification (RFID) tag. Here, a single chip platform provides all of the computing functionality needed for high-speed data recording, real-time software filtering, and wireless transmission of sensor outputs a s captured with an on-board 14-bit analogue-to-digital converter.

This system communicates through biofluids and tissue with little loss, owing to the use of magnetic coupling in a relatively low-frequency band (13.56 MHz; Fig. 1.36), consistent with negligible heating associated with system operation (Fig. 1.37). These characteristics enable communication distance of up to 25 mm through biological tissue. The high-speed, programmable operation of the NFC chip is critical to overall operation. Figure 1.38a presents examples of data-acquisition rates of up to 250 Hz, via recordings of oscillating voltages (sine wave) with frequencies from 1 Hz to 50 Hz. Spectrograms and other related data appear in Figure. 1.38b–d. These high sampling rates allow efficient operation of digital filtering algorithms, and they also foreshadow the ability to measure biosignals such as EEG, ECoG and ECG. Figure 1.39 demonstrates the response of real-time high/low-pass filter function achieved by software programming for on-board computation with the NFC chip. Figure 1.40 shows two-channel operation of the system with/without this type of filtering during sensing. This integrated system provides wireless operation that compares quantitatively with that of a commercial wired sensor (Fig. 1.41).

The wireless module is largely bioresorbable, as illustrated in Figure 1.35d through images at various stages of dissolution in ACSF at 60 °C. The magnesium coils, electrodes,

interconnects and silicon resistors (240 mg; ~85% of the total mass of the NFC system) dissolve fully after 14 days. Here, the NFC chip is not bioresorbable; but fully bioresorbable complementary metal-oxide semiconductor (CMOS) circuit technologies offer the potential for constructing bioresorbable chips. In particular, recently reported schemes demonstrate that modest modifications to otherwise conventional semiconductor-manufacturing techniques allow the use of foundry fabrication facilities for construction of bioresorbable CMOS[34]. Even with the examples presented here, where the NFC chip is not fully bioresorbable, the associated implantation strategy minimizes risk by locating the hardware subdermally on the skull, outside the intracranial space, thereby allowing rapid, facile extraction.

In this overall architecture, the fully bioresorbable sensors reside in the intracranial space, while the NFC system resides extracranially within the subgaleal layer of the scalp. Fine, dissolvable wiring provides electrical interconnections through a burr hole in the skull, sealed with a bioresorbable surgical glue. After completing the subgaleal closure, the wireless system and sensor are fully implanted. Figure 1.35e–h show a diagram of the implantation strategy, surgical process, and wireless *in vivo* intracranial pressure and temperature results measured in a rat model. Here, all of the components in the intracranial region are fully bioresorbable. The non-bioresorbable components of the system remain extra-axial within the scalp, thereby minimizing the risk of provoking pathological neuroinflammation in the intracranial space. In addition, the relative material safety (as judged by the US Food and Drug Administration (FDA) class) of, for example, a subdermally implanted encapsulated non-resorbable device (such as an RFID chip) is similar to that of a titanium fixation screw. Removal of an extra-axial component involves a much lower risk than intracranial surgery. Intracranial pressure and temperature values measured

in the rat model using the NFC system are comparable to those captured using commercial wired sensors.

Fabrication of a fully implantable NFC wireless system. The magnesium foil was patterned on the PDMS by using photolithography and etching with dilute hydrochloric acid (deionized water:HCl = 15:1). Transfer printing of the patterned magnesium foil onto a film of PLGA (~150 μm) formed the inductive coil and electrode. The Si-NM resistor was formed on the SOI wafer by doping with phosphorus at 950 °C and patterning the top silicon (~300 nm thick) into the trace. Undercutting the buried oxide with hydrofluoric acid and transfer printing Si-NM on PLGA formed the resistor of NFC system. Laminating the top PLGA (~150 μm) and heating it at 65 °C yielded the passivation layer. Biodegradable conductive W paste served to interconnect the NFC wireless system to the metal wire (molybdenum or magnesium)[35].

1.6 Tables

Table 1.1 Hydrolysis mechanisms and dissolution rates of key materials in this study (ACSF and PBS measured at 37 °C, DI at room temperature).

Materials	Dissolution rate (nm/day)			Hydrolysis mechanism
	ACSF	PBS[12,21]	DI[22]	
Si NM	2.3×10^1	0.5×10^1		$Si + 4H_2O \rightarrow Si(OH)_4 + 2H_2$
np-Si	9.0×10^3	-	-	
SiO_2	0.8×10^1	1.4×10^1		$SiO_2 + 2H_2O \rightarrow Si(OH)_4$
Mg	4.0×10^3	-	1.7×10^3	$MgO + H_2O \rightarrow Mg(OH)_2$
Mo	-	2.0×10^1	0.7×10^1	$2Mo + 2H_2O + 3O_2 \rightarrow 2H_2MoO_4$

1.7 Figures

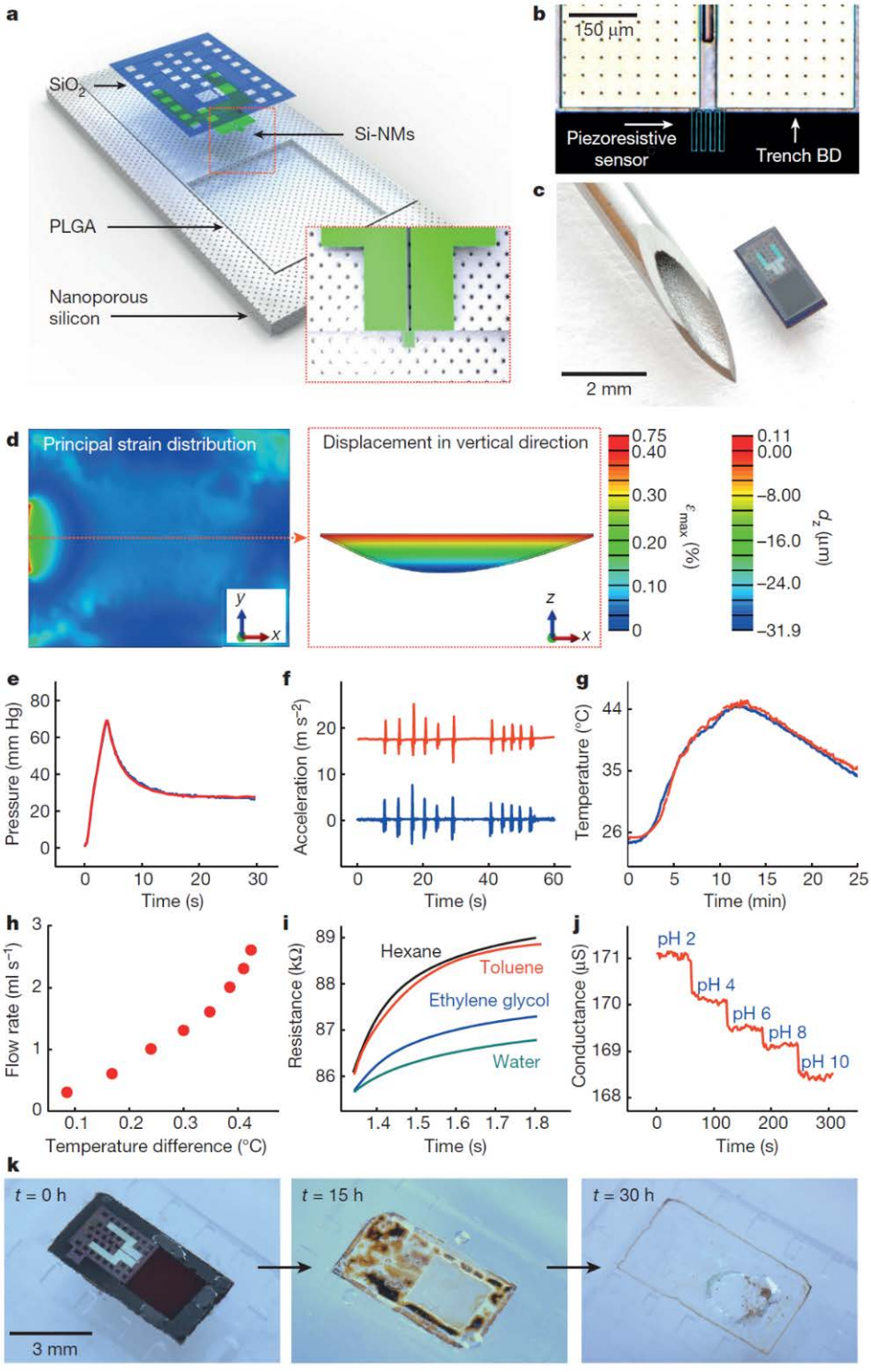

Figure 1.1 Bioresorbable, silicon-based mechanical/physical/chemical sensors for biomedical applications. a, Schematic illustration of a biodegradable pressure sensor. The inset shows the

Fig. 1.1 (cont.) location of the siliconnanomembrane (Si-NM) strain gauge. b, Optical micrograph of the strain-gauge region. 'Trench BD', boundary of the trench. c, Image of a complete device. The outer diameter of the hypodermic needle is 1 mm. d, Left, distribution of principal strains across the PLGA layer, including the Si-NM strain gauge at the left edge, determined from finite element analysis (FEA) for an external pressure of 50 mm Hg. Right, corresponding displacement profile evaluated along the red dotted line in the left panel. ε_{max} and d_z are the principal strain and vertical displacement, respectively. e, Responses of a commercial pressure sensor (blue) and a calibrated biodegradable device (red) to time-varying pressure over a range relevant to intracranial monitoring. f, Response of a similar biodegradable device (red), but configured as an accelerometer, with comparison to a commercial sensor (blue). g, Comparison of the calibrated response of such a bioresorbable temperature sensor (red) to a commercial device (blue). h, The difference in temperature measured by two separate Si-NM temperature sensors placed near a Si-NM element for Joule heating allows assessment of flow rate. i, A single serpentine Si-NM used as both a temperature sensor and a heating element allows measurements of thermal conductivity and heat capacity. The graph shows time-dependent changes in temperature upon actuation of Joule heating in devices immersed in different liquids. The coefficients of thermal conductivity (κ, measured through the rate of resistance change) of hexane, toluene, ethylene glycol, and water are 0.12, 0.13, 0.26, and 0.60 W m^{-1} K^{-1}, respectively. j, When the Si-NM is exposed to aqueous surroundings, its conductance depends on pH. The graph shows measurements for immersion in solutions with pH values between 2 and 10. k, Images collected at several stages ofaccelerated dissolution of a bioresorbable pressure sensor upon insertion into an aqueous buffer solution (pH 12) in a transparent PDMS enclosure at room temperature.

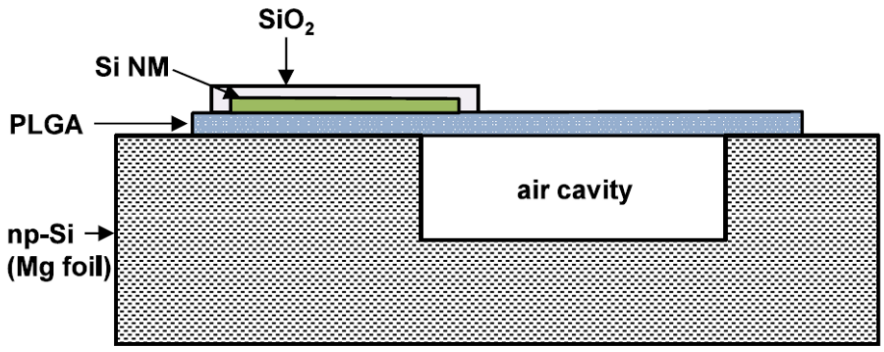

Figure 1.2 Cross-sectional side view of the bioresorbable pressure sensor.

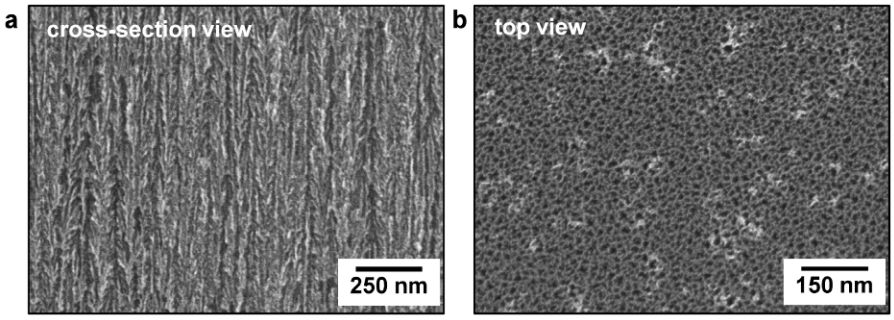

Figure 1.3 Scanning electron microscope (SEM) images of nanoporous Si. a) Crosssection view and b) top view of np-Si structure with ~71 % porosity.

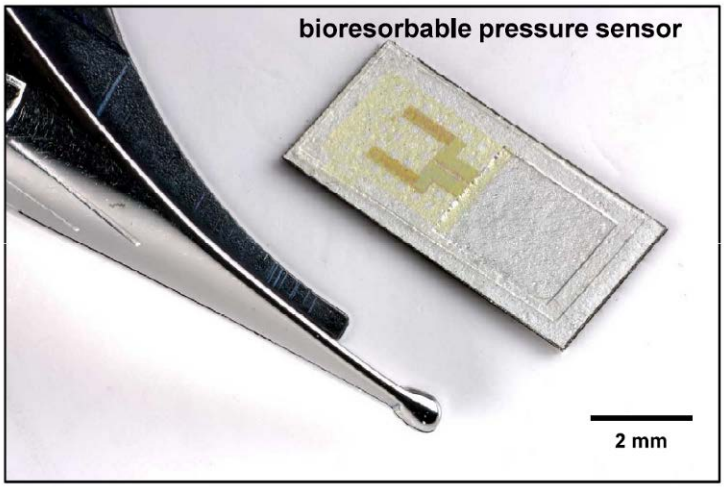

Figure 1.4 Biodegradable pressure sensor with Mg trench structure. Trench depth and thickness of Mg foil are ~ 40 μm and ~ 80 μm, respectively.

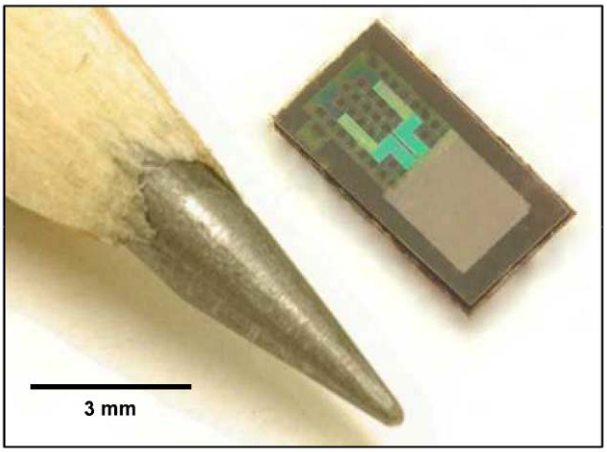

Figure 1.5 Image of a bioresorbable pressure sensor, with a thickness of ~110 μm, a weight of ~1 mg and overall lateral dimensions of 3 mm × 6 mm and trench dimensions of 2 mm × 2.4 mm × 40 μm.

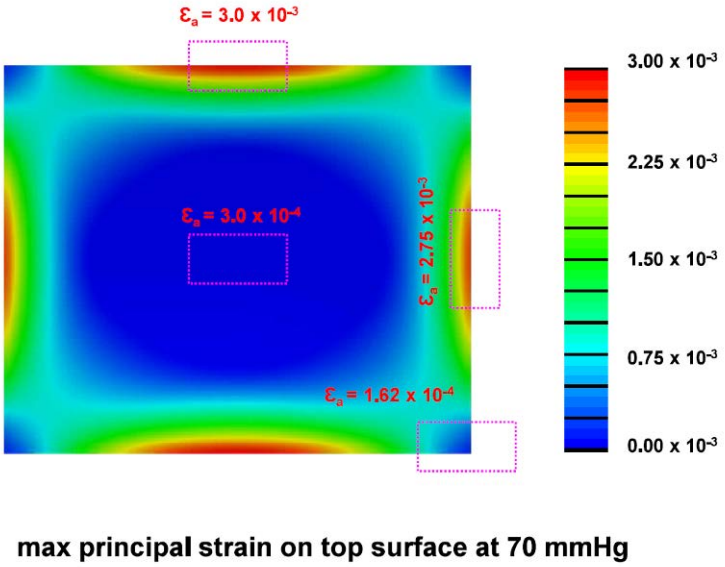

Figure 1.6 Optimization of the location of the piezoresistive serpentine sensors.

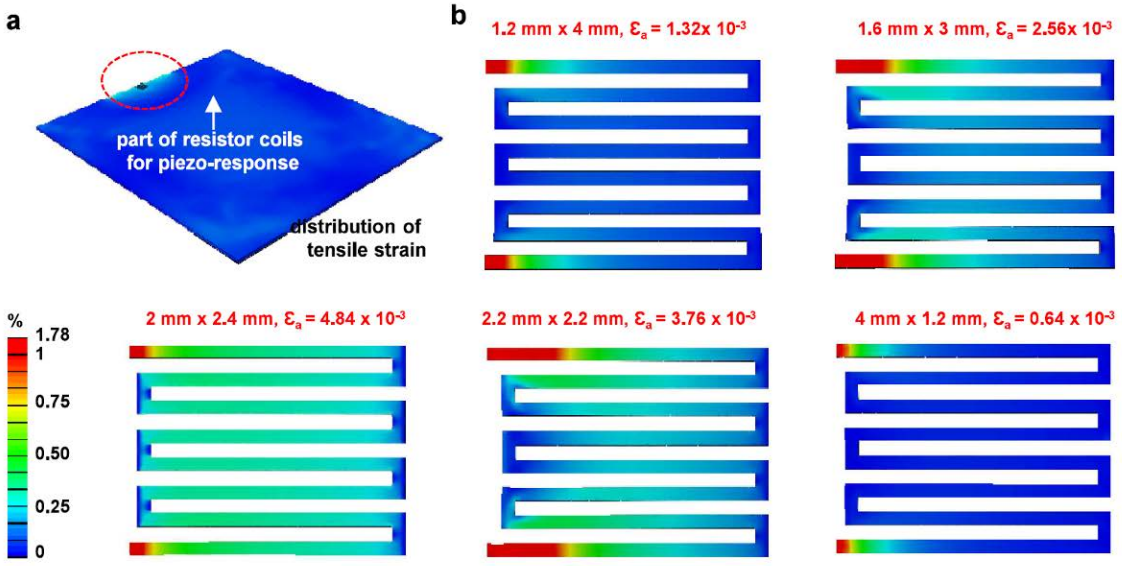

Figure 1.7 Optimization of trench geometry through stress-strain analysis using the finite element method (FEM). a) Full image of simulated dimension. b) Principle strain distribution around the piezoresistive serpentine sensors for various trench geometries. ε_a represents average strain on coils.

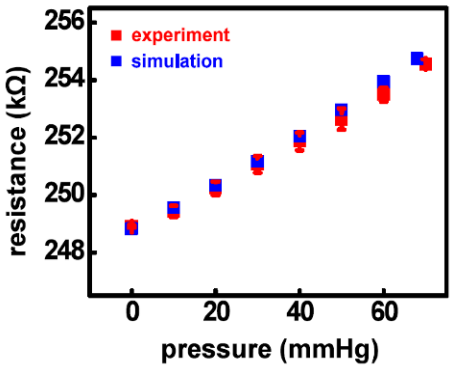

Figure 1.8 Piezoresistive response of the pressure sensor compared to finite element method (FEM) simulation (error bars represents standard deviations).

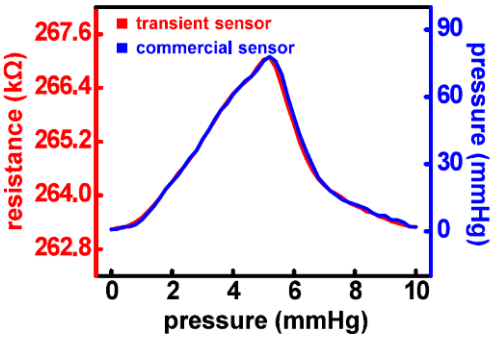

Figure 1.9 Calibration curve of pressure sensor with 2 mm × 2.4 mm × 40 μm dimension.

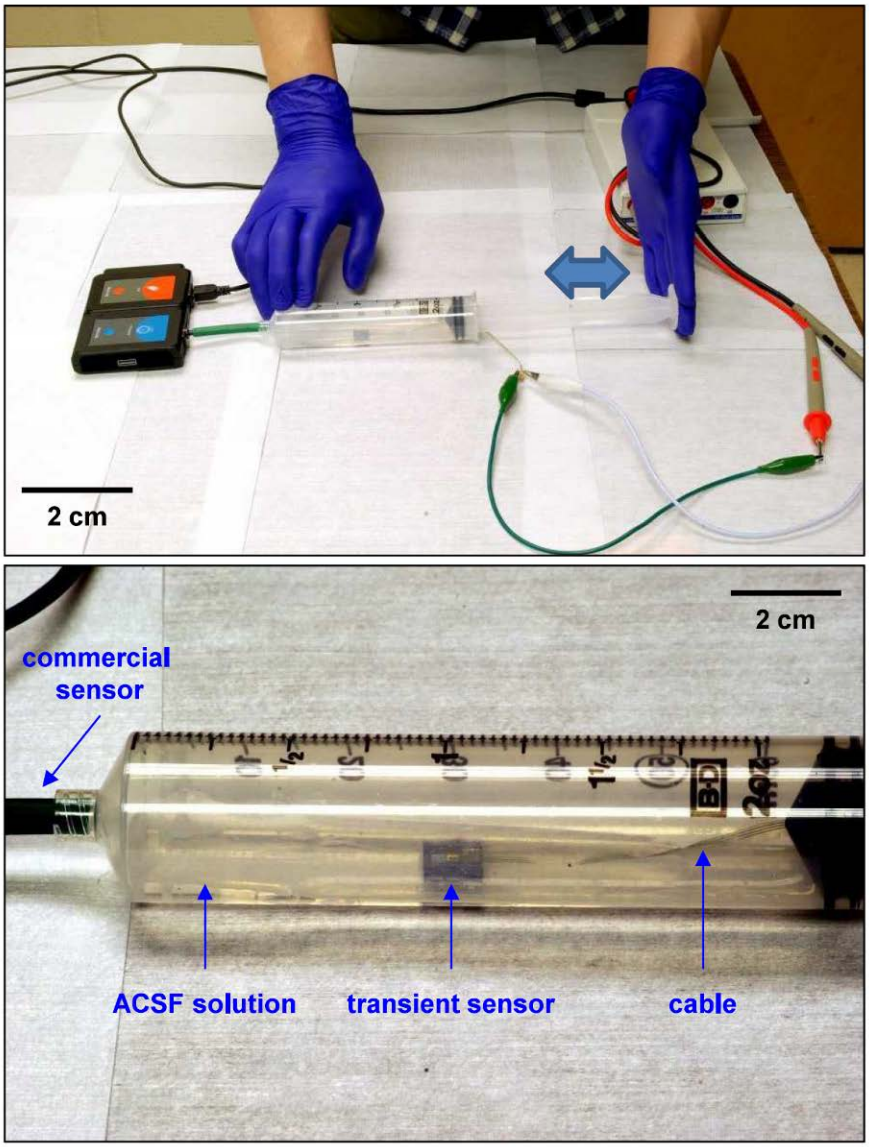

Figure 1.10 *In vitro* test of transient pressure sensor in ACSF solution.

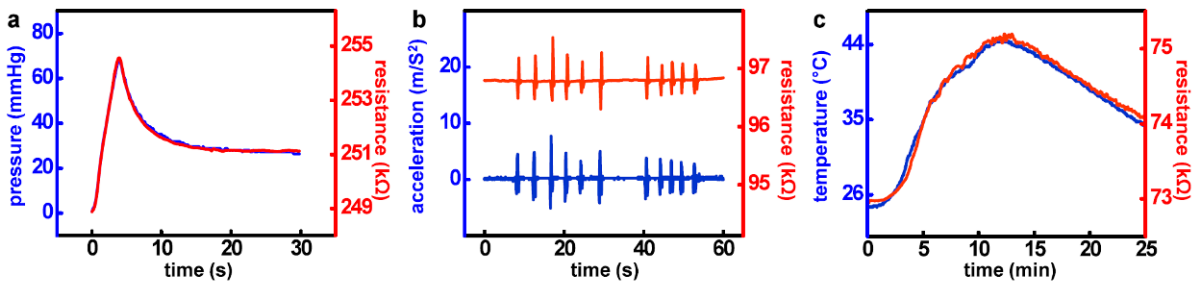

Figure 1.11 Calibration of resistance change to a) pressure, b) acceleration, and c) temperature.

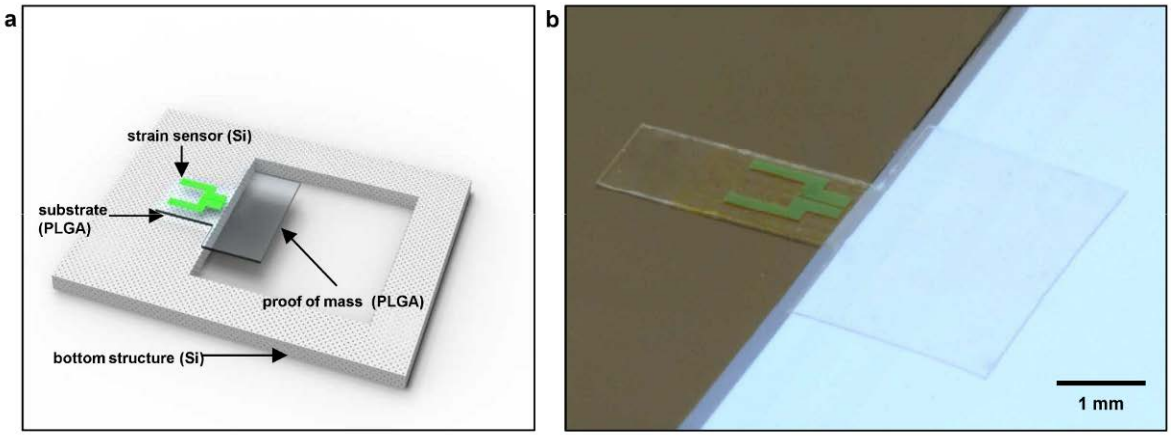

Figure 1.12 Transient accelerometer with Si-NM piezoresistive strain sensor. a) Materials and structure of accelerometer with PLGA proof mass. b) Image of bioresorbable accelerometer on the Si structure.

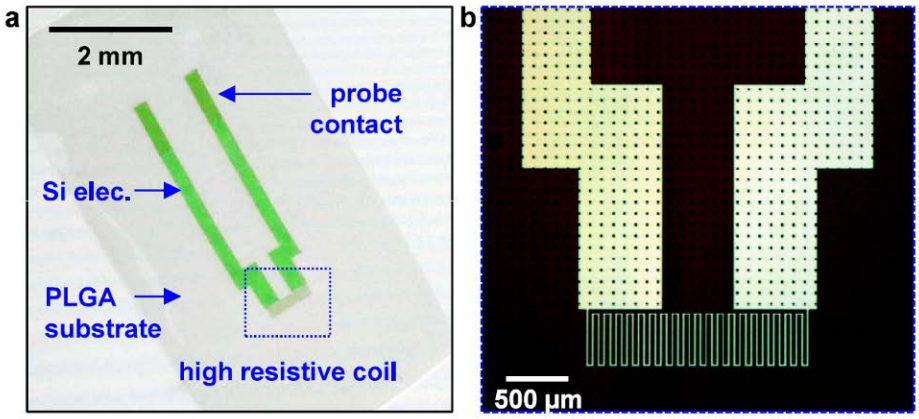

Figure 1.13 Bioresorbable temperature sensor on a thin PLGA film. a) Materials and structure of a thermoresistive Si temperature sensor. b) Microscope image of a dense serpentine Si-NM structure for enhanced thermoresistive response.

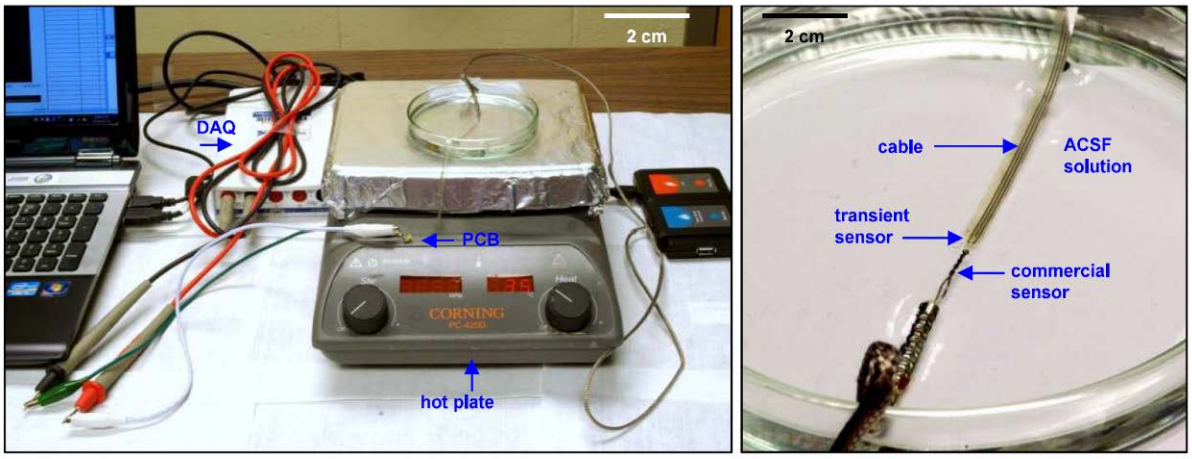

Figure 1.14 *In vitro* setup for transient temperature sensors.

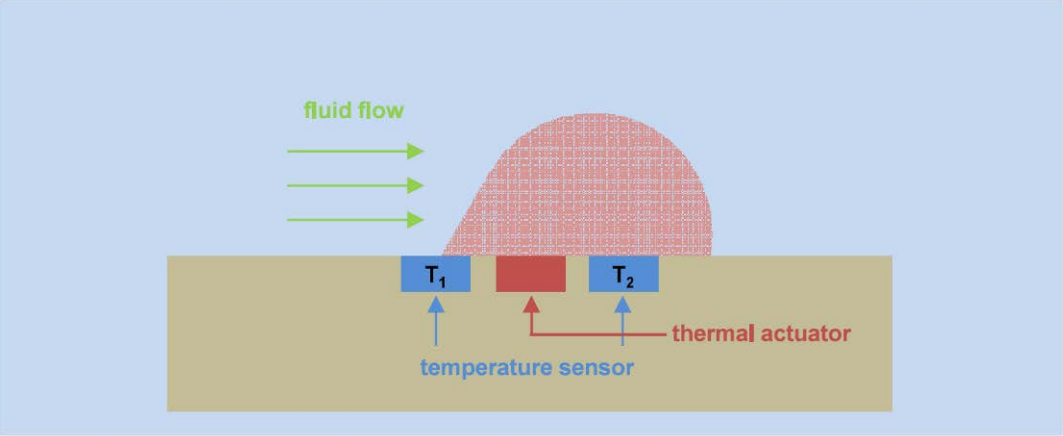

Figure 1.15 Principle of flow rate monitor based on a thermal actuator and a pair of temperature sensors. The difference between the temperatures recorded at the two temperature sensors (T2-T1) increases as the flow rate increase.

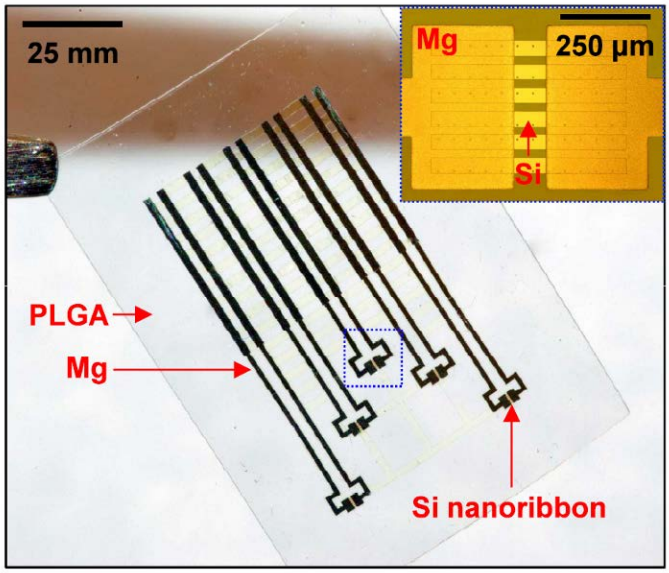

Figure 1.16 Bioresorbable pH sensor constructed with Si-NRs, Mg electrodes and PLGA substrates.

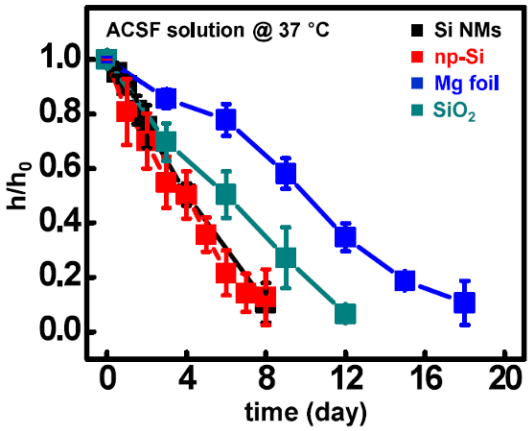

Figure 1.17 Hydrolysis kinetics of materials used in the bioresorbable pressure sensors. Normalized thickness (h/h_0) as a function of time during dissolution of individual materials in artificial cerebrospinal fluid (ACSF) at physiological temperature (37 °C). The initial thicknesses were 200 nm for Si nanomembranes (Si NMs), 80 μm for porous Si (p-Si), 80 μm for Mg foil, and 100 nm for SiO_2.

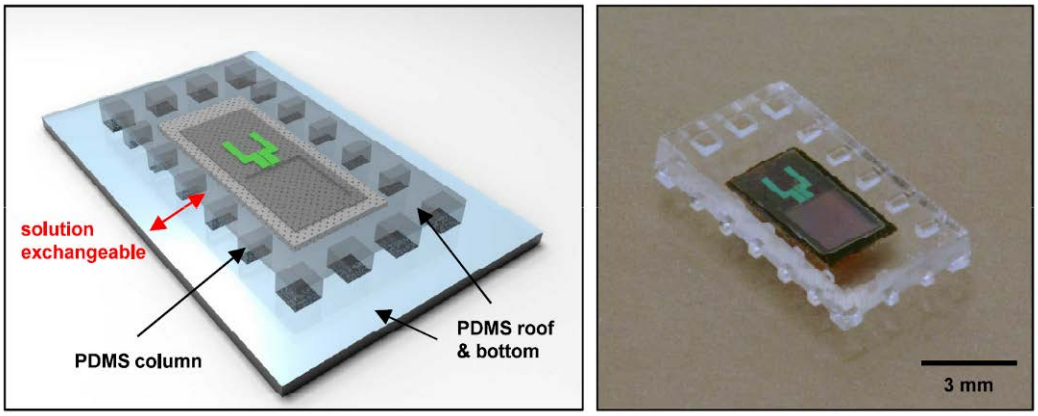

Figure 1.18 Schematic diagram (left) and image (right) of PDMS structure used as a simple mimic of the intracranial space.

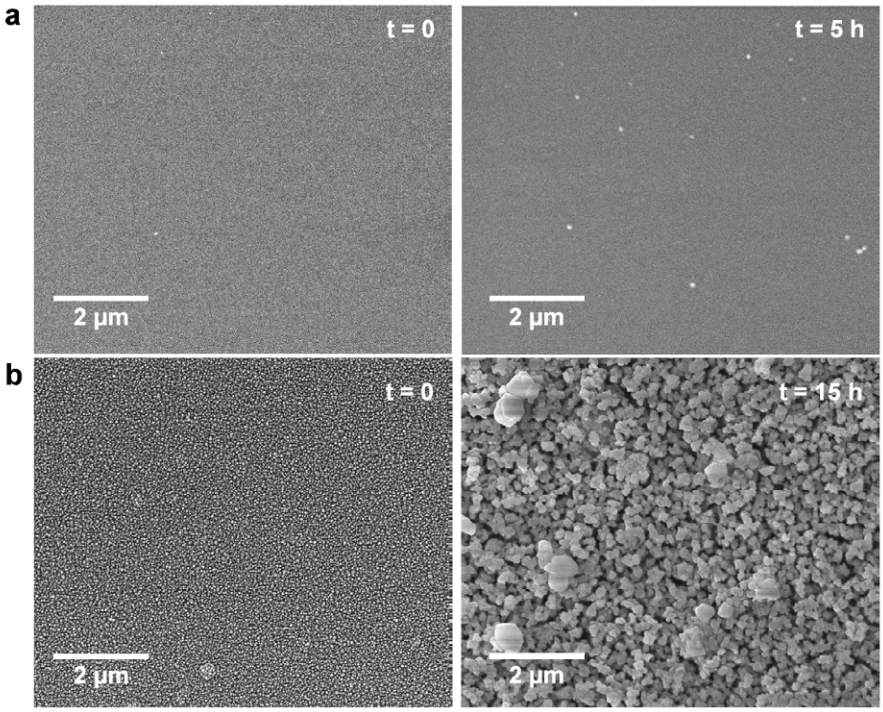

Figure 1.19 Scanning electron microscope (SEM) images of a) Si NMs and b) np-Si at the different stages of dissolution in buffer solution with pH 12 at 37 °C.

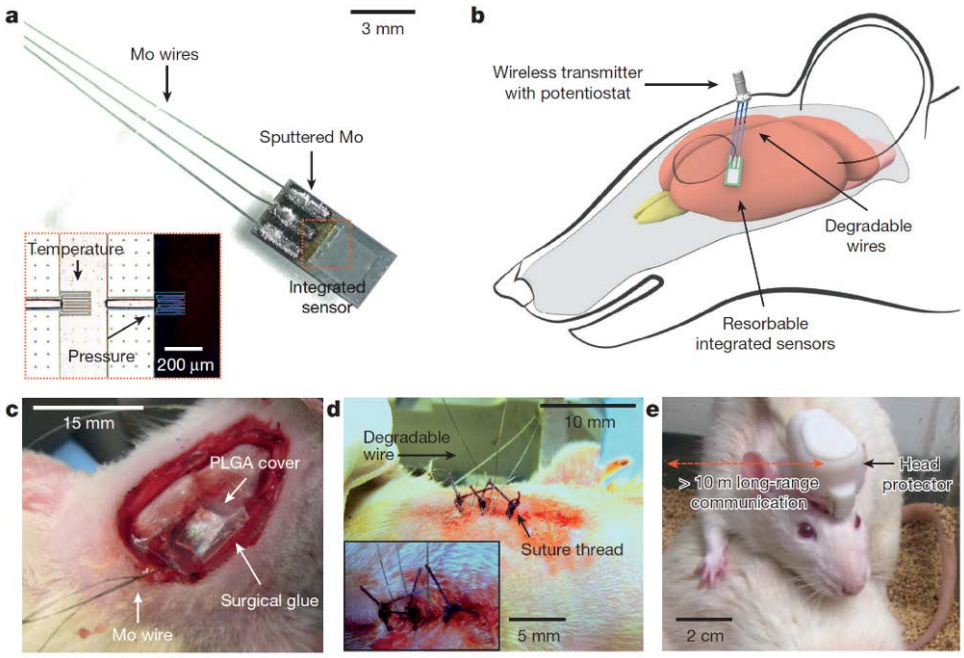

Figure 1.20 Bioresorbable interfaces between intracranial sensors and external wireless data-communication modules with percutaneous wiring. a, Image of bioresorbable pressure and temperature sensors integrated with dissolvable metal interconnects (sputtered molybdenum, Mo, 2 µm thick) and wires (Mo, 10 µm thick). The inset shows an optical micrograph of the serpentine Si-NM structures that form the sensing regions. The Si-NM that is not above the air cavity (left) responds only to temperature; the one at the edge of the air cavity (right) responds primarily to pressure. b, Diagram of a bioresorbable sensor system in the intracranial space of a rat, with electrical interconnects that provide an interface to an external wireless data-transmission unit for long-range operation. c, d, Demonstrations of c, an implanted bioresorbable sensor in a rat, and d, a sutured individual. A thin film of PLGA (~80 µm) and a degradable surgical glue (TISSEAL) seal the craniectomy defect to close the intracranial cavity. e, Healthy, freely moving rat equipped with a complete, biodegradable wireless intracranial sensor system.

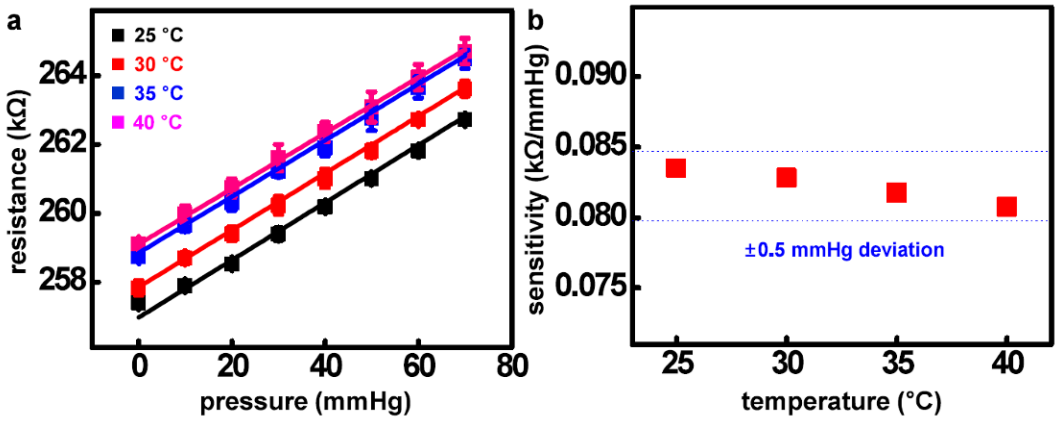

Figure 1.21 Calibration of the temperature dependent piezoresistivity. a) Resistivity variation to applied pressure at various temperatures (error bars represents standard deviation). b) Variation of sensitivity of resistivity to pressure associated with changes in temperatures. The change of piezoresistivity sensitivity is negligible across the expected range of brain temperatures.

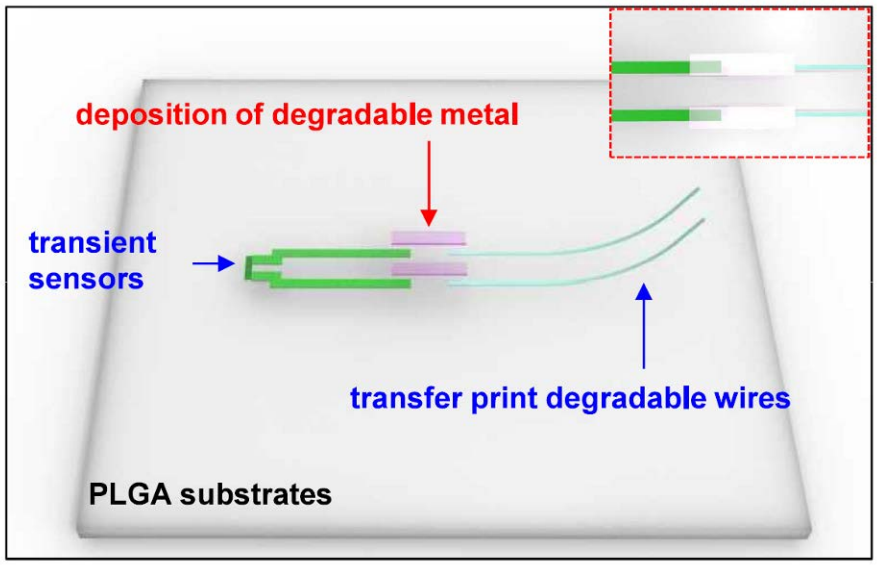

Figure 1.22 Strategy for interconnection between a bioresorbable device and degradable external wires on biodegradable polymer. Transfer printing the biodegradable wires (Mg or Mo) on the biodegradable polymer substrate (PLGA), and depositing dissolvable metal (Mo) between the wires and sensors yield the fully bioresorbable interface.

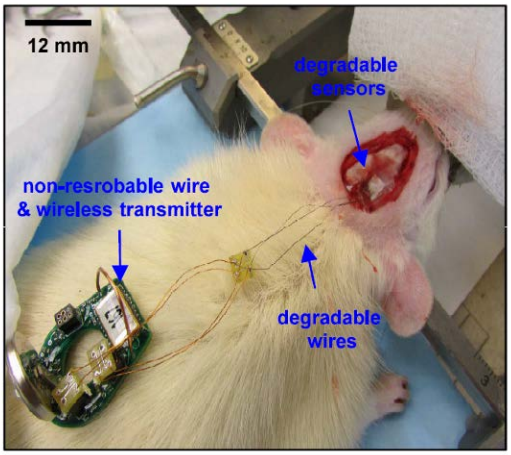

Figure 1.23 Image of the interface between the bioresorbable wires and the wireless transmitter.

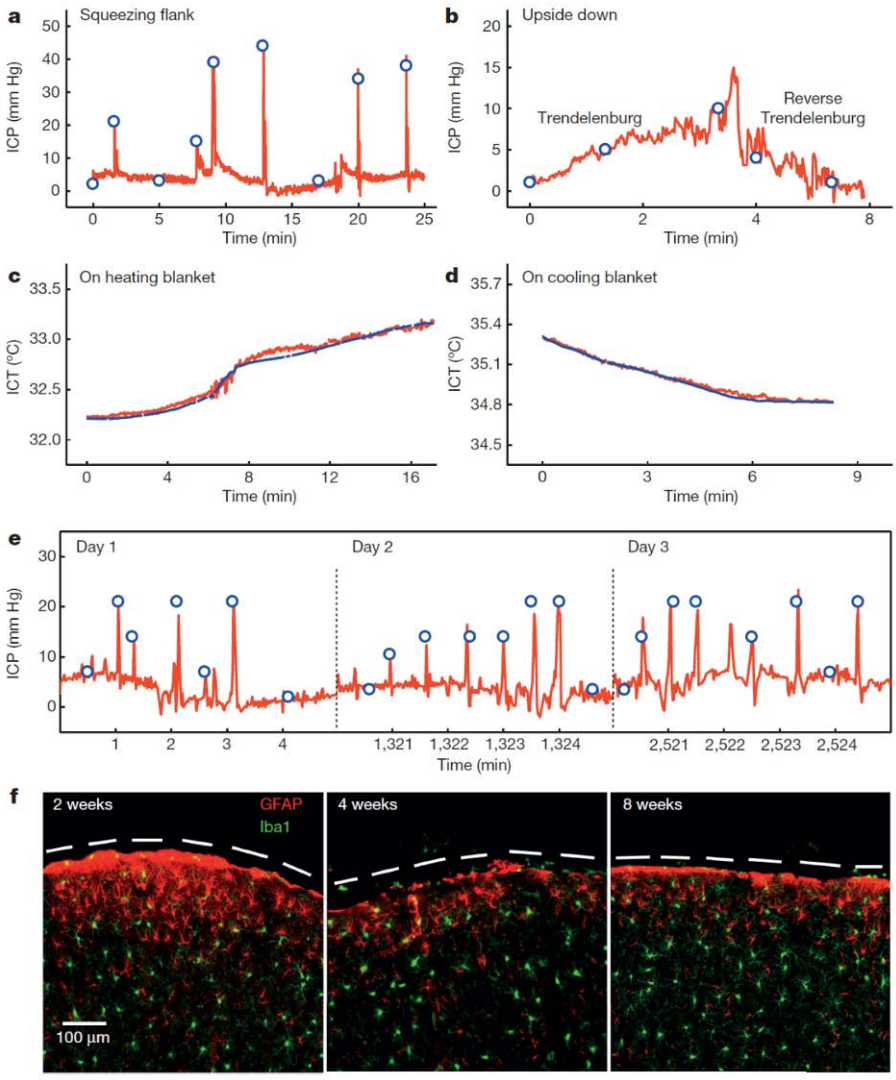

Figure 1.24 Wireless measurement of intracranial pressure and temperature with bioresorbable sensors implanted in live, freely moving animals. a–e, Red, data from a transient, bioresorbable sensor; blue, data from a commercial sensor. a, Real-time wireless measurements of ICP, showing transient increases induced by the Valsalva manoeuvre. b, *In vivo* observation of changes in ICP as a function of time in the Trendelenburg and reverse Trendelenburg positions. ICP increases in the 30° head-down position (Trendelenburg) as compared with the supine position, and decreases in the 30° head-up position (reverse Trendelenburg). c, Gradual increase and d, decrease in ICT due to application of a heating/cooling blanket. e, Measurements of ICP over three days reveal consistent responses from devices encapsulated with biodegradable polyanhydride. f, Confocal fluorescence images of the cortical surface beneath the dissolved device at 2, 4 and 8 weeks, showing the absence of inflammatory responses. The images are doubleimmunostained for GFAP (glial fibrillary acidic protein) to detect astrocytes (red), and Iba1 (ionized calcium-binding adaptor molecule 1) to identify microglia/macrophages (green). The dashed line indicates the site of the implant.

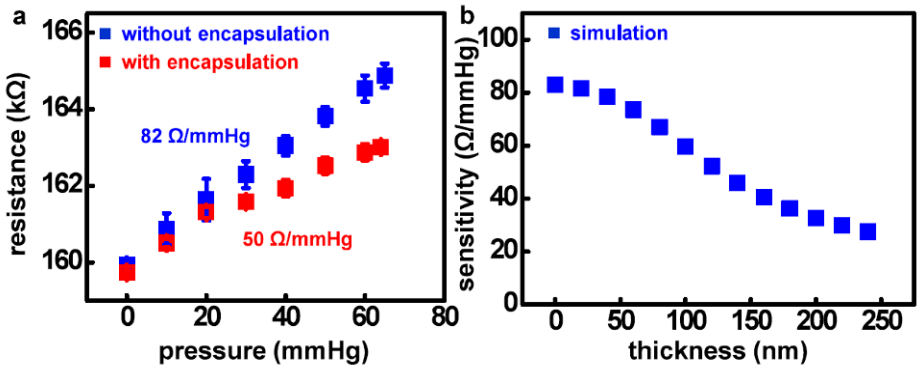

Figure 1.25 Effect of polyanhydride encapsulation on the response of the pressure sensor. a) Calibration curves before and after encapsulation. The calibration factor changes from 82 to 50 Ω/mmHg with 120 μm thick encapsulation (error bars represent standard deviation). b) The thickness dependent sensitivity simulated by FEM.

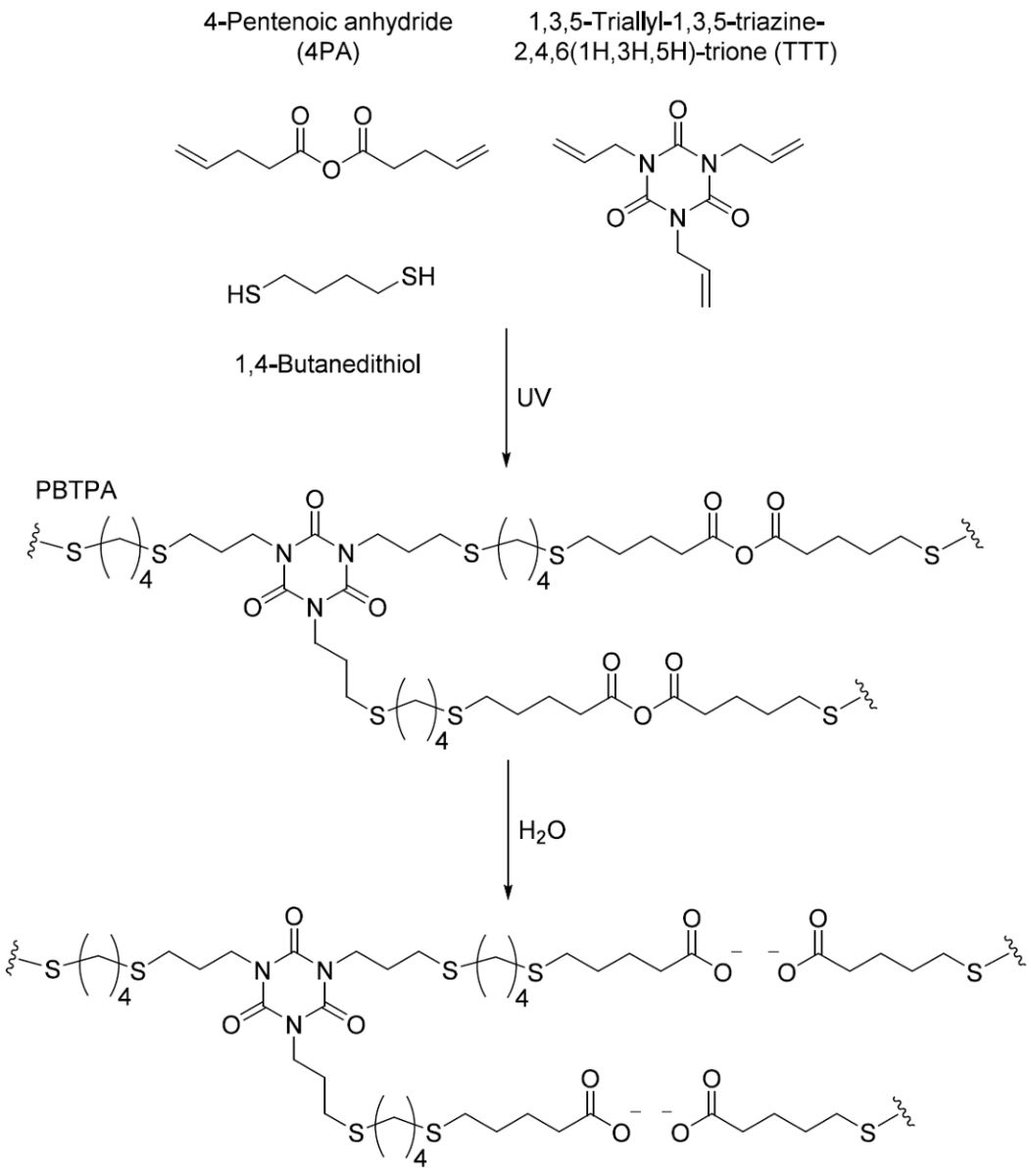

Figure 1.26 Chemistry of synthesis and hydrolysis of a biodegradable polymer (class of polyanhydride) for encapsulation.

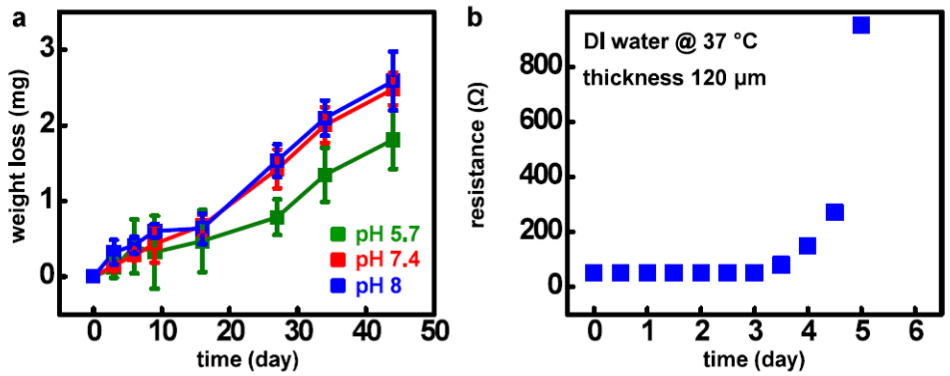

Figure 1.27 a) Dissolution kinetics and b) water permeability (tested by 300 nm thick Mg resistor) of polyanhydride encapsulation.

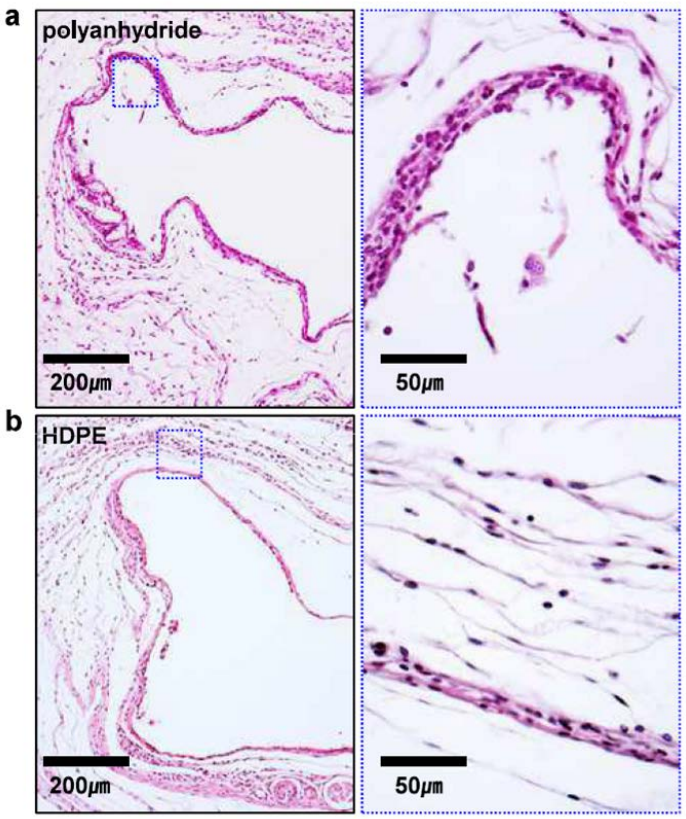

Figure 1.28 Hematoxylin and eosin (H&E) images of tissue around the implant site of a) polyanyhdride and b) HDPE after 14 days.

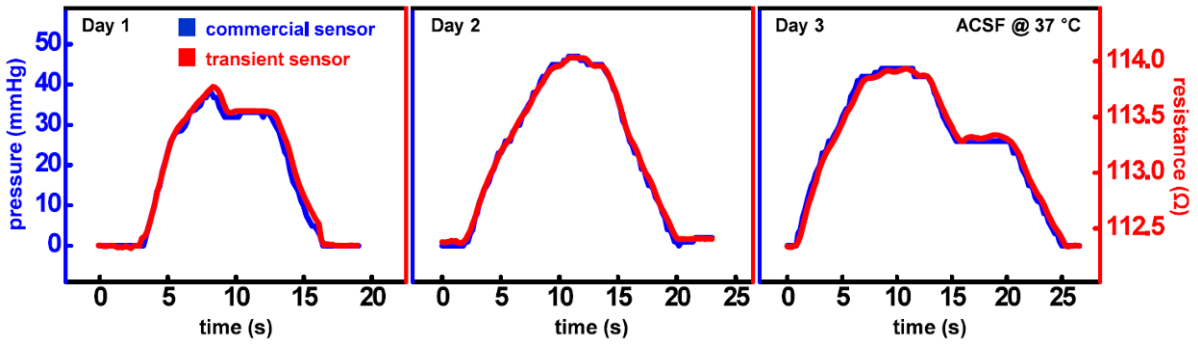

Figure 1.29 *In vitro* operation of bioresorbable pressure sensor with functional lifetime controlled with a biodegradable encapsulation layer.

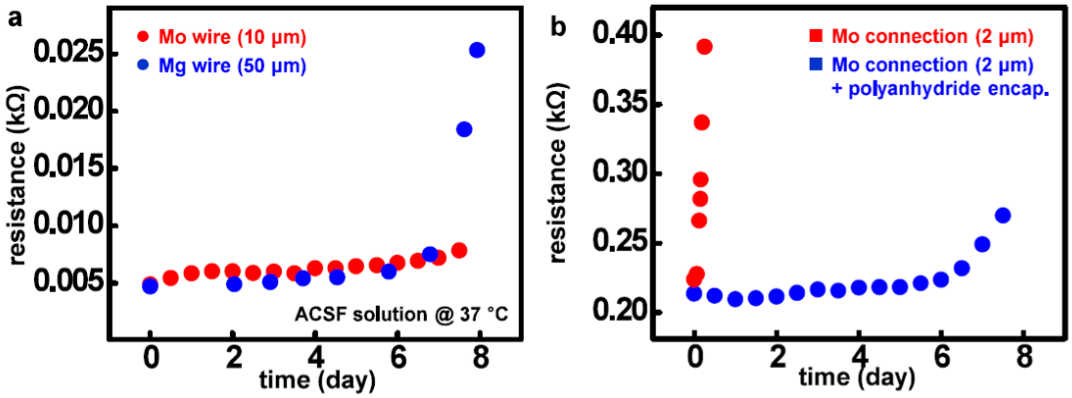

Figure 1.30 Effect of dissolution of metal wires and interconnects on the resistance. a) Increases in resistance of biodegradable metal wire (Mo, 10 μm; Mg, 50 μm) in ACSF at physiological temperature for ~a week. The change in resistance is negligible (below a few ohms) for a week. The resistance of Mg wire rapidly increases after 7 days due to its higher dissolution rate compared to Mo. b) Changes in resistance of Mo interconnections (~ 2 μm) during hydrolysis in ACSF at body temperature.

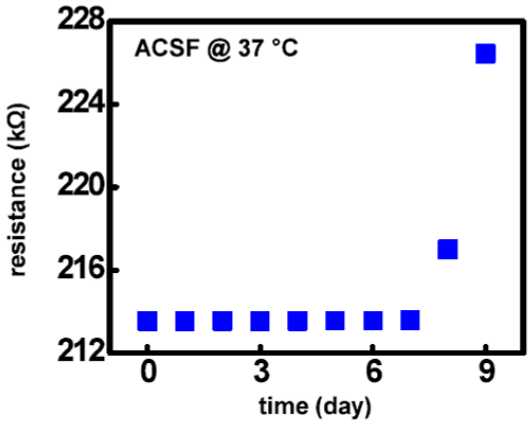

Figure 1.31 Resistance measurement of a pressure sensor with polyanhydride encapsulation with constant external pressure.

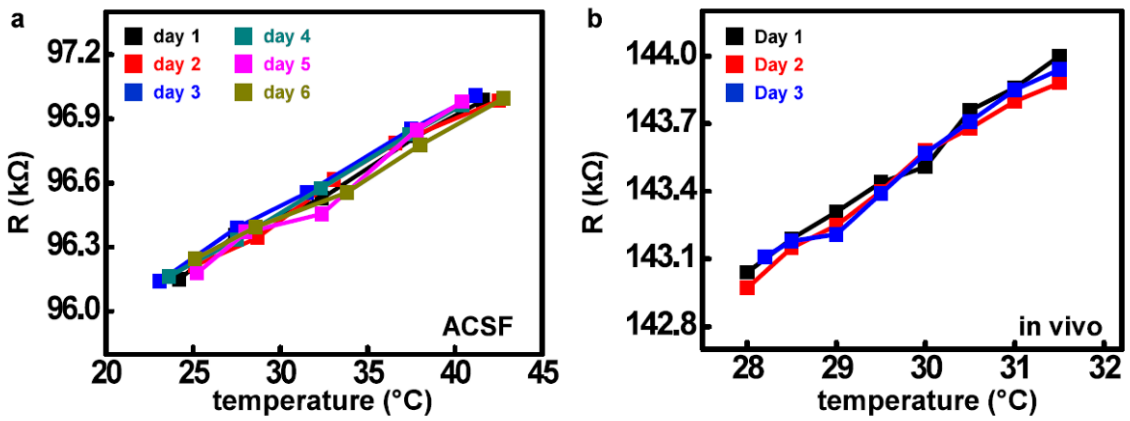

Figure 1.32 *In vitro* and *in vivo* demonstrations of biodegradable temperature sensors. a) Calibration curves for resistance to temperature indicate stable operation over 6 days in ACSF. b) Stable *in vivo* operation was demonstrated for three days. Sensors were encapsulated with a 120 μm thick layer of polyanhydride.

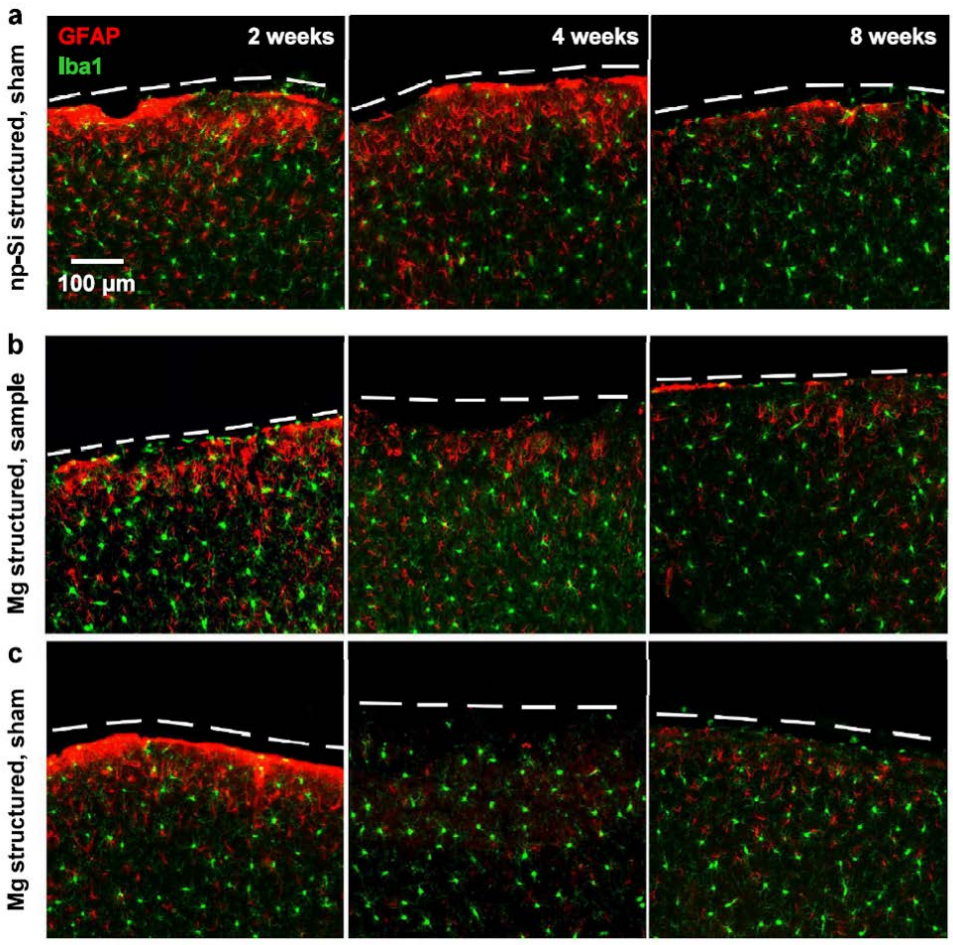

Figure 1.33 Confocal fluorescence images of the cortical surface. a) Series of images of the sham area (left side of brain) and the area underneath the np-Si pressure sensor (right side of brain). b) Image of the cortical surface at the site implanted with a Mg supported device and c) at the sham site.

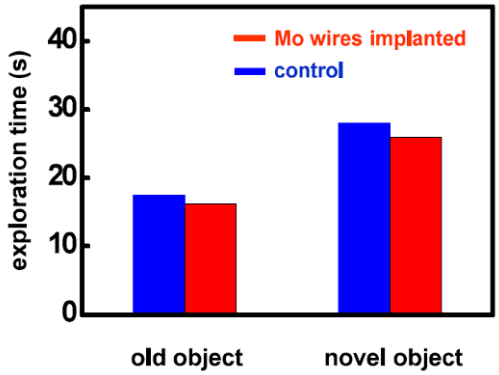

Figure 1.34 Animal behavior evaluation with transcutaneous wire implantation using novel object recognition test.

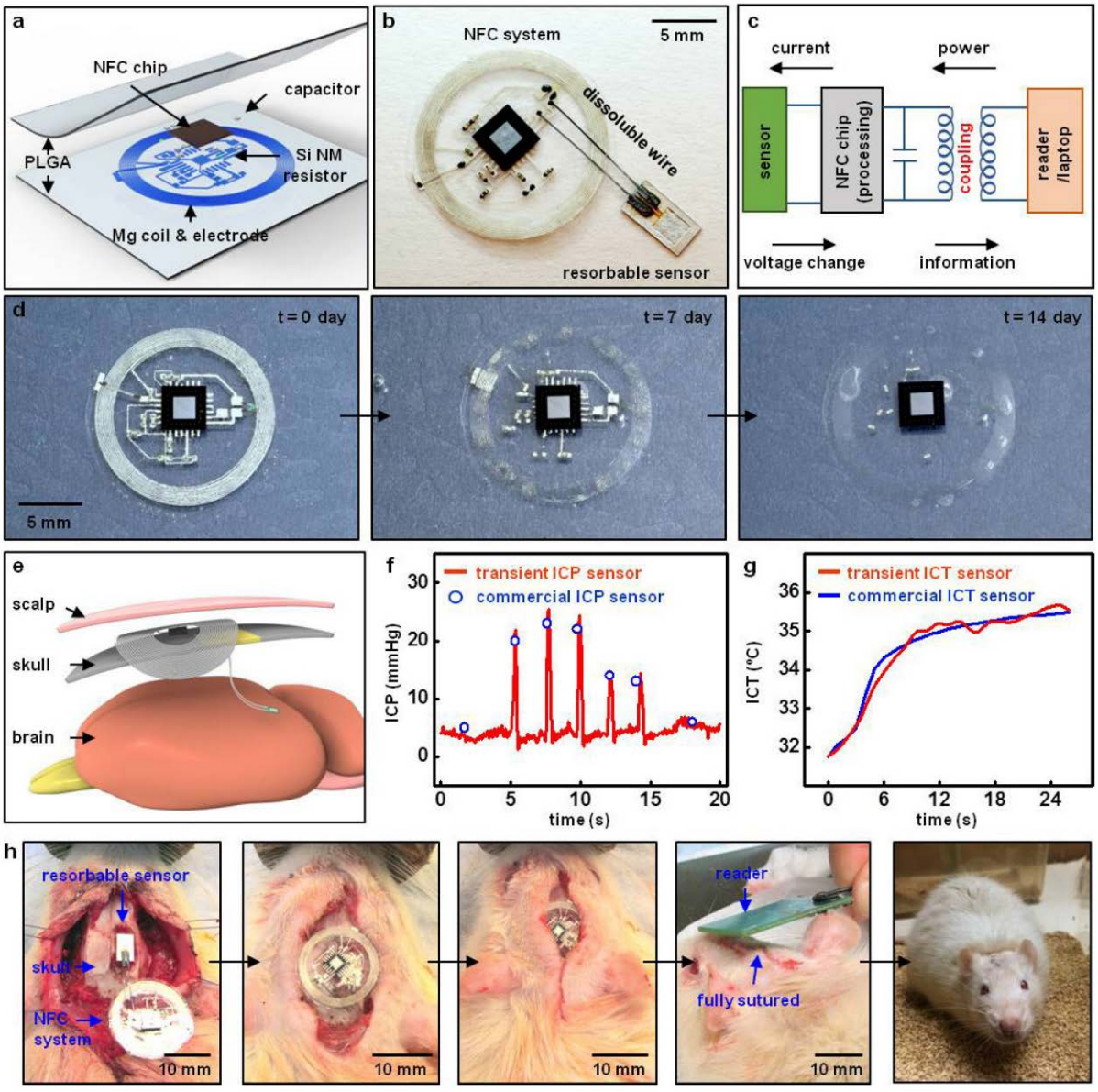

Figure 1.35 Fully implantable near-field communication (NFC) system with bioresorbable interface and intracranial sensors. a, Diagram of a fully implantable NFC system. This device uses a magnesium foil (~50 μm) for the inductive coil, interconnects and electrodes; patterned silicon nanomembranes (Si-NMs, ~300 nm) for resistors; conventional capacitors; and an advanced NFC microchip for data acquisition, processing and transmission. PLGA serves as the substrate and for encapsulation. The diameter of the entire device is about 15 mm. b, Image of this type of NFC system integrated with a bioresorbable pressure sensor. c, Diagram of the operational principles. d, Series of images showing accelerated dissolution of the NFC system inserted into an ACSF at 60 °C. e, Diagram of the implantation process. The bioresorbable sensors reside in the intracranial space, while the NFC system is located extracranially, on the outside surface of the skull, beneath the skin. Bioresorbable, thin metal wires interconnect the

Fig. 1.35 (cont.) NFC system and the sensors. f, Real-time wireless measurements of ICP, showing transient increases induced by the Valsalva manoeuvre (red, data obtained from a transient ICP sensor; blue, data obtained from a commercial ICP sensor). g, Increase in ICT owing to application of a heating blanket around the head, as determined by bioresorbable (red) and commercial (blue) sensors. h, Demonstrations of implantation and suturing in a rat model. A biodegradable surgical glue (TISSEAL) seals the intracranial space.

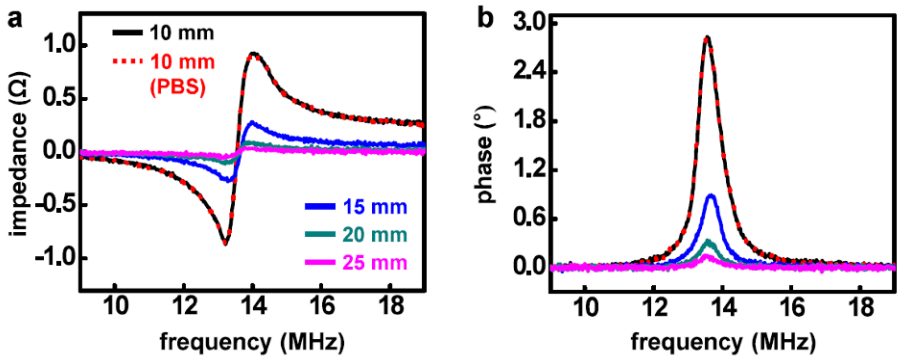

Figure 1.36 Frequency dependent a) impedance and b) phase of the NFC system at the different distance (black line; 10 mm, red dot; 10 mm with 2 mm barrier of phosphate buffer solution (PBS), blue line; 15 mm, cyan line; 20 mm, magenta line; 25 mm).

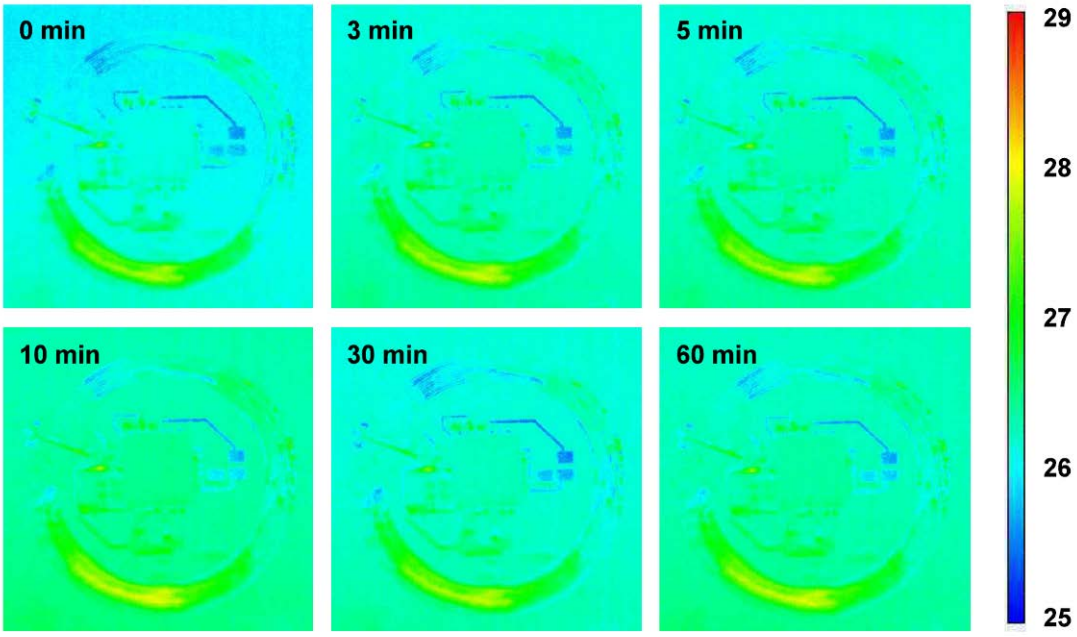

Figure 1.37 IR thermography of an NFC system during wireless operation in air.

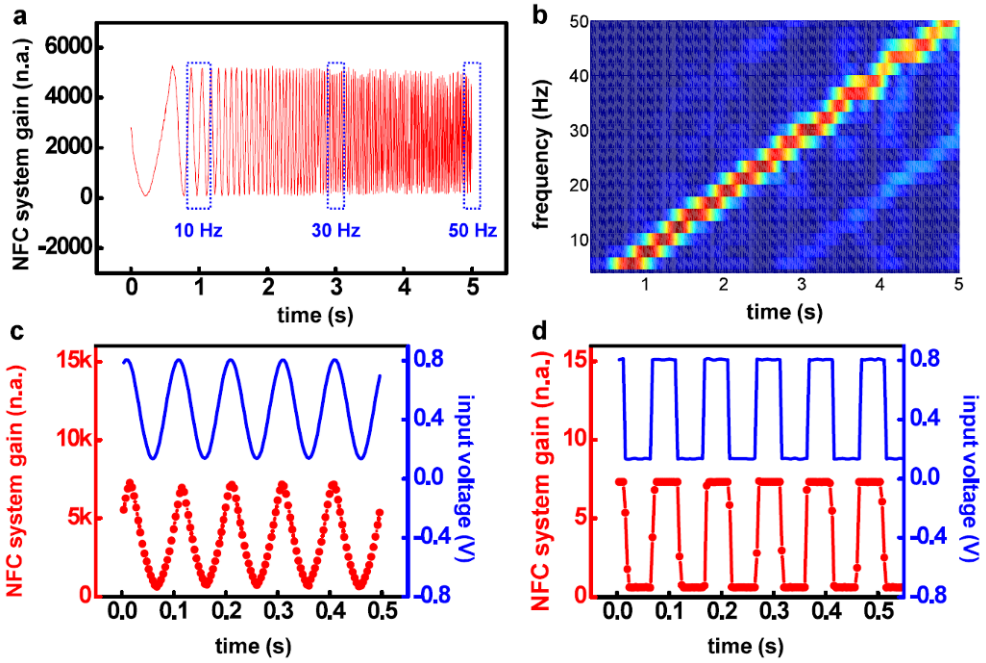

Figure 1.38 High sampling rate of NFC system. a) Wirelessly transmitted voltage sine waves with frequencies between 1 to 50 Hz. Maximum sampling rate of this system is 250 Hz. b) Spectrogram of swept sine wave in Figure 1.20f. High speed data acquisition of NFC system demonstrated with c) sine and d) square wave of 10 Hz frequency. (Red dot line is the data point measured by NFC system and blue line is input signal from signal generator.)

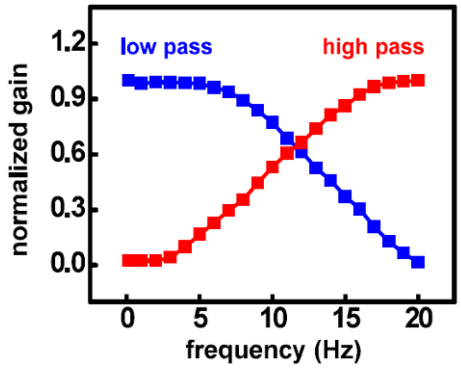

Figure 1.39 Gain response of programmed real-time high (red) and low (blue) pass filtering, performed by the NFC chip, as a function of frequency.

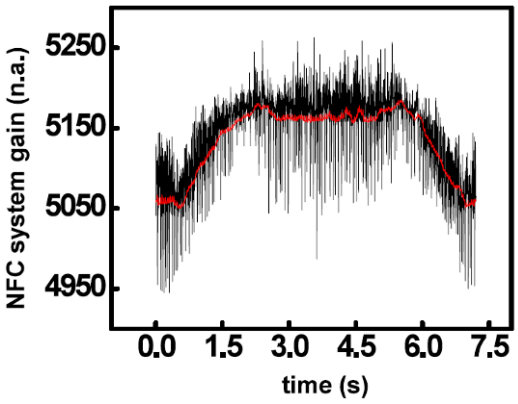

Figure 1.40 Comparison of filtered (red) and unfiltered (black) gain during pressure measurement. Two channels were measurement through NFC system at the same time. The filter function was loaded and performed in the chip.

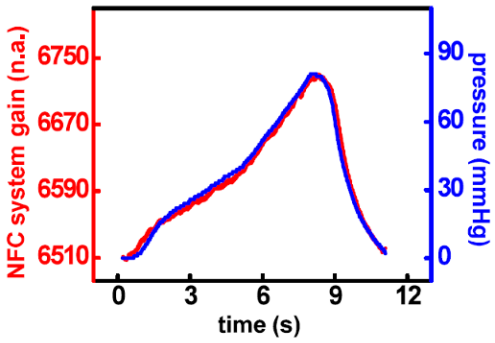

Figure 1.41 Response of a commercial pressure sensor (blue) and a wireless, biodegradable system (red) to time-varying pressure over a range relevant to intracranial monitoring.

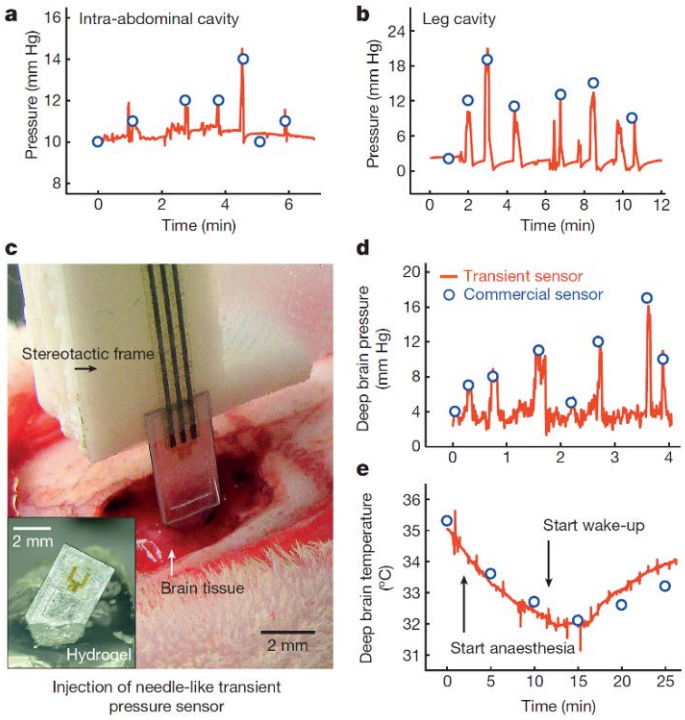

Figure 1.42 Application of bioresorbable sensors to various body cavities, and demonstration of an injectable format for deep brain monitoring. Red, data from a transient biodegradable sensor; blue, data from a commercial sensor. a, b, Pressures measured in a, intra-abdominal and b, leg cavities. c, Image showing *in vivo* injection of a needle-shaped biodegradable pressure sensor (using a magnesium foil support, ~80 μm thick) into the brain parenchyma with a stereotactic frame and arm. The inset shows a biodegradable pressure sensor inserted into hydrogel, as evidence of the sensor's robust mechanical construction. d, *In vivo* measurements of pressure in the deep brain. e, *In vivo* measurements of temperature in the deep brain during anaesthesia. The temperature drops during anaesthesia owing to reduced blood circulation, and returns to normal after awakening.

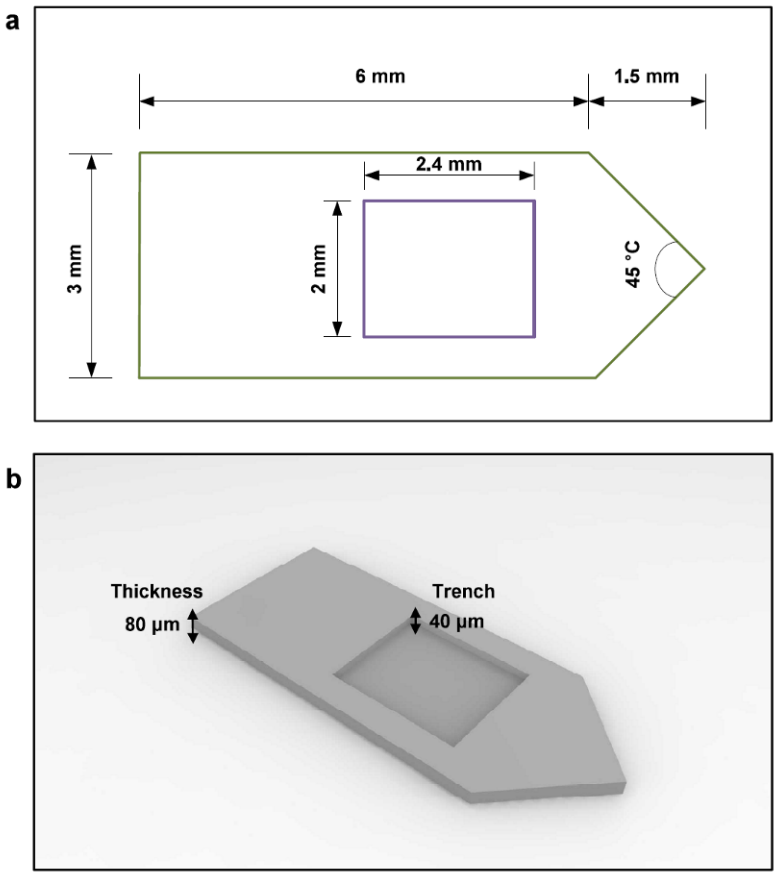

Figure 1.43 Geometry of needle substrates of pressure sensor. a) Lateral geometry and b) three-dimensional geometry of Mg needle substrates.

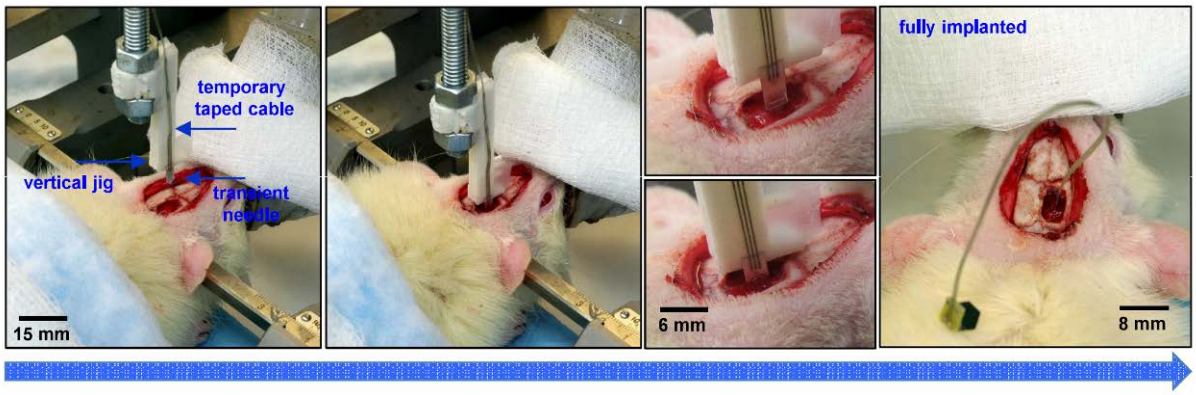

Figure 1.44 Surgical process for injectable form of biodegradable sensors. A needle shaped sensor was positioned with a jig. Lowering the jig causes the sharp edge of the device to penetrate into the deep brain.

1.8 References

1 Poole, J. E. Present guidelines for device implantation: clinical considerations and clinical challenges from pacing, implantable cardiac defibrillator, and cardiac resynchronization therapy. *Circulation* **129**, 383–394 (2014).

2 Brain, T. F. Guidelines for the management of severe traumatic brain injury. VI. Indications for intracranial pressure monitoring. *J. Neurotrauma* **24**, S37–S44 (2007).

3 Chamis, A. L. et al. Staphylococcus aureus bacteremia in patients with permanent pacemakers or implantable cardioverter-defibrillators. *Circulation* **104**, 1029–1033 (2001).

4 Hall-Stoodley, L., Costerton, J. W. & Stoodley, P. Bacterial biofilms: from the natural environment to infectious diseases. *Nature Rev. Microbiol*. **2**, 95–108 (2004).

5 Maytin, M. & Epstein, L. M. Lead extraction is preferred for lead revisions and system upgrades. *Circ. Arrhythm. Electrophysiol*. **3**, 413–424 (2010).

6 Boutry, C. M. et al. Towards biodegradable wireless implants. *Phil. Trans. R. Soc. A* **370**, 2418–2432 (2012).

7 Ott, K. et al. Retained intracranial metallic foreign bodies: report of two cases. *J. Neurosurg.* **44**, 80–83 (1976).

8 Vajramani, G. V. et al. Persistent and intractable ventriculitis due to retained ventricular catheters. *Br. J. Neurosurg*. **19**, 496–501 (2005).

9 Hwang, S.-W. et al. A physically transient form of silicon electronics. *Science* **337**, 1640–1644 (2012).

10 Irimia-Vladu, M. “Green” electronics: biodegradable and biocompatible materials and devices for sustainable future. *Chem. Soc. Rev*. **43**, 588–610 (2014).

11 Bettinger, C. J. & Bao, Z. Organic thin film transistors fabricated on resorbable biomaterial substrates. *Adv. Mater.* **22**, 651–655 (2010).

12 Luo, M., Martinez, A. W., Song, C., Herrault, F. & Allen, M. G. A microfabricated wireless RF pressure sensor made completely of biodegradable materials. *J. Microelectromech. Syst.* **23**, 4–13 (2014).

13 Brogan, M. E. & Manno, E. M. Treatment of malignant brain edema and increased intracranial pressure after stroke. *Curr. Treat. Options Neurol*. **17**, 327 (2015).

14 Liu, C. *Foundations of MEMS* Ch. 6 (Prentice Hall, 2011).

15 Moseley, P. T. & Crocker, J. *Sensor Materials* Ch. 4 (Institute of Physics Publishing, 1994).

16 Chang, H. et al. DNA-mediated fluctuations in ionic current through silicon oxide nanopore channels. *Nano Lett*. **4**, 1551–1556 (2004).

17 Zheng, G., Patolsky, F., Cui, Y., Wang, W. U. & Lieber, C. M. Multiplexed electrical detection of cancer markers with nanowire sensor arrays. *Nature Biotechnol*. **23**, 1294–1301 (2005).

18 Stern, E. et al. Label-free immunodetection with CMOS-compatible semiconducting nanowires. *Nature* **445**, 519–522 (2007).

19 Gentile, P., Chiono, V., Carmagnola, I. & Hatton, P. V. An overview of poly(lactic-co-glycolic) acid (PLGA)-based biomaterials for bone tissue engineering. *Int. J. Mol. Sci*. **15**, 3640–3659 (2014).

20 Hwang, S.-W. et al. Dissolution chemistry and biocompatibility of singlecrystalline silicon nanomembranes and associated materials for transient electronics. *ACS Nano* **8**, 5843–5851 (2014).

21 Kang, S.-K. et al. Dissolution behaviors and applications of silicon oxides and nitrides in transient electronics. *Adv. Funct. Mater*. **24**, 4427–4434 (2014).

22 Yin, L. et al. Dissolvable metals for transient electronics. *Adv. Funct. Mater*. **24**, 645–658 (2014).

23 Uslaner, J. M. et al. T-type calcium channel antagonism produces antipsychotic-like effects and reduces stimulant-induced glutamate release in the nucleus accumbens of rats. *Neuropharmacol*. **62**, 1413–1421 (2012).

24 Barth, K. N. M., Onesti, S. T., Krauss, W. E. & Solomon, R. A. A simple and reliable technique to monitor intracranial pressure in the rat: technical note. *Neurosurgery* **30**, 138–140 (1992).

25 Haure, P., Cold, G. E., Hansen, T. M. & Larsen, J. R. The ICP-lowering effect of 10° reverse Trendelenburg position during craniotomy is stable during a 10-minute period. *J. Neurosurg. Anesthesiol*. **15**, 297–301 (2003).

26 Morgan, P. W. Structure and moisture permeability of film-forming polymers. *Ind. Eng. Chem*. **45**, 2296–2306 (1953).

27 Meldrum, D. R. et al. Prospective characterization and selective management of the abdominal compartment syndrome. *Am. J. Surg*. **174**, 667–673 (1997).

28 Olson, S. A. & Glasgow, R. R. Acute compartment syndrome in lower extremity musculoskeletal trauma. *J. Am. Acad. Orthop. Surg*. **13**, 436–444 (2005).

29 Stiefel, M. F. et al. Reduced mortality rate in patients with severe traumatic brain injury treated with brain tissue oxygen monitoring. *J. Neurosurg*. **103**, 805–811 (2005).

30 Timofeev, I. et al. Extracellular brain pH with or without hypoxia is a marker of profound metabolic derangement and increased mortality after traumatic brain injury. *J. Cereb. Blood Flow Metab*. **33**, 422–427 (2013).

31 Suehiro, E. et al. Diverse effects of hypothermia therapy in patients with severe traumatic brain injury based on the computed tomography classification of the traumatic coma data bank. *J. Neurotrauma* **32**, 353–358 (2015).

32 Mittal, R. et al. Use of bio-resorbable implants for stabilization of distal radius fractures: the United Kingdom patients' perspective. *Injury* **36**, 333–338 (2005).

33 Ye, T. et al. Management of grade III open dislocated ankle fractures: combined internal fixation with bioabsorbable screws/rods and external fixation. *J. Am. Podiatr. Med. Assoc*. **101**, 307–315 (2011).

34 Yin, L., Bozler, C., Harburg, D. V., Omenetto, F. & Rogers, J. A. Materials and fabrication sequences for water soluble silicon integrated circuits at the 90 nm node. *Appl. Phys. Lett.* **106**, 014105 (2015).

35 Huang, X. et al. Biodegradable materials for multilayer transient printed circuit boards. *Adv. Mater*. **26**, 7371–7377 (2014).

CHAPTER 2: BIORESORBABLE PRESSURE SENSORS WITH THERMALLY-GROWN SILICON DIOXIDE ENCAPSULATION FOR MONITORING CHRONIC DISEASES

2.1 Introduction

Measurements of pressure in organ systems ranging from the brain, eyes, bladder, and blood vessels form an essential diagnostic basis for assessment of patient health and progression of diseases such as glaucoma (intraocular pressure), hypertension (blood pressure), traumatic brain injury, and hydrocephalus (intracranial pressure). Capabilities in precise, continuous monitoring of pressure can, therefore, be critically important in defining treatment protocols that decrease the rate of morbidity and increase the pace of recovery[1-3]. Conventional sensor technologies designed for this purpose are available in the form of accurate, implantable devices that must be surgically extracted after a patient has emerged from the most critical stages of the recovery process. These procedures are costly and they can expose the patient to significant pain and risks for complications[4]. Additionally, the devices can serve as a nidus for infection[5,6] and for immune-mediated inflammatory responses[7]. Emerging classes of bioresorbable electronic sensor systems have the potential to address these disadvantages. Here, all of the constituent materials dissolve in biofluids over well-defined periods of time, with biologically benign end products. This process naturally eliminates the devices after a useful functional period, thereby bypassing surgical extraction. Examples of bioresorbable devices in the recent literature include biophysical sensors of pressure, temperature, flow rate, and motion[8,9] together with several types of biochemical sensors[8,10]. Additional components range from thermal actuators[8] to neural electrodes[11,12], power supplies[13], and controlled drug-delivery vehicles[14,15]. Published animal

model studies include deployments in the intracranial, intra-abdominal and leg cavities[8], on cortical surfaces[11,12], and in subdermal regions[15,16].

Although recently reported bioresorbable pressure sensors offer sensitivity and accuracy comparable to those of conventional, non-resorbable analogs, they offer stable operation over a period of only several days, which is insufficient for many applications[8,9]. Extending this operational lifetime to several weeks involves daunting challenges in materials science and device design that follow directly from the requirement that the systems must ultimately dissolve completely, at a molecular level, without adverse effect. This difficulty is inherent to all classes of implantable, bioresorbable systems because immersion in biofluids immediately initiates processes of bioresorption. The most effective means to prolong the lifetime relies on passive encapsulating layers that delay the time required for biofluids to come into contact with the active materials. Biodegradable polymers such as silk fibroin[15,16], poly(L-lactide) (PLLA)[9], and poly(lactic-co-glycolic acid) (PLGA)[13] are attractive for such purposes, partly because they can be formed easily by spin-coating or molding. The hydrophilic nature of these materials, however, leads to swelling and water permeation, thereby causing premature fracture, buckling and dissolution of the underlying materials. Inorganic alternatives based silicon dioxide[17,18], silicon nitride[18], and various metal oxides[19] formed by chemical or physical vapor deposition offer exceptionally slow rates of dissolution without these other adverse responses. Nevertheless, these materials are of limited practical utility due to extreme difficulties in forming coatings without cracks or pinholes that can allow water to pass.

Recent work demonstrates that layers of silicon dioxide thermally grown on device-grade silicon wafers (t-SiO_2) can serve as biofluid barriers with defect-free, material perfection over large areas[20,21]. Systematic studies show that the eventual failure follows from hydrolysis

reactions, as opposed to water permeation through the material or through defects in the films. Specifically, t-SiO_2 dissolves in simulated biofluids at physiological temperatures with rates of several hundredths of a nanometer per day, to yield silicic acid as a biodegradable end product[18,20,21]. These observations suggest the use of ultrathin layers of t-SiO_2 as bioresorbable encapsulation layers to enable stable operating periods in the range of weeks or longer. This materials strategy has the potential to yield devices that can address operational lifetime requirements for envisioned clinical applications, including those in monitoring of pressure for traumatic brain injury (up to one week)[22] and glaucoma (several months), as examples. The principal design strategy includes: (1) t-SiO_2 barriers that prevent interactions with biofluids throughout the desired monitoring period, but with thicknesses sufficiently small to allow complete bioresorption within a reasonable timeframe, typically less than a year; (2) structural components that dissolve in a manner that does not affect the measurement accuracy; and (3) interlayer bonding approaches that prevent interfacial water penetration from the periphery.

Here, we demonstrate materials, device structures, fabrication methods that adhere to this strategy. The overall approach relies on bonding of a pair of silicon-on-insulator wafers using adhesion layers of amorphous silica formed by calcination of poly(dimethylsiloxane) (PDMS). Eliminating the handle wafers after bonding yields ultrathin, inorganic bioresorbable electronic devices with robust biofluid barriers that allow stable operation over extended periods of time. Data on the biodistribution of dissolved silicon in mice at five weeks following implantation of intracranial sensors formed in this manner, together with assessments of the hematology (complete blood count) and the blood chemistry confirm their nontoxicity and biodegradability. Measurements of intracranial pressures in rats over 25 days illustrate high accuracy and low drift, with overall performance that compares favorably to that of non-resorbable clinical standards.

The results not only establish routes to bioresorbable pressure monitoring technologies that meet requirements for clinical use, but they also serve as a generalizable platform for broad classes of bioresorbable electronic devices that can offer stable operating characteristics over long periods of time.

2.2 Experiments

The procedures for fabrication of bioresorbable pressure and temperature sensors with thermal SiO_2 biofluid barriers began with mechanical back-grinding (Syagrus Systems, USA) to reduce the total thickness of a silicon-on-insulator (SOI-A) wafer (top Si ~200 nm, buried SiO_2 ~1 μm, Si wafer ~100 μm; SOITEC, France) prior to device fabrication. Solid-state diffusion of phosphorus at 950^{o}C followed by photolithography and reactive ion etching (Plasma-Therm RIE) defined silicon nanomembrane strain gauges (Si NM SGs) and temperature gauges (TGs) in the top Si of SOI-A. Electron-beam (e-beam) evaporation of SiO_2 pellets (99.99%; Kurt J. Lesker Company, USA) formed a layer of SiO_2 (~600 nm) on top. Photolithography and deep reactive ion etching (STS Pegasus ICP-DRIE) defined an array of vent holes (area: 100 μm x 100 μm) through the thickness of SOI-A. Photolithography and ICP-DRIE formed a square trench with dimensions of 200 μm x 200 μm x 10 μm on a separate SOI wafer (SOI-B, top Si ~15 μm, buried SiO_2 ~600 nm, Si wafer ~85 μm after mechanical grinding; University Wafer, USA).

Wafer bonding of SOI-A (silicon sensors) and SOI-B (silicon trench) involved spin-coating a layer of diluted poly(dimethylsiloxane) (PDMS, part A/part B/hexane = 10:1:100, Sylgard 184; Dow Corning, USA) at a speed of 3000 rpm for 30 seconds on SOI-B, partially curing the PDMS by heating the wafer at 110 ^{o}C for 1 minute, transferring SOI-A on top of the SOI-B in a manner that aligned the SGs of SOI-A directly above the trench of SOI-B, pressing

the wafers together in a steel vise (Toomaker's vise; Tormach, Inc., USA), and fully curing the PDMS by placing the vise in a 70 ^{o}C convection oven for 2 hours bonded the wafers. Heating the vise in a furnace, by raising the temperature to 550^{o}C over 2 hours and keeping there for 2 more hours, converted the PDMS adhesion layer to amorphous silica.

Then, ICP-DRIE removed the top Si wafer (SOI-A) of the bonded sample to expose the buried oxide. Wet etching in a buffered oxide etchant (BOE, 6:1; Transene Company Inc., USA) reduced the thickness of this oxide to the desired value (~10 nm). Patterned wet etching exposed square areas (~100 μm x 100 μm) of Si NM in the four corners. Profilometer (Alpha Step D-500; KLA Tencor, USA) measurements confirmed the thickness of the buried oxide, with additional wet etching as needed to reach the desired value. Sputtering a layer of molybdenum (~100 nm) followed by patterning and wet etching formed metal contact pads (area: 150 μm x 150 μm) on top of the four exposed areas of Si NM. Spin-coating a layer of photoresist on the top surface, etching bottom Si wafer and buried oxide (SOI-B) by ICP-DRIE and wet etching in BOE, and removing the photoresist by descum process (March RIE) completed the fabrication.

2.3 Results and Discussion

Figure 2.1a shows the steps for fabrication, beginning with formation of silicon nanomembrane (Si NM) sensors on a silicon-on-insulator wafer (SOI-A, top Si ~200 nm, buried SiO_2 ~1 μm, Si wafer ~100 μm after mechanical grinding; SOITEC, France). Solid-state diffusion of phosphorus at 950 ^{o}C followed by photolithography and reactive ion etching (Plasma-Therm RIE) yields piezoresistive strain gauges in the top Si. Electron beam evaporation forms a coating of SiO_2 (eb-SiO_2, ~600 nm) that defines the thickest region of the sensing diaphragm of the final device. Photolithography and deep reactive ion etching (STS Pegasus

ICP-DRIE) create an array of holes (area: 100 μm x 100 μm) through the thickness of the wafer to release gaseous produces of the calcination process described subsequently. Patterning and etching the top Si layer of a second SOI wafer (SOI-B, top Si ~15 μm, buried SiO_2 ~600 nm, Si wafer ~85 μm after grinding; University Wafer, USA) creates a trench with dimensions of 200 μm x 200 μm x 10 μm. Spin-coating a thin layer of poly(dimethylsiloxane) (PDMS) on SOI-B allows bonding to SOI-A via thermal curing while applying pressure with a steel vise (Tormach, Inc., USA). Heating the vise in a furnace at 550 ^{o}C for 2 hours calcines the PDMS adhesion interlayer to yield an amorphous silica material (~200 nm) via a thermal oxidative degradation process[23]. Gaseous by-products such as carbon dioxide and water escape the bonding interface via the vent holes, leaving behind a smooth film of silica. Figure 2.2 shows scanning electron microscope (SEM) and atomic force microscope (AFM) images. A single broad peak at ~-110 ppm in the ^{29}Si NMR spectrum of the silica (Fig. 2.3) confirms full conversion of PDMS (no peak around -21 ppm, where $SiO_2(CH_3)_2$ would appear) into amorphous SiO_2 (Si-(O-Si)$_4$, Q_4 site). Electron dispersive spectroscopy (EDS) also confirms the absence of carbon. Removing the handle wafer of SOI-A by ICP-DRIE exposes the buried oxide underneath, to allow thinning to a desired thickness (~10 nm) by immersion in a buffered oxide etchant. Patterned wet etching exposes the Si NM in the four corners, to allow formation of electrical contact pads (area: 150 μm x 150 μm) using bioresorbable metals (molybdenum, 100 nm). ICP-DRIE followed by wet etching eliminates the handle silicon and buried oxide of SOI-B, respectively.

Figure 2.1b shows a photograph of a representative device, with size and weight of 1.3 mm x 1.3 mm x 16 μm and ~60 μg, respectively. The system consists of four Si sensors, two of which serve as strain gauges (SGs, blue) and two as temperature gauges (TGs, red), depending on their position relative to the trench (Fig. 2.1c). The partial extension of SGs over the trench as

part of a floating diaphragm yields a response that depends on the mechanical equilibrium between the pressures of the surroundings and that of the air trapped inside the trench. The TGs are not located over the trench and are therefore unresponsive to changes in pressure. These four gauges combine to form a Wheatstone bridge circuit to compensate temperature effects on the piezoresistive response of the SGs[24].

A magnified view of the diaphragm appears in Figure 2.1d. Two gray lines (width ~5 μm) represent etched regions of the Si NM that isolate each SG (pink, width ~8 μm) from the surrounding silicon. The diaphragm has an area of 200 μm x 200 μm, defined by lateral dimensions of the trench, and consists of a tri-layer of thermal SiO_2 (t-SiO_2, ~10 nm), monocrystalline Si (~200 nm), and eb-SiO_2 (~600 nm). The t-SiO_2 layer, derived from the buried oxide of the SOI-A wafer, insulates the Si devices from exposure to biofluids, thereby extending their functional lifetime. The eb-SiO_2 layer constitutes the thickest part of the diaphragm, and serves to increase the vertical separation between the neutral mechanical planes of the SGs and the bulk membrane, thereby improving the response of the SGs to pressure.

Three-dimensional finite element analysis (3D-FEA) provides insights into the mechanics of pressure sensing using these constructs. Distributions of principal strain and vertical displacements associated with the diaphragm under an external pressure of 40 mmHg above atmospheric appear in Figure 2.1e. The maximum strain for any applied pressure over the range of interest occurs along the edge of the trench, where the SGs are located. The relationship between the resistance of a SG and pressure is linear with a slope of -0.13 Ω/mmHg, which corresponds to a gauge factor of about -20.9, consistent with theory (see Methods and Fig. 2.4 for details). The value of the gauge factor follows from the heavy doping of the top Si (step 1 in Fig. 2.1a) needed to allow phosphorus atoms to diffuse through its thickness to the base (Fig.

2.5), at the location of electrical contact pads formed as a result of wafer bonding and etching (steps 4-7)[25,26]. Reducing the thickness of the Si NM (~50 nm), increasing the area of the diaphragm (~500 μm x 500 μm), and introducing serpentine designs in the SGs can improve the pressure sensitivity (Fig. 2.6). Measurements of the resistance of the TG as a function of temperature reveal a linear response with a temperature coefficient of resistance (TCR) of 0.0012/^{o}C, which lies within a range of expected values for monocrystalline silicon (Fig. 2.7)[26,27]. Changes in pressure sensitivity due to changes in temperature within the relevant ranges for the intracranial space (34-40 ^{o}C) induce errors in measured pressures that are less than ±0.4 mmHg (Fig. 2.8).

In vitro evaluations that mimic thermodynamic conditions inside the intracranial space illustrate the functional capabilities of the device. An airtight plastic chamber filled with artificial cerebrospinal fluid (ACSF, pH 7.4) at physiological temperature (37 ^{o}C) and connected via tubes to a commercial pressure sensor (Neulog, USA) and a syringe allows measurement and control of pressure, respectively (Fig. 2.9). Comparing voltage responses of the sensor (red, V_s = 2.5 V) with the measured pressures (blue) for values over a range relevant to intracranial monitoring reveals a linear correspondence (Figs. 2.1f and 2.10a). The level of noise in the response of the bioresorbable sensor, evaluated as the difference between the pressures measured by bioresorbable and commercial sensors (noise floor less than ±0.8 mmHg), lies within ±1 mmHg in the range of 0-30 mmHg and within ±3 mmHg in the ranges above (Fig. 2.10b). These numbers meet the intracranial pressure (ICP) monitoring standards defined by the Association for the Advancement of Medical Instrumentation (AAMI) (that is, a functional range of 0-100 mmHg, accuracy of ±2 mmHg in the range of 0-20 mmHg, and maximum error less than ±10 % in the range of 20-100 mmHg)[28]. Comprehensive results from continuous *in vitro* operation over

a period of 22 days reveal variations in pressure sensitivity and baseline within ±1.5 % and ±2.5 mmHg, respectively (Fig. 2.11). The observed baseline drift is within the expected ranges specified for a clinical fiber optic ICP monitor (that is, ±2 mmHg maximum in the first 24 hours and ±1 mmHg per day thereafter)[29].

The key feature of this system is that the constituent materials are water soluble, with biocompatible end products. Dissolution of Si and SiO_2 yields silicic acid $Si(OH)_4$ via hydrolysis, according to $Si + 4H_2O \rightarrow Si(OH)_4 + 2H_2$ and $SiO_2 + 2H_2O \rightarrow Si(OH)_4$, respectively. Figure 2.12a shows the kinetics, evaluated as changes in thicknesses of films of silicon oxides obtained by thermal oxidation, electron beam evaporation, and PDMS calcination in ACSF at T = 37 ^oC. The thicknesses of t-SiO_2 and eb-SiO_2 layers can be quantified by spectroscopic reflectometry (MProbe), while those of the silica adhesion layer can be assessed most effectively by profilometry (Alpha Step) due to non-uniformities in film thickness that follow from calcination. Figure 2.13 shows the steps for fabricating arrays of square patterns of silica used in the study, along with an image of these structures. The layers of t-SiO_2, eb-SiO_2 and silica dissolve at rates of 0.11 ± 0.01, 13.6 ± 1.6, and 129 ± 9 nm/day, respectively. The rates of dissolution of single-crystalline silicon and biodegradable metals (Mo, Mg) appear elsewhere[8,11]. These rates, taken together with the overall structures of the devices, yield estimated times for full dissolution of ~400 days. By decreasing the thickness of the trench (~10 μm), this time can be reduced to approximately 290 days without significantly compromising the sensor response.

Figure 2.12b shows a schematic illustration of a set-up designed to dissolve bioresorbable sensors at accelerated rates by immersion in phosphate-buffered saline (PBS, pH 7.4) at T = 95^oC in a plastic bottle. Employing a test design in which the sensor uses a t-SiO_2 substrate (by omitting step 8 in Fig. 2.1a) allows unidirectional thinning of component layers in sequence from

top to bottom. Figure 2.12c presents optical micrographs collected at various stages of dissolution. Complete hydrolysis of the t-SiO_2 layer leads to exposure of the Si NM within 5 hours; fast and non-uniform dissolution of the silicon creates a rough surface profile, which appears as dark shades under the microscope. The eb-SiO_2 and silica adhesion layers disappear within 20 hours, followed by the Si trench (outer gray region) in 80 hours. Complete disintegration leaves only the surface of the t-SiO_2 substrate with a shallow feature of surface relief (pink).

The use of t-SiO_2 as a defect-free barrier to prevent biofluid penetration to the Si device layer is critically important to the robust, long-lived operation. The functional lifetime is proportional to the thickness of the t-SiO_2 (Fig. 2.12d)[20]. Calibration curves of a bioresorbable pressure sensor (~10 nm t-SiO_2) collected at constant time intervals after immersion of the device in PBS at T = 95°C indicate highly uniform pressure responsivity in the first 3 hours followed by rapid transience. Operational failure follows from formation of holes or cracks in the diaphragm after dissolution of the t-SiO_2.

Evaluating the biodistribution of dissolved silicon, the hematology (complete blood count), and the blood chemistry of mice implanted with bioresorbable intracranial sensors provides insights into the body reactions to these devices as bioresorbable implants. Use of miniaturized devices (size: 750 μm x 750 μm x 11 μm; weight ~12 μg) without t-SiO_2 encapsulation accelerates the dissolution, thereby facilitating evaluations over a five-week period of study. The surgical procedure includes opening a craniectomy defect penetrating through the dura, implanting the sensor, and sealing the intracranial cavity using a drop of biodegradable tissue adhesive (TissueSeal, USA).

Figure 2.14a shows concentrations of silicon in liver, spleen, heart, kidney, brain, and lung tissues explanted from mice at 1, 3, and 5 weeks after implantation, measured by inductively coupled plasma optical emission spectrometry (ICP-OES; see Methods for sample preparation steps). The results indicate deposition of silicon at higher concentrations in spleen, heart, and lung tissues than in the brain, where the device is located, 1 week after implantation. This observation can be attributed to fast turnover of CSF volumes in mice (12-13 times per day in mice; 3-4 times in humans)[30]. The CSF circulates through the brain, then joins the bloodstream by bulk reabsorption via arachnoid villi, transporting dissolved silicic acids to other organs. In particular, mononuclear phagocyte system-related organs such as liver, spleen, and lung have phagocytic cells that uptake nanomaterials in the blood, leading to deposition of silicon in these organs[31]. Clearance of silicic acid from the body via excretion through the kidneys leads to a gradual decrease and nearly complete removal from most organs after 5 weeks. Abnormal levels of silicon in the kidney and brain at week 5, however, suggest presence of residual device silicon in the brain, as verified by computed tomography (CT) images taken for a mouse at week 5 (Fig. 2.14b). Scans of the mouse brain along the sagittal, coronal, and axial planes reveal the locations of the craniectomy defect and a sensor implanted near the top surface of the brain, fixed in a tilted angle.

Results of complete blood count and blood chemistry tests provide a comprehensive understanding of the health of the mice (Figs. 2.14c and d). Average counts of white blood cells (WBC), red blood cells (RBC), platelets (PLT) and levels of hemoglobin (HGB) and hematocrit (HCT, the percentage of red blood cells in blood) show no significant differences between implanted mice from those of control animals throughout the five-week period of the studies. Blood levels of enzymes and electrolytes, which serve as indicators of organ-specific diseases,

also fall within confidence intervals of control values. For example, normal levels of alanine aminotransferase (ALT), cholesterol (CHOL) and triglyceride (TRIG), phosphorus (PHOS) and urea nitrogen (BUN), calcium (CAL), and albumin (ALB) and total proteins (TP) indicate absence of disorders in the liver, heart, kidney, bone and nerve, and good overall health, respectively. Complete results for both tests appear in Figs. 2.15 and 2.16.

Figure 2.17 compares changes in the body weight of mice implanted with intracranial sensors to those of control animals. The differences are minimal, indicating continued maturation without significant toxic effects. Immunohistochemistry of brain, spleen, heart, and kidney tissues from a control mouse and a mouse implanted with a sensor for 5 weeks also show no obvious sign of damage, specifically with respect to steatosis, inflammation, and necrosis (Fig. 2.14e and 2.18).

Acute and chronic tracking of ICT and ICP in rats demonstrate the accuracy and long operating lifetimes of the bioresorbable sensors. Figure 4a illustrates the procedures for implantation, which involve opening a craniectomy defect, placing the sensor mounted on a thin film of poly(lactide-co-glycolide) (PLGA, ~10 μm thick; inset) inside, and applying biodegradable glue to bond the PLGA film with the surrounding skull, thereby sealing the cavity. Wired connections to an external data acquisition system allow recordings of ICP from the sensor (see Methods for details). Inserting the probe of a standard clinical ICP monitor (Integra LifeSciences, USA) through a separate defect on the same hemisphere allows comparison of the responses of bioresorbable and clinical standard devices. Storing the electrical connectors of the sensor in a plastic hat (Pinnacle Technology, USA, Fig. 2.20), fixed on the skull using dental cement (Pentron, USA), prepares the rat for subsequent tests.

Figure 2.19b shows acute recordings of the intracranial temperature (ICT) by both a bioresorbable device (red) and a commercial thermistor (blue; Digi-Key, USA) during gradual heating, using an electrical heating blanket, and cooling, using an ice pack, of the animal, indicating similar levels of accuracy. Figures 2.19c-e show recordings of acute variation in ICP induced by contracting and releasing the rat's flank (increase and decrease by ~10 mmHg, respectively; Fig. 2.19c), laying the rat in Trendelenburg (30^{o} head-down) and reverse Trendelenburg (30^{o} head-up) positions (increases and decreases by ~2 mmHg, respectively; Fig. 2.19d), and intravenously infusing Mannitol (dose: 2 g per kg weight) via the saphenous vein (decreases by 2-5 mmHg starting ~10 minutes after infusion; Fig. 2.19e) using bioresorbable (red) and commercial (blue) ICP sensors. Figure 2.19f summarizes ICP signals collected while contracting and releasing the flank on days 1, 8, 18, and 25. Responses of the sensor from days 1 through 18 display absolute accuracy within ±2 mmHg and baseline drift within ±1 mmHg. Recordings on day 25 show ~4 mmHg negative drift, in a range consistent with that of clinical ICP monitors after several days of implantation without re-calibration[29,32-34]. Signals from the device disappear after day 25, possibly due to the dissolution of the bioresorbable metal pads following penetration of water into the sensor-wire interface.

In many clinical scenarios, patients require magnetic resonance imaging (MRI) at various stages of recovery. Figure 2.21 illustrates *in vitro* verification of compatibility of a biroesorbable sensors with MRI by using gel phantoms (True Phantom Solutions, Inc., Canada) designed to imitate the conductivity and dielectric constant of the brain. The set-up consists of a bioresorbable sensor and two fiber-optic temperature probes (LumaSense Technologies, USA), one near the sensor and the other distant (control), embedded in between two 2 cm-thick slabs of the phantom. Recordings of the difference in temperatures measured by the two probes

throughout a continuous 20-minute, high-specific adsorption rate (SAR) MRI scan (3 Tesla Siemens Magnetom Prisma system) suggest that there is no significant heating associated with the presence of the device.

2.4 Conclusion

The materials, device structures, and fabrication strategies for biomedical sensors demonstrated in this study enable bioresorbable implants capable of accurate, stable monitoring of pressure and temperature in organ systems to treat chronic diseases that require extended periods of operation, previously attained only by non-resorbable devices. *In vivo* experiments to track elemental biodistribution of silicon, hematology, and blood chemistry in mice throughout five weeks following implantation of intracranial sensors confirmed their innocuity and biodegradability. *In vivo* monitoring of intracranial pressures in rats over 25 days illustrated high accuracy and low drift, which compare favorably to those of non-degradable standard devices. These results suggest not only clinical value of these bioresorbable implants, but also utility as a generalizable platform for broad classes of bioresorbable electronics, including sensors of motion, flow, and various chemical species, as well as stimulators, power supplies, or thermal actuators that may benefit from longer *in vivo* operation times.

2.5 Methods

Connections to data acquisition systems. Ultrathin enameled copper wires (~80 um diameter; Remington Industries, USA) and silver conductive epoxy (MG Chemicals, USA) formed electrical connections between the bioresorbable sensor and a digital multimeter (USB-4065; National Instruments, USA) for data acquisition during *in vitro* and *in vivo* experiments. A

100 μm-thick layer of bioresorbable polyanhydride[8] encapsulated the sensor-wire interface to prevent direct exposure to biofluid.

Calibration of the pressure response. Absolute pressure calibration of the bioresorbable sensor relied on a custom set-up consisting of an airtight container (Nuovoware, USA) connected by two plastic tubes to a commercial pressure sensor (NUL-210; Neulog, USA) and a syringe for pressure measurement and control, respectively. Placing the bioresorbable sensor inside the container, partially filled with artificial cerebrospinal fluid (ACSF, pH 7.4; Ecocyte BioSciences, USA), followed by connnecting the wires to a power supply (V_s = 2.5 V) and a digital multimeter (Fig. 2.9) prepared the system for testing. Collecting the voltage response of the bioresorbable device and pressures from the commercial device simultaneously, while varying the fluid pressure by moving the plunger of the syringe in and out, yielded a calibration curve over the range of pressures relevant to intracranial monitoring (0-70 mmHg, Fig. 2.10a).

Evaluation of the hydrolysis kinetics. Measurements by spectroscopic reflectometry (MProbe; Semiconsoft, Inc., USA) defined changes in thicknesses of films of thermal and e-beam SiO_2 (t-SiO_2 and eb-SiO_2). Profilometry (Alpha Step) revealed the thicknesses of square dots (50 um x 50 um) of amorphous silica adhesion interlayer formed on t-SiO_2 wafers (Fig. 2.11). Each sample had a lateral size of ~1 cm x 1 cm, with coatings of t-SiO_2 on the side and bottom surfaces formed by thermal oxidation. The experiments involved placing the sample in a screw cap plastic bottle filled with ~50 mL of ACSF solution, storing the bottle in an oven (Fisher Scientific, USA) to maintain the solution temperature near 37 ^oC, and monitoring the temperature throughout the experiment using a digital thermometer probe (DTP482; CDN, USA) penetrating through the plastic cap. Rinsing the sample with deionized water, drying, measuring

the thickness, and placing back in the solution (renewed every 4 days), repeatedly, yielded the dissolution rates.

Accelerated soaking tests. Soaking the device in phosphate buffered saline (PBS, pH 7.4; Sigma-Aldrich, USA) at 95^{o}C for some time, rinsing with deionized water, drying, and analyzing under an optical microscope yielded images of a bioresorbable sensor through various stages of accelerated dissolution. Similarly, evaluation of the change in the pressure sensitivity of the device throughout a process of thinning of the t-SiO_2 encapsulation layer involved soaking the device in PBS at 95^{o}C for 30 minutes, rinsing with deionized water, drying, calibrating against the commercial pressure sensor, and placing back in the PBS. The dissolution chamber comprised of a screw cap plastic bottle, installed with a penetrating thermometer probe and kept in a heated oven.

Evaluation of the biodistribution, hematology, and blood chemistry of mice. Overnight ultraviolet radiation sterilized miniaturized bioresorbable sensors (size: 750 μm x 750 μm x 11 μm; weight ~12 μg) without t-SiO_2 encapsulation prior to device implantation. The procedures involved anaesthetizing a female CD-1 mouse (Charles River, USA) with isoflurane gas, fixing the head in a stereotaxic frame, forming a craniectomy defect using a drill, implanting the sensor into the intracranial cavity, sealing the defect with a drop of biodegradable tissue adhesive (TissueSeal, USA), and suturing the scalp. Daily monitoring and weighing of the mice ensured their normal stress and moribund conditions. Computed tomography scans carried out every week tracked the size and location of the implanted device. Euthanization of 1-2 mice at weeks 1, 3, and 5 after device implantation enabled extraction of blood and explantation of organs including liver, spleen, heart, kidney, brain, and lung. Charles River Laboratory (Boston, MA) conducted complete blood count and blood chemistry tests on the blood samples collected in K-

EDTA tubes and gel tubes, respectively. Weighing, splitting the explanted organs in half, and storing the halves in pre-weighed 15 mL conical metal-free tubes in -20 ^{o}C fridge and in 10 % buffered formalin in 50 mL conical tubes prepared tissue samples for biodistribution and histology studies, respectively. Dissolving the tissues by adding 1.5 mL nitric acid and 0.35 mL hydrogen peroxide to each tube, keeping the tubes in 65^{o}C water bath for 5 hours, diluting the dissolved tissue solutions 1:20 by adding Milli-Q water (MilliporeSigma, USA), and analyzing by inductively coupled plasma optical emission spectrometry (ICP-OES) yielded the concentrations of Si in the tissues 1, 3, and 5 weeks after implantation to demonstrate biodistribution and biodegradability of dissolved silicon.

Evaluation in animal models. All procedures of the animal study followed the recommendations in the Guide for the Care and Use of Laboratory Animals of the National Institutes of Health. The Institutional Animal Care and Use Committee (IACUC) of Washington University in St Louis (protocol number 20170189) approved the protocol. Male Lewis rats weighing 250–350 g (Charles River, Wilmington, MA) received subcutaneous injections of buprenorphine hydrochloride (0.05 mg kg^{-1}; Reckitt Benckiser Healthcare Ltd, USA) for pain management, and of ampicillin (50 mg kg^{-1}; Sage Pharmaceuticals, USA) to prevent infection at the implantation site before the surgical process. The surgical procedures involved anaesthetizing the rat with isoflurane gas, holding the head in a stereotaxic frame, opening a craniectomy and dura, implanting the bioresorbable sensor on the cortical surface, and sealing the craniectomy with a PLGA sheet (~10 μm thick) and biodegradable glue (TissueSeal, USA). A clinical intracranial pressure monitor (Integra LifeSciences, USA) or a commercial thermistor (Digi-Key, USA) implanted in a nearby craniectomy enabled comparison testing to demonstrate the accuracy of the pressure and temperature measurements by the bioresorbable sensor, respectively.

Biodegradable glue sealed the opening for commercial sensor after testing. A plastic chamber with cap (Pinnacle Technology, USA), fixed on the skull by dental cement (Fusio™ Liquid Dentin; Pentron, USA), stored and protected the implanted bioresorbable sensor and its electrical connectors for subsequent tests.

Evaluation of the MRI compatibility. The set-up consisted of a bioresorbable sensor and two fiber optic temperature probes (Luxtron 812 Fluoroptic Thermometer; LumaSense Technologies, USA), one placed near the sensor and the other distant, sandwiched between brain phantom slabs (True Phantom Solutions, Inc., Canada). A 3 Tesla Siemens Magnetom Prisma MRI scanner performed a high-SAR (Specific Adsorption Rate, or RF deposition) turbo spin echo (TSE) scan (repetition time (TR) = 6290.0 ms, echo time (TE) = 99 ms, 14 slices, thickness= 4 mm, flip angle = 180º, field of view = 230 × 230 mm) continuously for 20 minutes.

Calculation of the Gauge Factor. The gauge factor (G) of the silicon nanomembrane strain gauge (Si NM SG) can be estimated by the following equation[35]:

$$\mathrm{G} = \frac{\Delta R}{R_0 \times \varepsilon}$$

where ΔR is the change in resistance of the SG due to piezoresistivity of silicon at elevated pressures, R_0 is the resistance of the SG at atmospheric pressure, and ε is the average strain in the SG.

Three-dimensional finite element analysis (3D-FEA) using commercial software (ABAQUS) can reveal the average strain within the SG under pressure load ranging from 0 to 40 mmHg (Fig. 2.4a) based on quadrilateral shell element S4R for the diaphragm and clamped edge boundary conditions[8]. The resistance change ΔR with respect to applied pressure can be obtained experimentally. The base resistance R_0 of the SG lying on the diaphragm is estimated by FEA to be ~38.9 % of the resistance measured across the metal contact pads based on SG design,

assuming uniform doping concentration in the silicon nanomembrane. The slope of a plot of $\Delta R/R_0$ versus ε yields a gauge factor of –20.9 (Fig. 2.4b).

The gauge factor can also be calculated analytically by the following equation[36]:

$$G = \alpha\pi_{Si[110]}E_{Si} = 0.5 \times \left(-31 \times 10^{-11}\,\frac{1}{Pa}\right) \times (130 \times 10^{9}\ \mathrm{Pa}) = -20.15$$

where α is a correction coefficient for different doping concentrations[37], π is the piezoresistive coefficient for n-type monocrystalline silicon, and *E* represents Young's modulus. The calculated gauge factor agrees well with the experimental/modeling result.

2.6 Figures

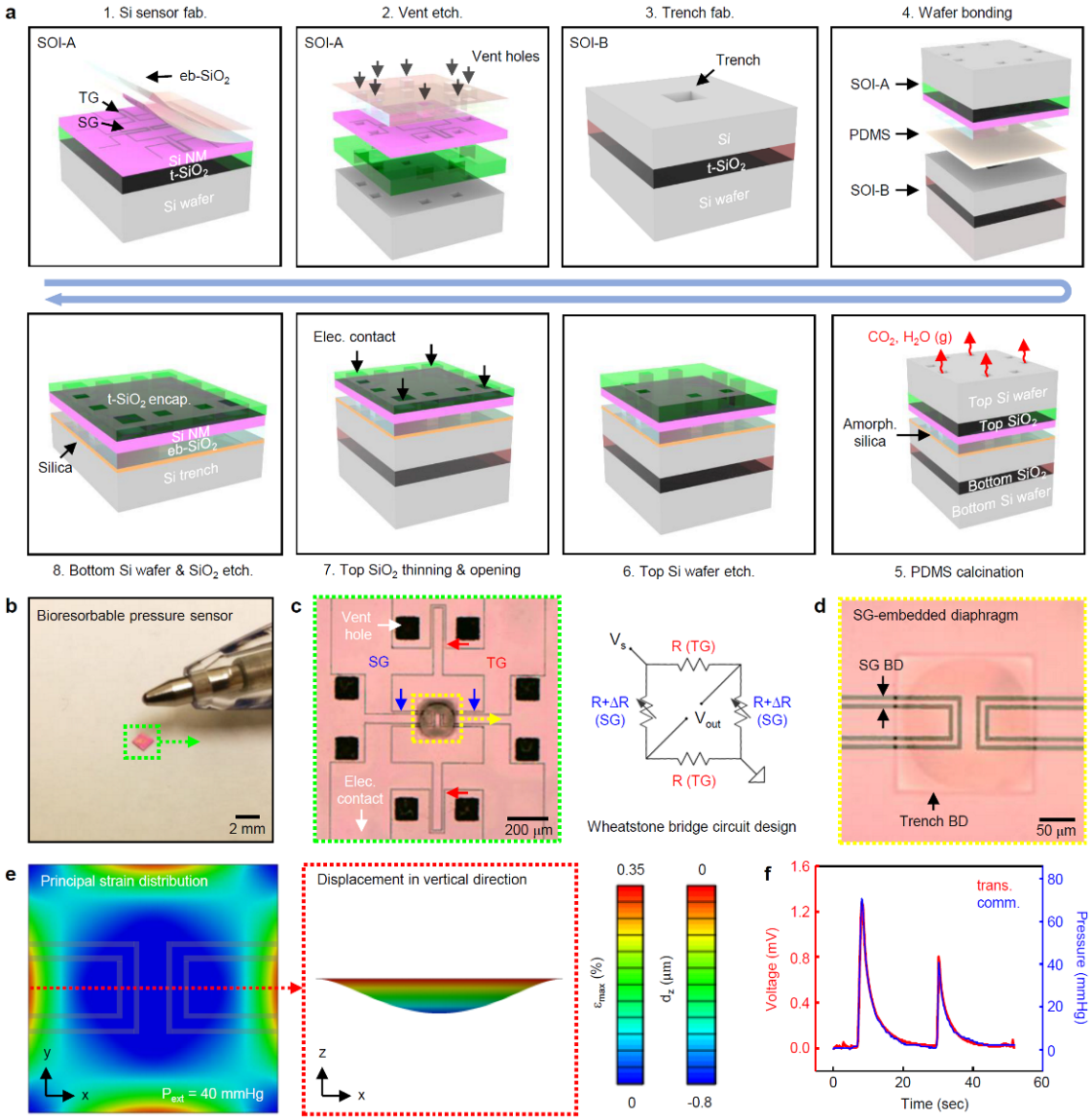

Figure 2.1 Procedures for fabricating inorganic bioresorbable pressure sensors. a, Steps for fabricating piezoresistive sensors based on silicon nanomembranes (Si NMs, pink) on a silicon-on-insulator (SOI) wafer, SOI-A (1). Reactive ion etching to form an array of vent holes through the wafer (2). Reactive ion etching to form a trench (top white) on a separate SOI wafer, SOI-B (3). Aligned bonding of SOI-A and SOI-B using a thin film of PDMS (beige) as an adhesion interlayer (4). Calcination of the PDMS to yield amorphous silica (orange) by heating in a furnace (5). Release of gaseous products (CO_2 and H_2O) through vent holes in SOI-A. Reactive ion etching to eliminate the silicon wafer of SOI-A (6). Wet etching of the buried oxide using buffered oxide etchant (BOE) to yield a layer of SiO_2 (green) with desired thickness and to expose regions for electrical contacts (7). Reactive ion etching to eliminate the silicon wafer and

Fig. 2.1 (cont.) the buried oxide of SOI-B (8). B, Photograph of a bioresorbable pressure sensor next to the tip of a ball point pen. c, Optical micrograph of the sensor (left). Two Si NM structures that extend partially over the trench on a flexible diaphragm define strain gauges (SGs, blue) with piezoresistive responses. A pair of Si NM sensors on regions adjacent to the trench define temperature gauges (TGs, red) via their temperature-dependent resistance. Four gauges combine to form a Wheatstone bridge circuit (right) that compensates temperature induced variations in the piezoresistivity of the SGs. d, Optical micrograph of SGs embedded in a diaphragm. Two boundary lines (grey area, no silicon) isolate the SGs (pink area, silicon) from the surrounding Si NM. Thermal SiO_2 (t-SiO_2), Si NM, and SiO_2 deposited by electron beam evaporation (eb-SiO_2) define the flexible diaphragm that spans over the square trench. e, Three-dimensional finite element analysis (3D-FEA) results for the distribution of principal strains (left) and vertical displacements (right) of the diaphragm for an external pressure of 40 mmHg above atmospheric. f, Responses of a bioresorbable pressure sensor (red, V_s = 2.5V) and a commercial sensor (blue) to time-varying pressures over a range relevant to variations in intracranial pressure (ICP).

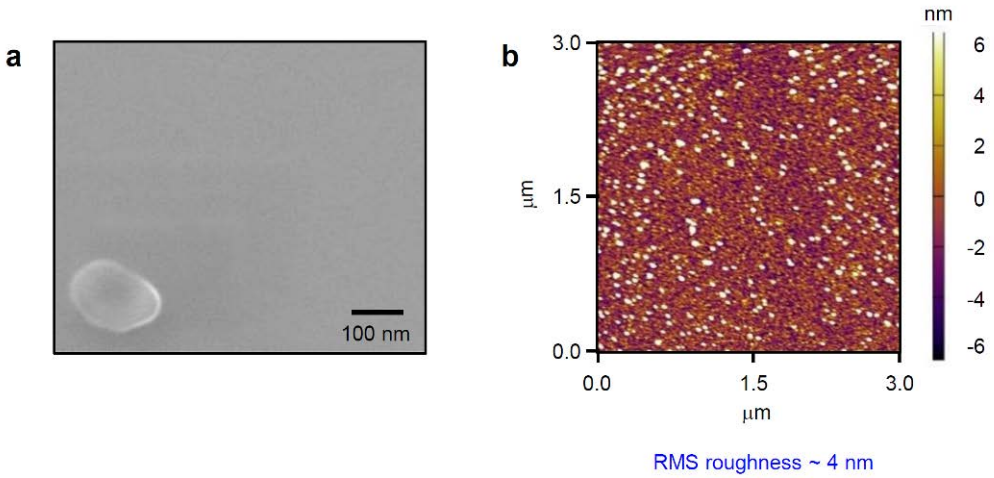

Figure 2.2 a, Scanning electron microscope and b, atomic force microscope images of the surface of an amorphous silica layer obtained from PDMS calcination.

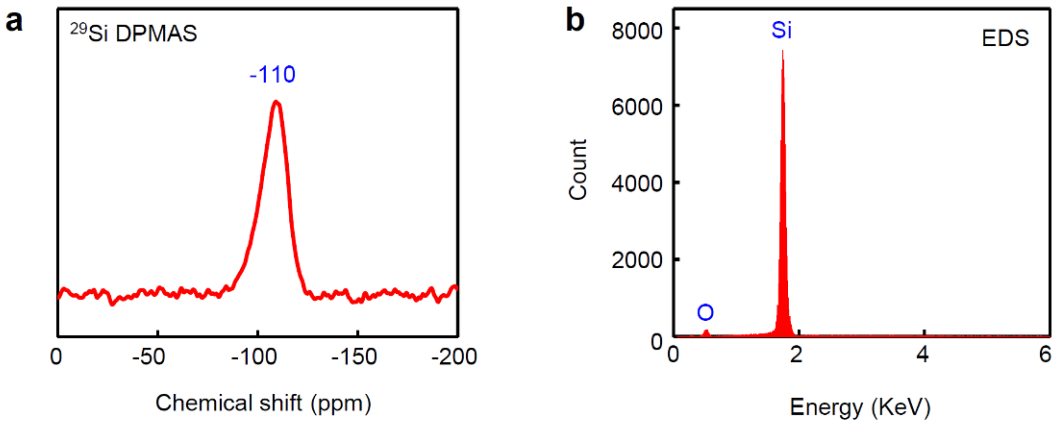

Figure 2.3 a, Silicon NMR spectroscopy (^{29}Si DPMAS) and b, electron dispersive spectroscopy (EDS) measurements of amorphous silica powder obtained from PDMS calcination followed by annealing at 800^{o}C.

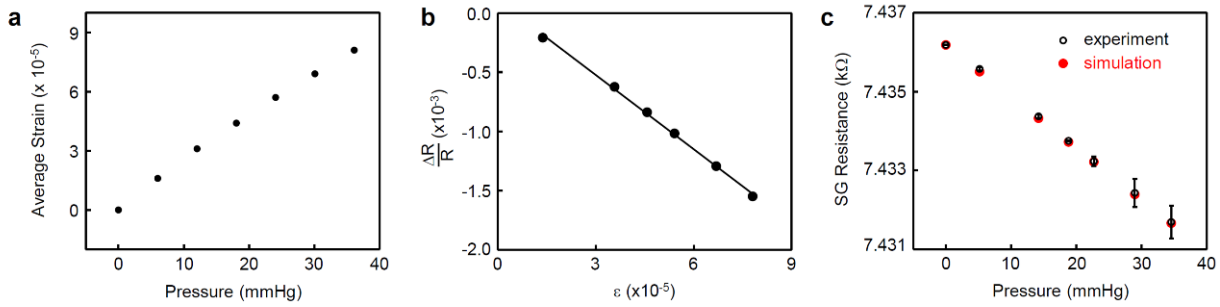

Figure 2.4 a, Three-dimensional finite element analysis (3D-FEA) of the average strain within a strain gauge (SG) due to applied pressure. b, Resistance responses of the SG with simulated average strain. The gauge factor (slope) is -20.9. c, Calibration of the resistance of a bioresorbable SG to pressure (black) compared with responses simulated by FEA (red).

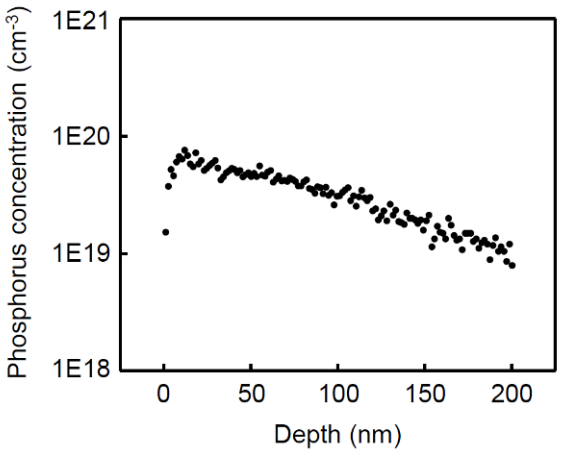

Figure 2.5 Secondary ion mass spectrometry (SIMS) profile of phosphorus distributed throughout the thickness of a silicon nanomembrane (Si NM).

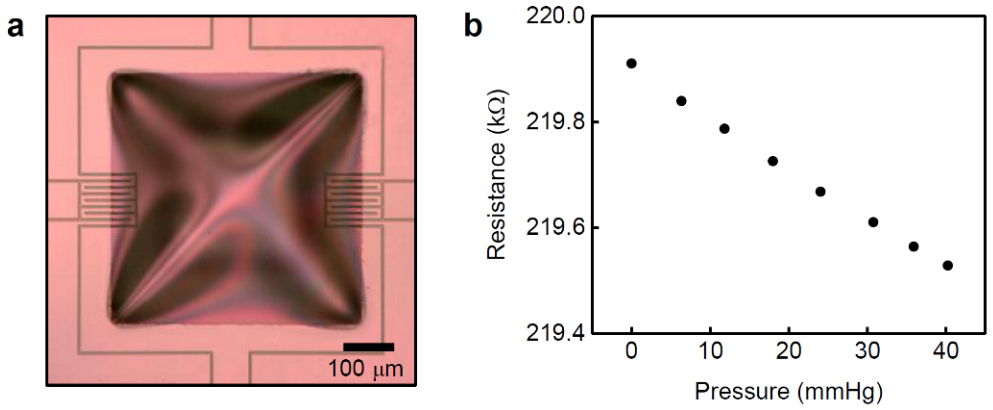

Figure 2.6 a, Optical micrograph and b, calibration curve of a bioresorbable sensor with a thin Si NM (~50 nm), large diaphragm area (500 μm x 500 μm), and serpentine strain gauge. The sensor shows a significantly higher pressure sensitivity of -9.47 Ω/mmHg.

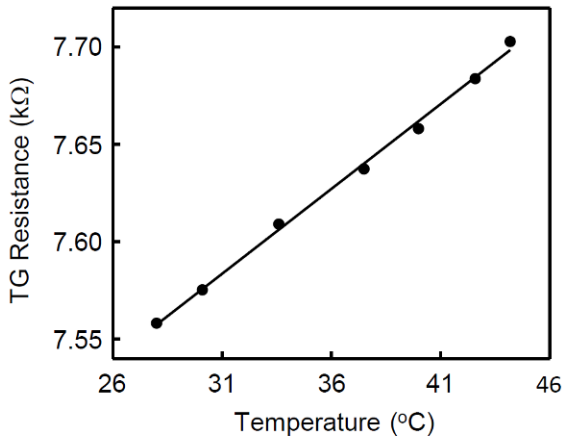

Figure 2.7 Calibration of the resistance of a bioresorbable temperature gauge (TG). The temperature coefficient of resistance (TCR) is ~0.0012/°C.

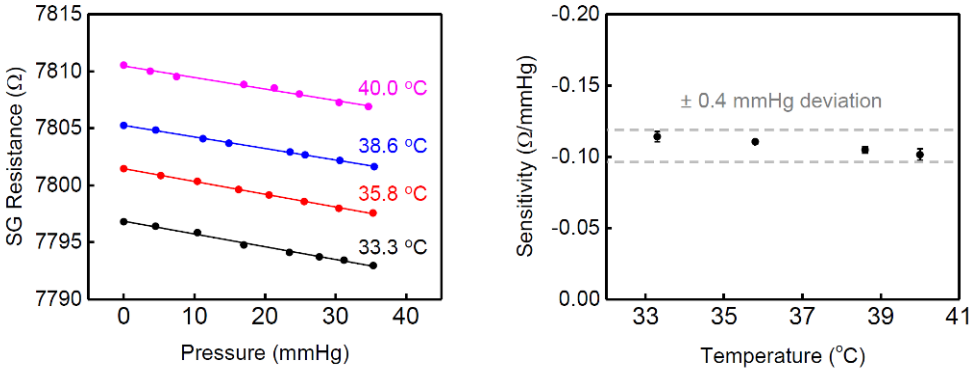

Figure 2.8 Pressure sensitivity of a bioresorbable sensor measured at different temperatures within a range relevant for intracranial temperature (33-40 ^{o}C). Maximum deviation in measured pressures at these temperatures is less than ±0.4 mmHg.

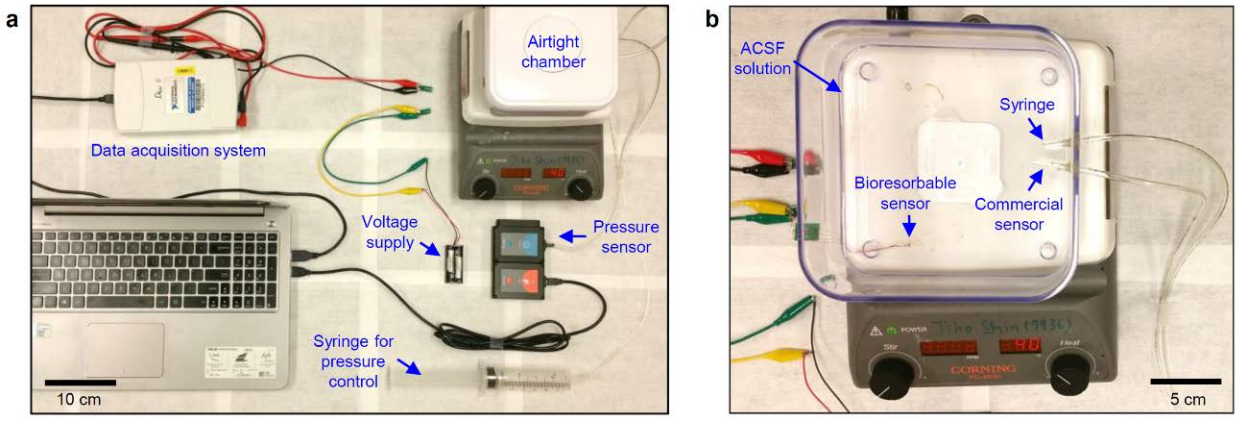

Figure 2.9 a, Photograph of the test set-up for *in vitro* assessment of bioresorbable intracranial sensors. b, Airtight chamber without the top cover.

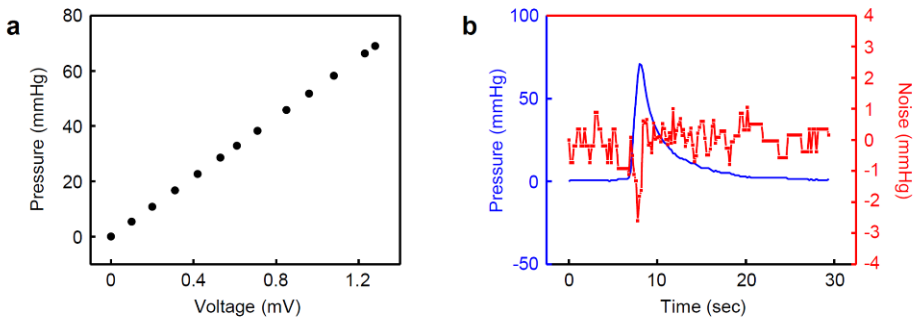

Figure 2.10 a, Calibration of the voltage responses of a bioresorbable sensor with pressures measured by commercial sensor. b, Noise floor in the response of the bioresorbable sensor (red), evaluated as the difference between pressures measured by the bioresorbable and commercial devices exposed to time-varying pressure. Pressures recorded by the commercial sensor (blue), which has a noise floor less than ±0.8 mmHg.

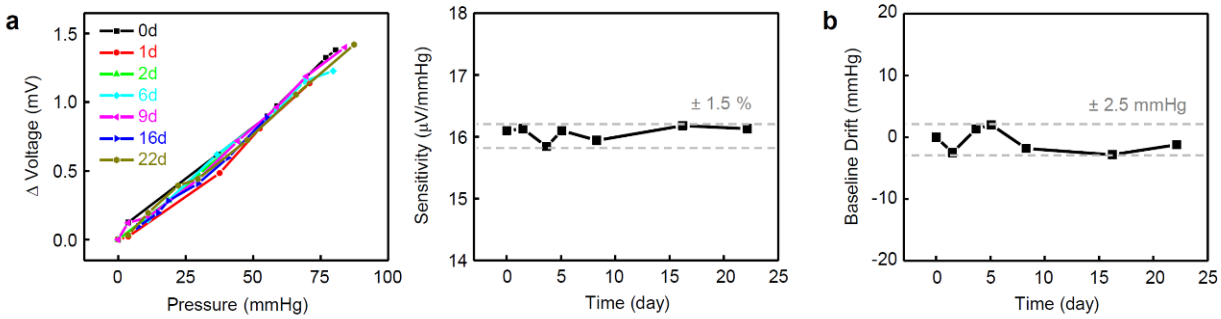

Figure 2.11 a, Calibration curves for a bioresorbable pressure sensor obtained throughout a 22-day period of *in vitro* operation in ACSF at T = 37ºC (left). Pressure sensitivity as a function of time (right). b, Drift in the baseline as a function of time.

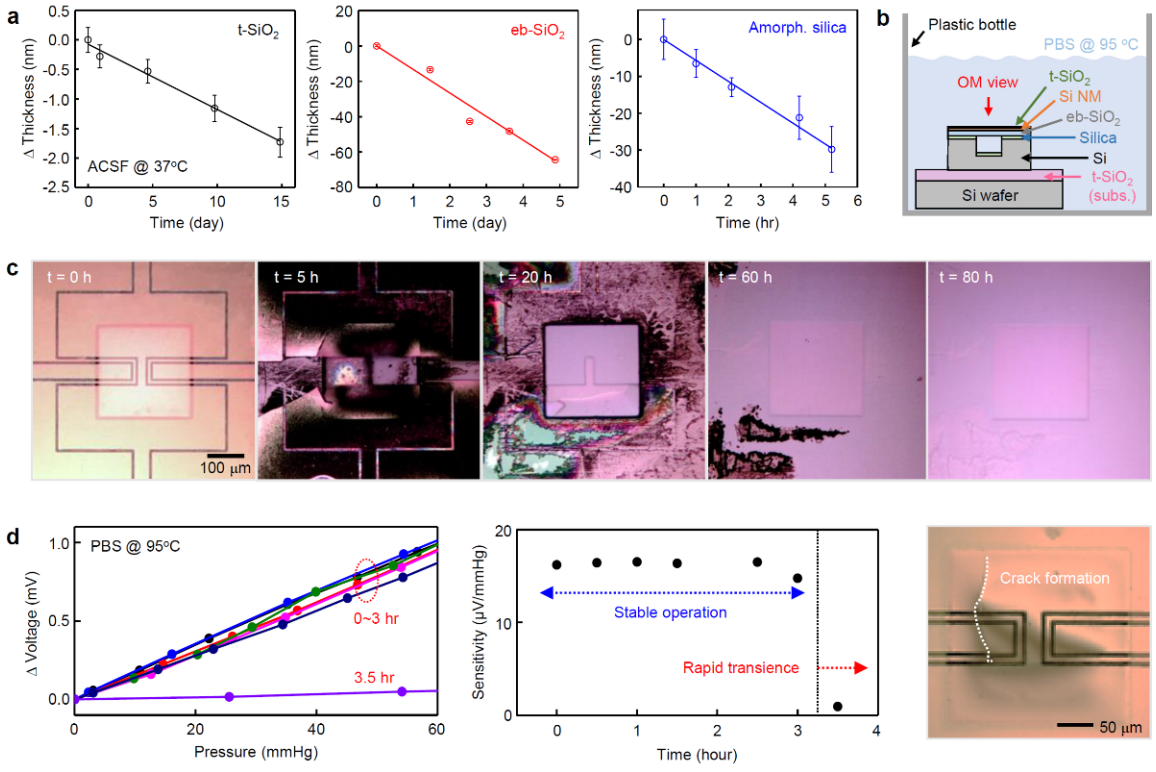

Figure 2.12 Kinetics of dissolution of a bioresorbable pressure sensor. a, Measured changes in thickness as a function of time of immersion of t-SiO_2 (left), eb-SiO_2 (middle), and amorphous silica (obtained from calcination of PDMS, right) in artificial cerebrospinal fluid (ACSF, pH 7.4) at 37°C. The dissolution rates are 0.11 ± 0.01, 13.6 ± 1.6, and 129 ± 9 nm/day, respectively. b, Schematic illustration of the *in vitro* dissolution experiment set-up. c, Optical micrographs at various stages of accelerated dissolution of a bioresorbable pressure sensor due to immersion in phosphate buffered saline (PBS, pH 7.4) at 95°C. d, Voltage response of a sensor with t-SiO_2 encapsulation (~10 nm) and comparison to a commercial device at various times after immersion in PBS at 95°C (left), with corresponding responsitivities as a function of time (middle). The data indicate two-stage kinetics in function, involving stable operation for several hours, defined by dissolution of thermal SiO_2 encapsulation layer, followed by rapid degradation due to formation of hole/crack in the diaphragm (right) due to dissolution of the functional layers.

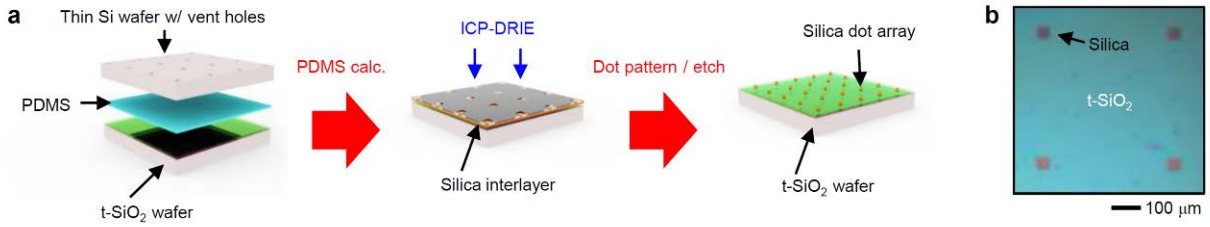

Figure 2.13 a, Fabrication steps and b, optical micrograph of an array of square patterns of silica (50 μm x 50 μm) on a silicon wafer used for study of dissolution kinetics of silica.

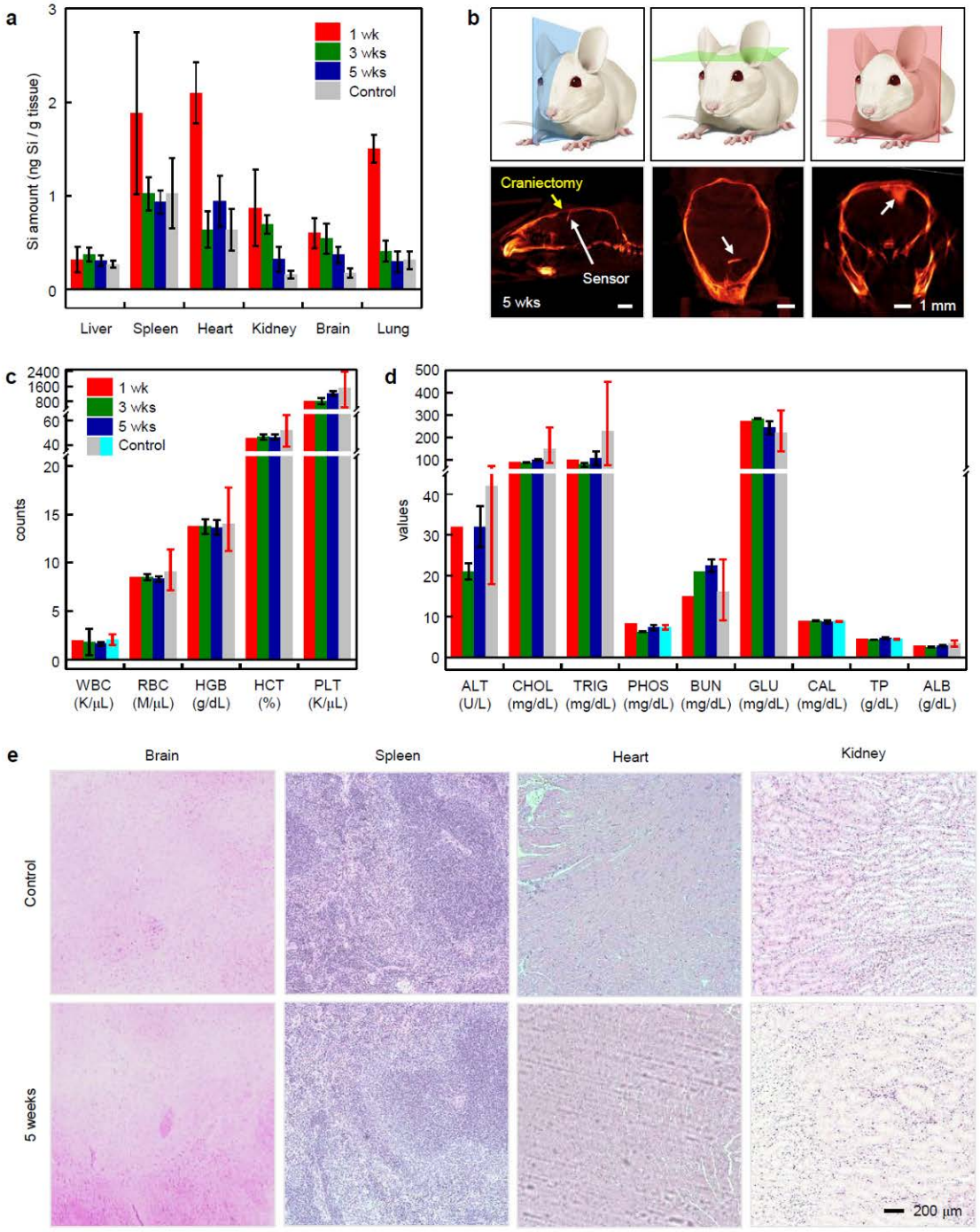

Figure 2.14 *In vivo* measurements of elemental biodistribution and biocompatibility of bioresorbable devices throughout their functional lifetimes and beyond. a) *In vivo* biodistribution of products of dissolution of bioresorbable pressure sensors (size: 750 μm x 750 μm x 10 μm; weight ~12 μg; no t-SiO_2 encapsulation) implanted within the intracranial space of mice (n = 1 or 2), with comparisons to control animals (n = 2). A drop of biodegradable tissue adhesive

Fig. 2.14 (cont.) (TissueSeal, USA) seals the craniectomy defect after implantation. Inductively coupled plasma optical emission spectrometry (ICP-OES) determines concentrations of silicon in organs explanted at 1, 3, and 5 weeks post implantation. High concentrations of silicon in spleen, heart, and lung tissues in the first week after implantation decrease gradually to normal levels. b) Computed tomography (CT) scans of a mouse brain after 5 weeks. Cartoon illustrations and CT images 5 weeks post implant of the sagittal (left), coronal (middle), and axial (right) planes show the locations of the craniectomy and a sensor near the surface of the brain fixed at a tilted angle. c, d) Results of c) complete blood count test and d) blood chemistry test for the mice in a. No significant differences from control animals can be found for both tests. Control data provided by the mouse supplier (Charles River, gray) or collected from 22-24 mice acquired from two batches within 2 months' span (cyan). Red error bars indicate 95% confidence intervals; black error bars indicate S.E. Abbreviations include, WBC: white blood cell, RBC: red blood cell, HGB: blood hemoglobin level, HCT: hematocrit level, PLT: platelet count in blood, ALT: alanine aminotransferase, CHOL: cholesterol, TRIG: triglycerides, PHOS: phosphorus, BUN: urea nitrogen, GLU: glucose, CAL: calcium, TP: total protein, ALB: albumin. e) Immunohistochemistry of brain, spleen, heart, and kidney tissues of a control mouse and a mouse implanted with a bioresorbable sensor 5 weeks post implantation, showing no notable sign of damage.

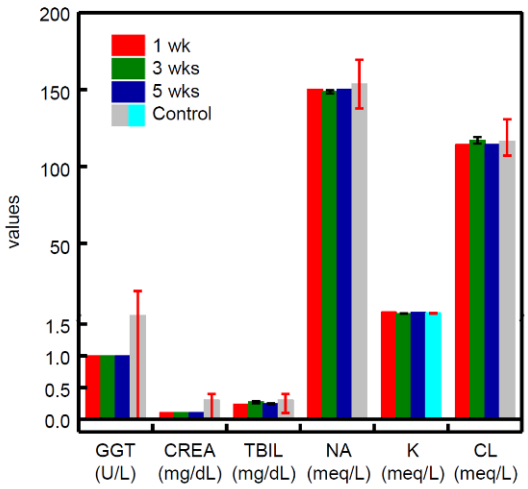

Figure 2.15 Results for complete blood count (CBC) tests of mice implanted with bioresorbable intracranial pressure sensors. Abbreviations include, NE: neutrophil, LY: lymphocyte, MO: monocyte, EO: eosinophil, BA: basophil, MCV: mean corpuscular volume, MCH: mean corpuscular hemoglobin, MCHC: mean corpuscular hemoglobin concentration, RDW: red cell distribution width, MPV: mean platelet volume. # and % indicate number and percent, respectively.

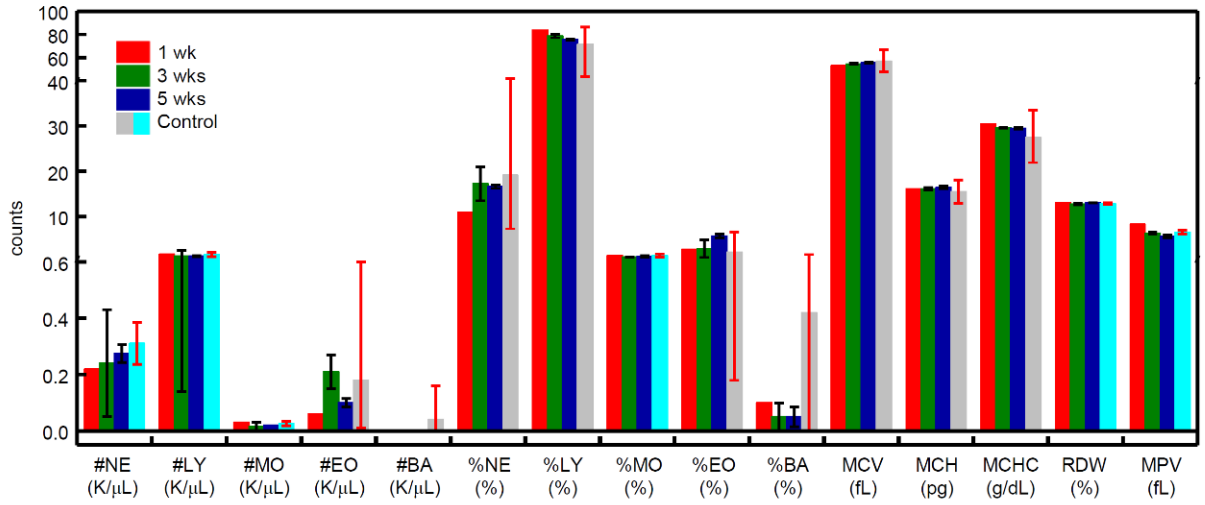

Figure 2.16 Results from blood chemistry tests of mice implanted with bioresorbable intracranial pressure sensors. Abbreviations include, GGT: gamma-glutamyl transferase, CREA: creatinine, TBIL: total bilirubin, NA: sodium, K: potassium, CL: chloride.

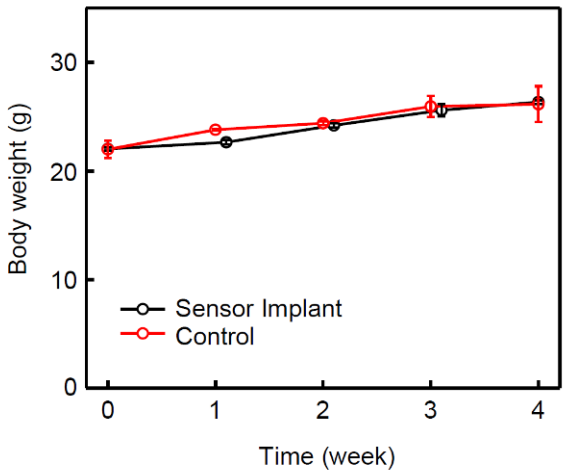

Figure 2.17 Changes in body weights of mice implanted with bioresorbable pressure sensors (n = 3) compared with control animals (n = 3).

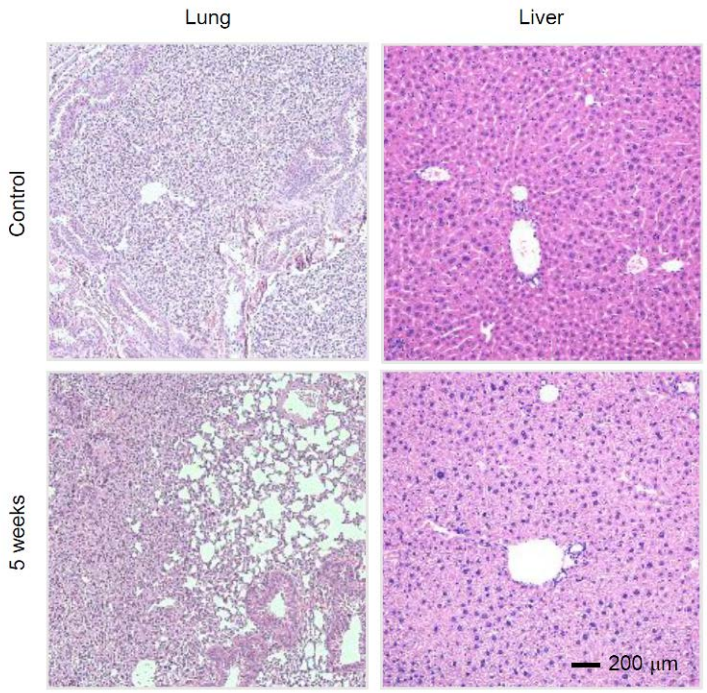

Figure 2.18 Immunohistochemistry of lung and liver tissues of a control mouse and a mouse with a bioresorbable implant 5 weeks after implantation.

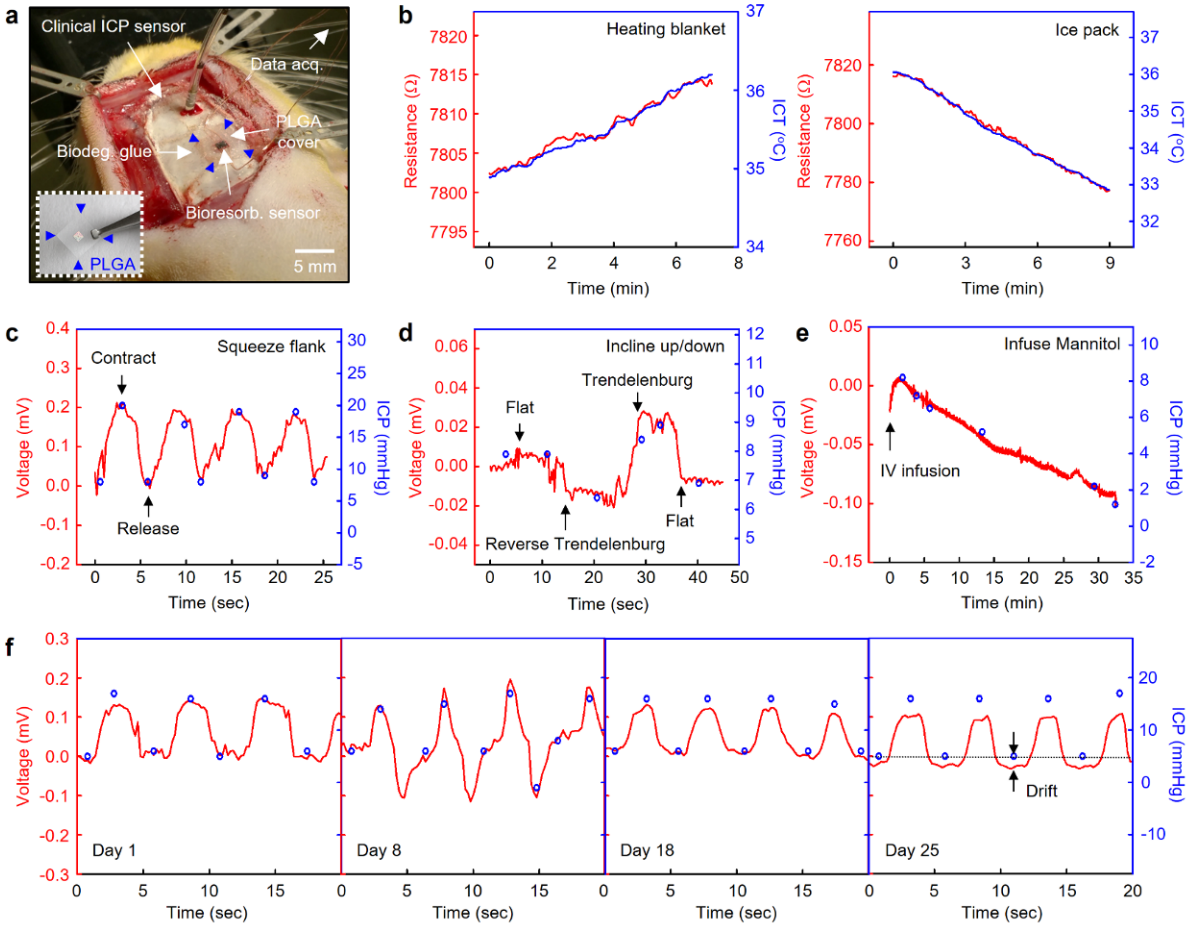

Figure 2.19 Acute and chronic monitoring of intracranial temperature and pressure in rats using bioresorbable sensors. a, Photograph of a bioresorbable ICP sensor implanted in a rat. Image of a sensor mounted on a thin film of poly(lactide-co-glycolide) (PLGA, ~10 um thick; inset), placed in an intracranial cavity on the right hemisphere after exposure by craniectomy. Biodegradable glue bonds the edges of the film to the surrounding skull and seals the cavity. Wired connection to a digital multimeter allows data acquisition from the sensor. A clinical ICP monitor probe inserted in the same hemisphere of the brain serves as reference. b, *In vivo* recordings of intracranial temperature (ICT) of a rat as a function of time. Both bioresorbable (red) and commercial (blue) devices capture gradual increase (left) and decrease (right) in ICT caused by application of heating blanket/ice pack. c, d, e, *In vivo* monitoring of variations in ICP due to c, contracting and releasing rat's flank, d, laying in Trendelenburg (30^{o} head-down; increases ICP) and reverse Trendelenburg (30^{o} head-up; decreases ICP) positions, e, and infusing Mannitol, which decreases ICP, in the saphenous vein, as a function of time by both bioresorbable (red) and commercial (blue) sensors. f, *In vivo* recordings of ICP as a function of time on days 1, 8, 18, and 25 post implantation. About 10 mmHg variations in ICP are induced by contracting and releasing the intraperitoneal (body) cavity. Recordings on day 25 show ~3 mmHg negative drift for the bioresorbable device.

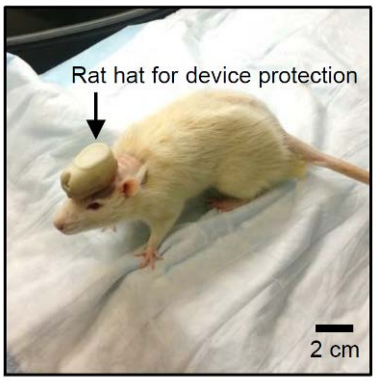

Figure 2.20 Photograph of a rat mounted with a plastic hat for protection of the implanted sensor and its electrical connectors.

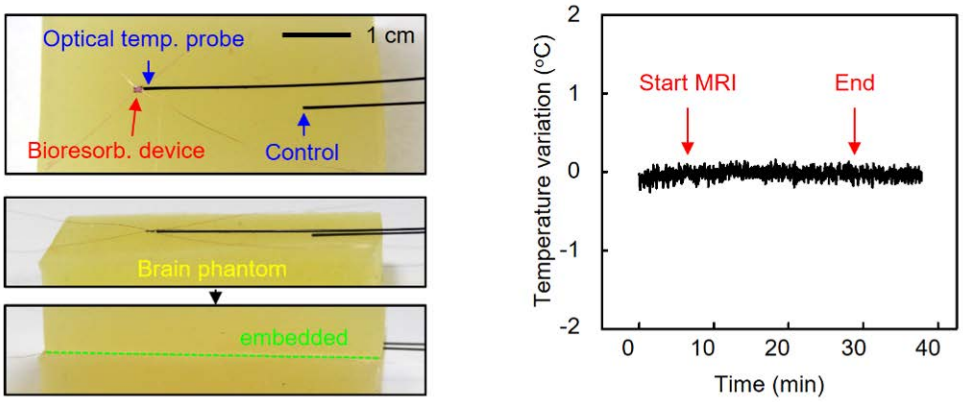

Figure 2.21 Magnetic resonance imaging (MRI) compatibility of a bioresorbable sensor placed in a brain phantom, designed to imitate the conductivity and dielectric constant of brain tissue. Photograph of a bioresorbable sensor and two fiber-optic temperature probes (one near and the other distant from the sensor) placed in between two slabs of the phantom (left). Recordings of the difference in temperatures measured by the two probes throughout a 20-minute, high-specific adsorption rate (SAR) scan, indicating no significant heating of the device.

2.7 References

1 Jiang, G. Design challenges of implantable pressure monitoring system. *Frontiers in Neuroscience* **4** (2010).

2 Yu, L., Kim, B. & Meng, E. Chronically Implanted Pressure Sensors: Challenges and State of the Field. *Sensors* **14**, 20620 (2014).

3 Sit, A. J. Continuous Monitoring of Intraocular Pressure: Rationale and Progress Toward A Clinical Device. *Journal of Glaucoma* **18**, 272-279 (2009).

4 Boutry, C. M. *et al.* Towards biodegradable wireless implants. *Philosophical Transactions of the Royal Society A: Mathematical, Physical and Engineering Sciences* **370**, 2418-2432 (2012).

5 Chamis, A. L. *et al.* Staphylococcus aureus Bacteremia in Patients With Permanent Pacemakers or Implantable Cardioverter-Defibrillators. *Circulation* **104**, 1029-1033, (2001).

6 Hall-Stoodley, L., Costerton, J. W. & Stoodley, P. Bacterial biofilms: from the Natural environment to infectious diseases. *Nature Reviews Microbiology* **2**, 95, (2004).

7 Polikov, V. S., Tresco, P. A. & Reichert, W. M. Response of brain tissue to chronically implanted neural electrodes. *Journal of Neuroscience Methods* **148**, 1-18 (2005).

8 Kang, S.-K. *et al.* Bioresorbable silicon electronic sensors for the brain. *Nature* **530**, 71 (2016).

9 Luo, M., Martinez, A. W., Song, C., Herrault, F. & Allen, M. G. A Microfabricated Wireless RF Pressure Sensor Made Completely of Biodegradable Materials. *Journal of Microelectromechanical Systems* **23**, 4-13 (2014).

10 Hwang, S.-W. *et al.* Biodegradable Elastomers and Silicon Nanomembranes/Nanoribbons for Stretchable, Transient Electronics, and Biosensors. *Nano Letters* **15**, 2801-2808 (2015).

11 Yu, K. J. *et al.* Bioresorbable silicon electronics for transient spatiotemporal mapping of electrical activity from the cerebral cortex. *Nature Materials* **15**, 782 (2016).

12 Lee, Y. K. *et al.* Dissolution of Monocrystalline Silicon Nanomembranes and Their Use as Encapsulation Layers and Electrical Interfaces in Water-Soluble Electronics. *ACS Nano* **11**, 12562-12572 (2017).

13 Lee, G. *et al.* Fully Biodegradable Microsupercapacitor for Power Storage in Transient Electronics. *Advanced Energy Materials* **7** (2017).

14 Lee, C. H. *et al.* Wireless Microfluidic Systems for Programmed, Functional Transformation of Transient Electronic Devices. *Advanced Functional Materials* **25**, 5100-5106 (2015).

15 Tao, H. *et al.* Silk-based resorbable electronic devices for remotely controlled therapy and in vivo infection abatement. *Proceedings of the National Academy of Sciences* **111**, 17385-17389 (2014).

16 Hwang, S.-W. *et al.* A Physically Transient Form of Silicon Electronics. *Science* **337**, 1640-1644 (2012).

17 Hwang, S.-W. *et al.* High-Performance Biodegradable/Transient Electronics on Biodegradable Polymers. *Advanced Materials* **26**, 3905-3911 (2014).

18 Kang, S.-K. *et al.* Dissolution Behaviors and Applications of Silicon Oxides and Nitrides in Transient Electronics. *Advanced Functional Materials* **24**, 4427-4434 (2014).

19 Kang, S.-K. *et al.* Biodegradable Thin Metal Foils and Spin-On Glass Materials for Transient Electronics. *Advanced Functional Materials* **25**, 1789-1797 (2015).

20 Fang, H. *et al.* Ultrathin, transferred layers of thermally grown silicon dioxide as biofluid barriers for biointegrated flexible electronic systems. *Proceedings of the National Academy of Sciences* **113**, 11682-11687 (2016).

21 Lee, Y. K. *et al.* Kinetics and Chemistry of Hydrolysis of Ultrathin, Thermally Grown Layers of Silicon Oxide as Biofluid Barriers in Flexible Electronic Systems. *ACS Applied Materials & Interfaces* **9**, 42633-42638 (2017).

22 Haddad, S. H. & Arabi, Y. M. Critical care management of severe traumatic brain injury in adults. *Scandinavian Journal of Trauma, Resuscitation and Emergency Medicine* **20**, 12 (2012).

23 Camino, G., Lomakin, S. M. & Lazzari, M. Polydimethylsiloxane thermal degradation Part 1. Kinetic aspects. *Polymer* **42**, 2395-2402 (2001).

24 Wang, Q., Ding, J. & Wang, W. Fabrication and temperature coefficient compensation technology of low cost high temperature pressure sensor. *Sensors and Actuators A: Physical* **120**, 468-473 (2005).

25 Kanda, Y. A graphical representation of the piezoresistance coefficients in silicon. *IEEE Transactions on Electron Devices* **29**, 64-70 (1982).

26 Lund, E. & Finstad, T. G. Temperature and Doping Dependency of Piezoresistivity in p-type Silicon. *MRS Proceedings* **657** (2000).

27 Norton, P. & Brandt, J. Temperature coefficient of resistance for p- and n-type silicon. *Solid-State Electronics* **21**, 969-974 (1978).

28 Brain Trauma, F. *et al.* Guidelines for the management of severe traumatic brain injury. VI. Indications for intracranial pressure monitoring. *J Neurotrauma* **24 Suppl 1**, S37-44 (2007).

29 Post craniotomy subdural pressure monitoring kit. Model 110-4G, in *San Diego, CA: Integra NeuroSciences* (2010).

30 Johanson, C. E. *et al.* Multiplicity of cerebrospinal fluid functions: New challenges in health and disease. *Cerebrospinal Fluid Research* **5**, 10 (2008).

31 Moghimi, S. M. & Patel, H. M. Serum-mediated recognition of liposomes by phagocytic cells of the reticuloendothelial system – The concept of tissue specificity. *Advanced Drug Delivery Reviews* **32**, 45-60 (1998).

32 Gelabert-González, M. *et al.* The Camino intracranial pressure device in clinical practice. Assessment in a 1000 cases. *Acta Neurochirurgica* **148**, 435-441 (2006).

33 Martínez-Mañas, R. M., Santamarta, D., de Campos, J. M. & Ferrer, E. Camino® intracranial pressure monitor: prospective study of accuracy and complications. *Journal of Neurology, Neurosurgery & Psychiatry* **69**, 82 (2000).

34 Zacchetti, L., Magnoni, S., Di Corte, F., Zanier, E. R. & Stocchetti, N. Accuracy of intracranial pressure monitoring: systematic review and meta-analysis. *Critical Care* **19**, 420 (2015).

35 Maluf, N. & Williams, K. *Introduction to Microelectromechanical Systems Engineering*. (Artech House, 2004).

36 Liu, C. *Foundations of MEMS*. 214-215 (Prentice-Hall, 2006).

37 Lund, E. & Finstad, T. G. Temperature and Doping Dependency of Piezoresistivity in p-type Silicon. *MRS Proceedings* **657**, EE5.13 (2000).

CHAPTER 3: BIORESORBABLE OPTICAL SENSORS AND WAVEGUIDES

3.1 Introduction

Bioresorbable sensors, an emerging class of technology in which the constituent materials disappear completely in a controlled fashion within the body, provide basis for novel implantable devices that can avoid patient distress and complications associated with surgical removal procedures, as well as infection via biofilm colonization along percutaneous wires, problems that are commonly associated with standard permanent electronic hardware[3,4,6-8,10]. Optical sensors, based on changes in intensity or resonance frequency of guided light rather than electrical parameters like voltage or current, offer several important advantages over electronic analogs, such as compatibility with magnetic resonance imaging (MRI), which is frequently used in patients that undergo surgery and are primary targets for sensor implants, but could cause heating or displacement of electronic implants[24]; they also offer safety from potential tissue damage due to normal or leakage current flows[25].

Here, we demonstrate materials, design, and fabrication strategies for bioresorbable optical pressure and temperature sensors. Two types of optical pressure sensors based on Fabry-Perot interferometry and photonic crystal microcavities both demonstrate good pressure sensitivity with linear responses to pressure variation, verified by simulation as well as *in vitro* and *in vivo* experiments. Accelerated dissolution tests in hot phosphate buffered saline solutions show complete disintegration of the constituent materials.

3.2 Experiments

Schematic illustration of the fabrication procedures for bioresorbable Fabry-Perot (FP) pressure sensors appear in Fig. 3.1. The process began with solid-state diffusion of phosphorous at 950^{o}C on a mechanically back-grinded silicon-on-insulator (SOI-A) wafer (top Si ~250 nm, buried SiO_2 ~1 μm, Si wafer ~100 μm; SOITEC, France) to reach doping concentration of ~10^{20} cm^{-3}. Fabrication of silicon trench involved patterning and deep reactive ion etching (ICP-DRIE) of an array of square patterns (area: 250 μm x 250 μm) on a separate SOI wafer (SOI-B, top Si ~15 μm, buried SiO_2 ~600 nm, Si wafer ~85 μm; University Wafer, USA). Removing the Si wafer of SOI-B by ICP-DRIE, wet etching in a buffered oxide etchant (BOE, 6:1; Transene Company Inc., USA) to remove the exposed buried SiO_2, and cleaning the sample of residual photoresist and crystal bond (used in ICP-DRIE process) via a descum process (March RIE) yielded 15 μm-thick slab of monocrystalline silicon with array of square holes (trenches).

Wafer bonding two wafers of SOI-A with a 15 μm-thick silicon trench involved spin-coating a layer of diluted poly(dimethylsiloxane) (PDMS, part A/part B/hexane = 10:1:100, Sylgard 184; Dow Corning, USA) at a speed of 3000 rpm for 30 seconds on each SOI-A, followed by sandwiching the silicon trench between the two SOI-A wafers. Pressing the wafers together in a steel vise (Toomaker's vise; Tormach, Inc., USA) and placing the vise in a 70 ^{o}C convection oven for 2 hours fully cured the PDMS, bonding the wafers. Heating the vise in a furnace, by raising the temperature to 550^{o}C over 2 hours and keeping there for 2 more hours, converted the PDMS adhesion layer to amorphous silica. Then, ICP-DRIE removed the top and bottom Si wafers of SOI-A of the bonded sample to expose buried oxide on both top and bottom sides. Wet etching in a buffered oxide etchant (BOE) removed the buried oxides, exposing Si NM diaphragms.

Integrating the resulting structure with a single-mode optical fiber (core diameter ~9 μm, cladding ~125 μm), connected with a tunable laser source (Agilent 8163B1; Agilent Technologies, USA), polarization-maintaining (PM) fiber, single-mode (SM) fiber and circulator, and photodetector completed the optical sensing system (Fig. 3.2). Procedures for fiber-sensor alignment involved positioning the SM fiber close to a flat surface of the device on regions surrounding the diaphragm, tuning fiber angle for the best FP profile, moving the fiber laterally for alignment on the diaphragm, verifying silicon and air FP resonances, applying UV-curable glue, and curing by exposing UV light. Connecting the laser source to Port 1 of the circulator and the sensor to Port 2 allowed monitoring of peak shift in the return loss spectrum. The returned optical intensity at Port 3 characterized the FP interference in the sensor's air cavity of which the thickness is subjected to the ambient pressure.

Fabrication of bioresorbable FP temperature sensor involved preparing a 15 μm-thick slab of monocrystalline silicon by removing Si wafer and buried oxide of SOI-B wafer by ICP-DRIE and wet etching in BOE, followed by integrating the resulting structure with a SM fiber.

Fabrication of bioresorbable photonic microcavity (PC) pressure sensor involved fabrication of the cavities on SOI-A wafer using electron-beam lithography, dry etching alignment marks through the wafer using ICP-DRIE process (to allow alignment of cavities over the trench during wafer bonding step), wafer bonding with silicon trench (dimensions: 250 μm x 250 μm x 10 μm) fabricated on SOI-B wafer using PDMS followed by calcination process, removal of Si wafers and thinning of buried oxides of SOI-A and SOI-B using ICP-DRIE followed by wet etching in BOE.

3.3 Results and Discussion

A fully bioresorbable Fabry-Perot (FP) pressure sensor consists of two nanomembranes of highly Phosphorous-doped (doping concentration ~10^{20} cm^{-3}) monocrystalline silicon that serve as pressure-sensitive flexible membranes that are bonded to a 15 μm-thick Si trench structure by adhesion interlayers of amorphous silica (Fig. 3.3a). Fabrication process involves wafer bonding of silicon-on-insulator (SOI) wafers of two different top silicon thicknesses (250 nm and 15 μm) using poly(dimethylsiloxane) (PDMS), followed by calcination at temperatures at 550 °C to convert PDMS to amorphous silica, and back-etching of Si wafers by deep reactive ion etching processes followed by wet etching in buffered oxide etchant to remove exposed buried oxides. Integrating the structure with single-mode (SM) optical fiber, connected with tunable laser source, circulator, polarization-maintaining fiber, and photodetector, allows pressure readout (Fig. 3.3b). Increase in surrounding air or fluid pressure pushes the membrane downward, which reduces the thickness of the air cavity in between the silicon membranes, leading to blue shift of the FP resonance signal, as observed from both simulation and experimental results (Figs. 3.3c and d).

Figure 3.4 shows results of mechanical and optical simulations, based on three-dimensional finite element analysis (3D-FEA) using ABAQUS software, which determines the deformation of the diaphragm at different surrounding pressures (Fig. 3.4a), and electromagnetic wave analysis using S4 software, which determines shift in the peak of the optical spectrum of the reflected laser at different center locations (Fig. 3.4b), respectively. As the pressure increases, the thickness of air layer underneath the diaphragm decreases. The destructive interference wavelength in the air cavity, indicated by the peaks in the return loss, shift to smaller wavelength due to the shortening in the light path length. The monotonic correlation of the ambient pressure

and the return loss peak provides an accurate measurement with high sensitivity at optimized design parameters.

Device structures and *in vitro* calibration curve for bioresorbable FP temperature sensor appear in Figure 3.5. The sensor consists of a 15 μm-thick slab of silicon connected with a SM optical fiber (Fig. 3.5a), and functions also as a FP interferometer, for which the peak wavelength of the optical spectrum red shifts linearly at a slope of 47.9 pm/^{o}C with respect to changes in surrounding temperature due to change in refractive index (thermo-optics effect; Fig. 3.5b).

Temperature sensing is critical in pressure measurement in the use of FP pressure sensor, as temperature affects the sensor performance significantly. Results of *in vitro* calibration of the pressure sensor indicate that the baseline (peak wavelength under atmospheric pressure) shifts linearly as a function of temperature with a slope of 11.9 nm/^{o}C (Fig. 3.6b). This is caused by expansion of the volume of air inside the cavity with rising temperature, which increases the length of air layer and affects the FP resonance signal. Figure 3.6c shows the pressure sensitivity (shift in peak wavelength per mmHg change in pressure) measured at different temperatures. No obvious trend is found, and the maximum error in sensitivity is ~7%.

In vivo monitoring of acute variations in intracranial pressure (ICP) and temperature (ICT) using bioresorbable FP sensors appears in Figure 3.7. The procedures for implanting the device as shown in Figure 3.7a includes opening a small craniectomy (~3 mm x 3 mm) on the skull and piercing open the dura mater, placing the sensor inside with diaphragm facing downwards, covering the top of the sensor with a biopolymer film, and sealing the gap between the cover and the skull using biodegradable glue.

A clinical ICP monitor probe implanted near the bioresorbable device allows calibration of the sensor *in vivo* (Fig. 3.7b and c), which involves squeezing rat's flank until the readings on clinical monitor stabilizes then collecting the optical spectrum from bioresorbable device. The design of the pressure sensor tested in the study illustrated in Figure 3.7a and b consisted of ~100 μm-thick air cavity and diaphragm consisting of 250 nm Si / ~1 μm SiO_2, which led to significantly reduced pressure sensitivity of -10.9 nm/mmHg. Temperature sensor calibration can be done in similar ways to yield a temperature responsivity of ~98 pm/^{o}C, which is within the observed ranges for fabricated devices (Fig. 3.7c and d).

Figure 3.8 illustrates another type of bioresorbable optical pressure sensor that relies on shifts in the returned resonance spectrum from an array of photonic crystal (PC) microcavities (diameter ~85 nm, separation between cavities ~1 μm) fabricated on the diaphragm. Changes in surrounding pressure deforms the diaphragm, which affects the distance between the PC cavities on the diaphragm, leading to shifts in the optical spectrum from reflected laser. Figure 3.8a illustrates materials and design of the bioresorbable PC pressure sensor, with light delivered via free-space detection mechanism from a distant laser. The design of the PC cavities located on the diaphragm are highlighted in the scanning electron microscopy (SEM) image in Figure 3.8b, an image obtained while the device is on the SOI wafer, prior to wafer bonding and back-etching procedures. Optical micrograph of the active region appears in Figure 3.8c. PC cavity array (outer square, area: 300 μm x 300 μm) sits over the air cavity (inner square, area: 250 μm x 250 μm).

For PC pressure sensor, the resonance spectrum red shifts in response to increasing pressure, as shown in Figure 3.8d. The pressure sensitivity is 1.9 pm/mmHg, which is significantly smaller compared to that of a FP device, for reasons of ease with which the

membrane can move vertically as opposed to expand laterally. Figure 3.8e shows optical set-up used for *in vitro* sensor calibration. While PC- and FP-based bioresorbable pressure sensors are both feasible, FP devices have advantages of simpler fabrication procedures (does not require e-beam lithography, align mark etching steps) and higher responsivity to pressure. Light delivery and collection through integrated optical fiber also has advantages over free-space detection method used here as it allows more freedom of movement for the sensor (no need to align laser onto diaphragm for measurement) and also is unaffected by concerns of loss of light intensity when the light travels through water, which makes collecting signals from PC devices deployed in watery environments of the body difficult.

Complete disintegration in biofluids into biologically benign end products is key characteristic of bioresorbable implants. Layers of silicon and silicon dioxide, which make up the FP and PC devices demonstrated in this study, are known to degrade in water via hydrolysis to yield silicic acid $Si(OH)_4$. Figure 3.9 shows the set-up (left) and optical micrographs (right) of a FP pressure sensor collected at various stages of accelerated dissolution by immersing in PBS at 95 ^oC. Highly doped silicon nanomembrane dissolve away within 3 hours, followed by amorphous silica bonding layer in 6 hours, followed by the 10 μm-thick silicon trench within 60 hours. Complete disappearance yields thermal SiO_2 substrate with a slight relief feature.

Figure 3.10 shows effects of silicon nanomembrane dissolution on PC resonance signals of a PC cavity device fabricated on SOI wafer. Figure 3.10a shows SEM images of the cavities before and after immersion in PBS (pH ~7.4, 85^oC) for 30 minutes, indicating rough surface profile. The resonance spectrum also blue shifts linearly, matching the decrease in silicon nanomembrane thickness as determined from SEM (Fig. 3.10b).

3.4 Conclusion

Bioresorbable optical implants for intracranial pressure and temperature sensing and light delivery have potential for wide clinical application replacing conventional electronic implants that are susceptible to electromagnetic interference and normal/leakage current flow that may cause local thermal damage to the biological structure. *In vitro* and *in vivo* calibration results verify the accuracy of these sensors. Accelerated dissolution experiments demonstrate transience of the sensors, waveguides, and polymers. Future studies will aim to identify long-term stability of optical pressure and temperature monitoring *in vivo* and develop strategies to integrate bioresorbable optical sensors with waveguides/fibers to build fully bioresorbable optical sensing platform. The device structures and materials studied here may also serve as platform for development of other types of clinically useful bioresorbable optical sensors and actuators.

3.5 Figures

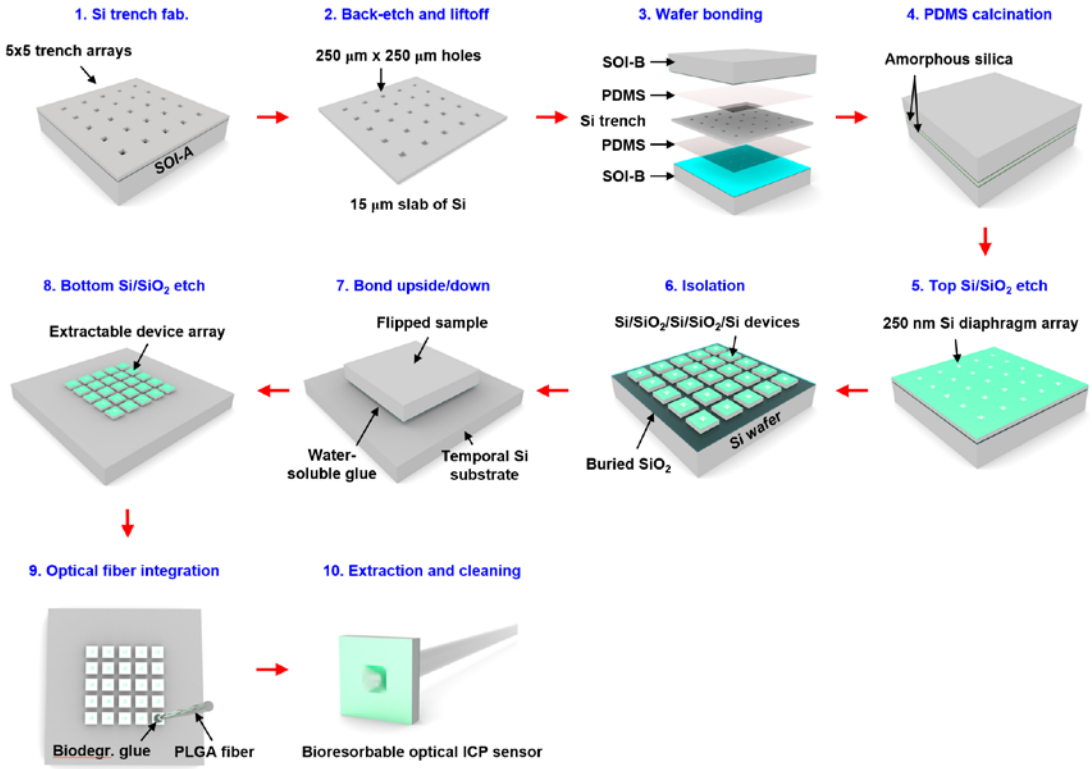

Figure 3.1 Fabrication procedures for bioresorbable Fabry-Perot pressure sensors integrated with commercial optical fibers.

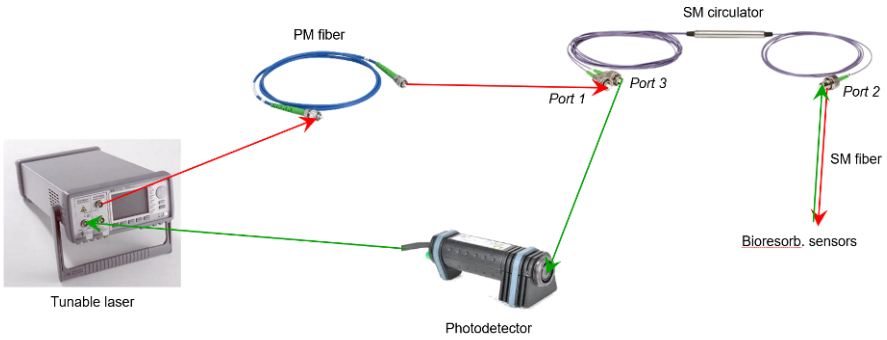

Figure 3.2 Optical set-up for bioresorbable Fabry-Perot pressure and temperature sensors integrated with commercial optical fibers. Consists of tunable laser source, polarization-maintaining (PM) optical fiber, single-mode (SM) optical fiber and circulator, and photodetector. Red and green arrows indicate incoming and returning light paths, respectively.

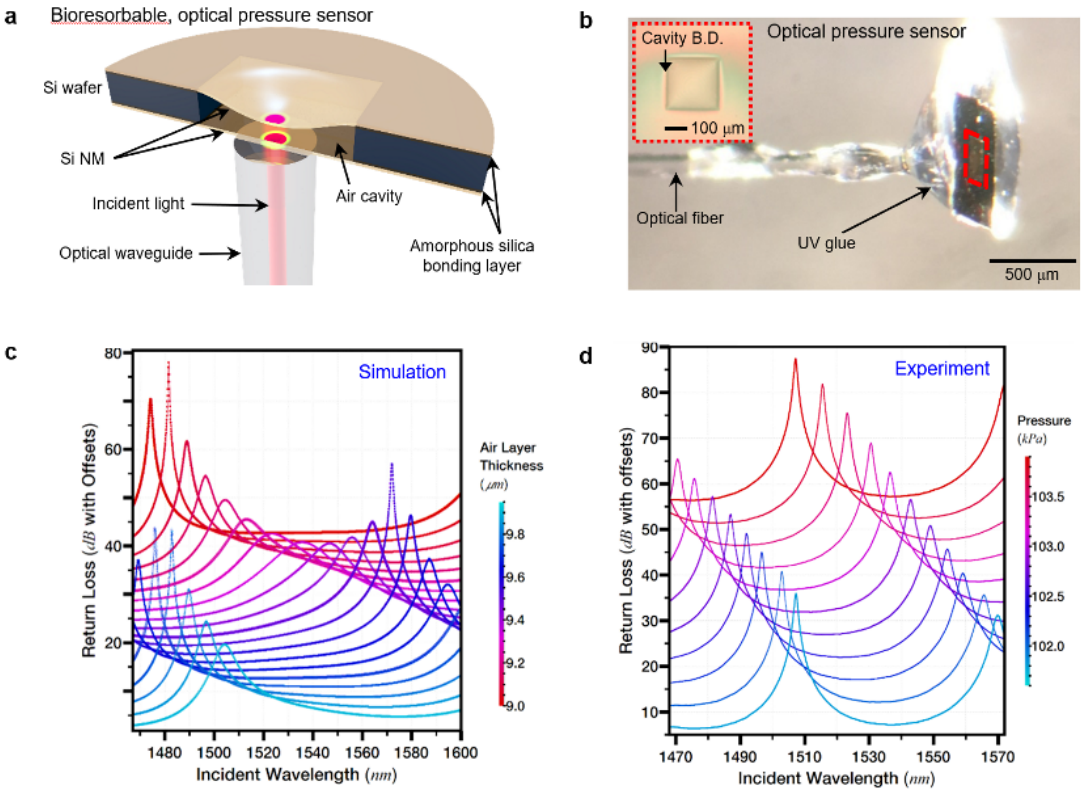

Figure 3.3 Bioresorbable Fabry-Perot pressure sensor integrated with single-mode optical fiber. a, Schematic illustration of the pressure sensor integrated with optical fiber via UV-curable glue. b, Photograph of the sensor. Inset: optical micrograph of the sensing silicon nanomembrane diaphragm. c, Simulated return spectrum of the Si pressure sensor as the air layer thickness changes by S4 software. d, Experimentally obtained (at constant surrounding temperature) spectrum of fiber integrated Si pressure sensor in response to pressure change.

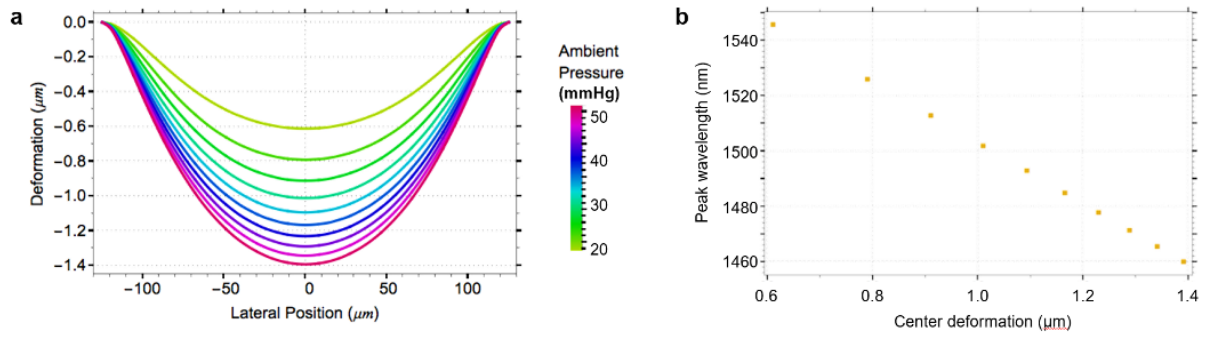

Figure 3.4 Mechanical and optical simulation of bioreosrbable Fabry-Perot pressure sensor. a, Simulation of diaphragm deflection at various pressures based on three-dimensional finite element analysis (3D-FEA) using ABAQUS software. b, Simulation of the peak wavelength extracted from the Fabry-Perot resonance return loss spectrum at different membrane deformations using S4 software.

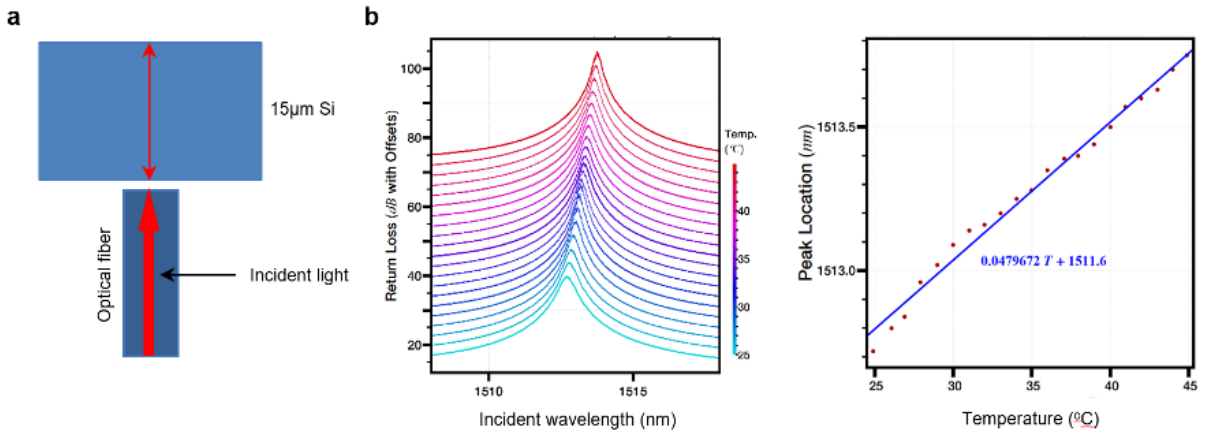

Figure 3.5 Bioresorbable Fabry-Perot temperature sensor based on thermo-optics effect of silicon. a, Schematic illustration of the sensor, consisting of a 15 μm-thick slab of monocrystalline silicon, aligned and bonded with an optical fiber. b, Fabry-Perot resonance signals collected by the sensor, indicating red shift of the peak with increasing temperature.

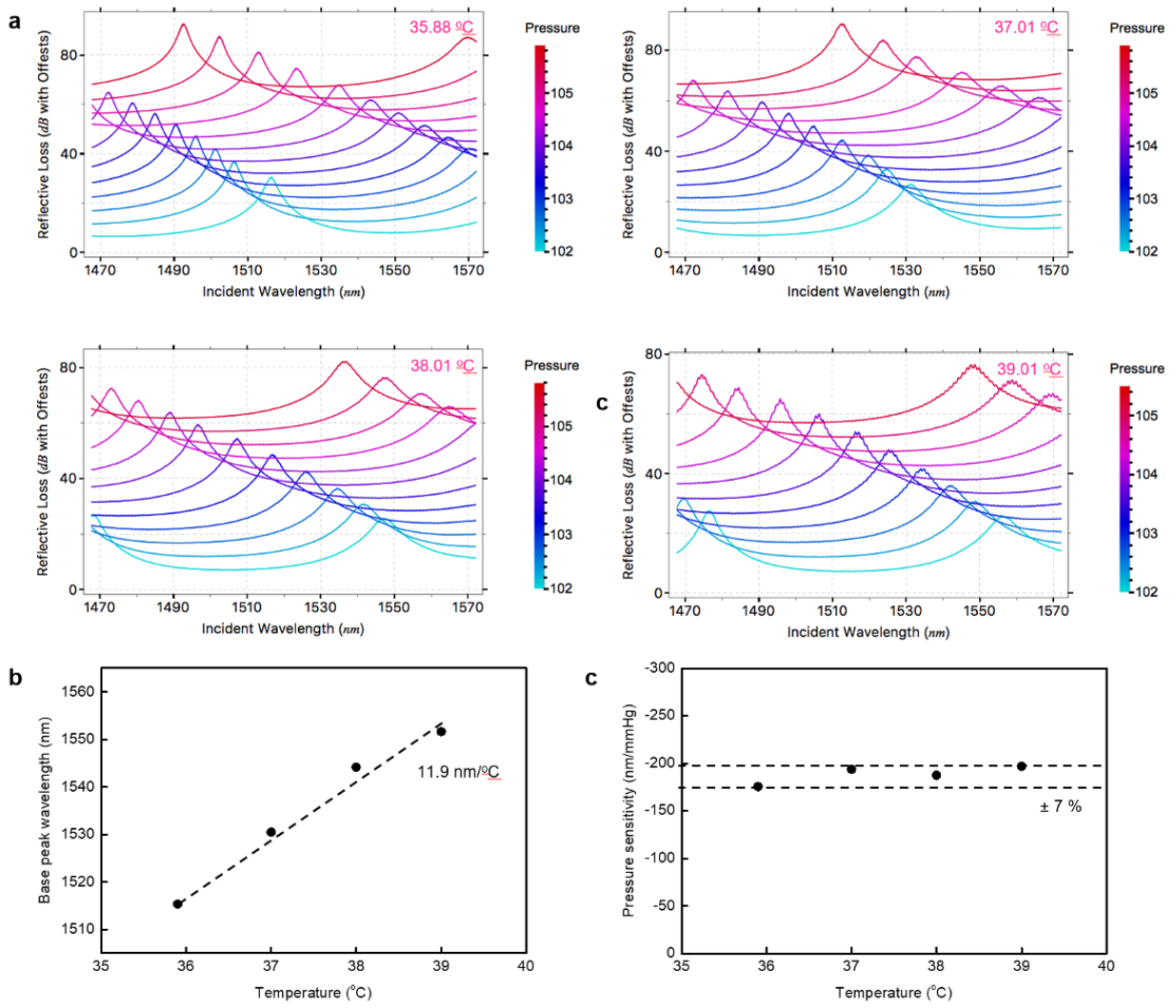

Figure 3.6 *In vitro* calibration of bioresorbable pressure sensor in phosphate buffered saline (PBS, pH ~7.4) at different temperatures. a, Resonance spectra collected at various sets of pressures and temperatures within PBS solution. b, Peak wavelength of the sensor under atmospheric pressure at various temperatures, indicating red shift of the baseline at linear slope of 11.9 nm/^{o}C. c, Pressure sensitivity (shift in peak wavelength as a function of pressure) at different temperatures.

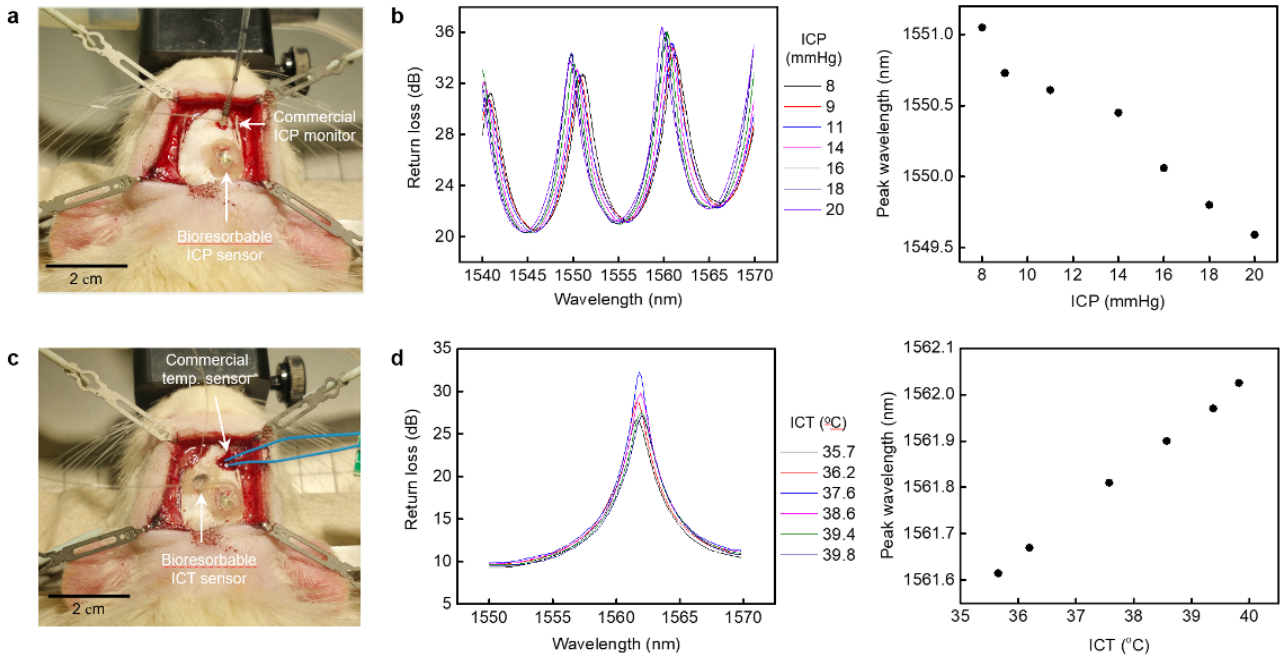

Figure 3.7 *In vivo* monitoring of intracranial pressure (ICP) and temperature (ICT) using bioresorbable optical sensors. a, Photograph of bioresorbable and commercial ICP sensors (reference) implanted in the subdural space. b, Fabry-Perot resonance signals and pressures collected by both devices while raising ICP by squeezing the flank. The sensor used in this study has 100 μm-thick air cavity and diaphragm consisting of 250 nm Si/~1 μm SiO_2. c, Photograph of bioresorbable and commercial ICT sensors implanted alongside a bioresorbable ICP sensor. d, Fabry-Perot resonance signals and temperatures collected while raising ICT by covering the rat's body with electrical heating blanket.

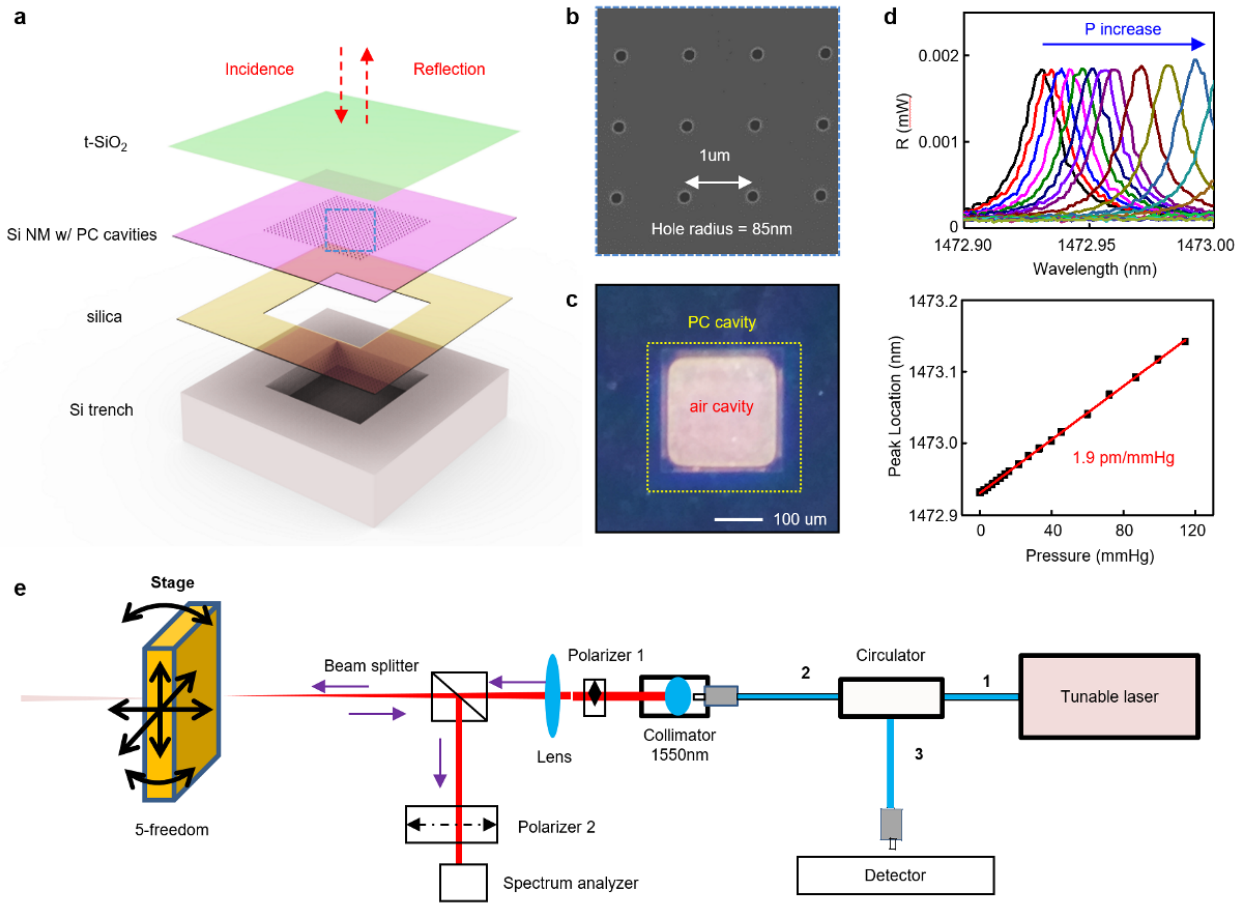

Figure 3.8 Bioresorbable optical pressure sensor based on photonic crystal (PC) microcavities. a, Schematic illustration of the device structures, indicating an array of PC cavities in the diaphragm. b, Scanning electron microscopic (SEM) image of the cavities fabricated on a silicon-on-insulator wafer, prior to wafer bonding and back-etching of Si wafer. c, Photograph of the diaphragm region. d, Optical spectrum from reflected laser (top), indicating red shift of the peaks with increasing pressure in highly linear fashion (bottom). e, Experimental set-up for device calibration.

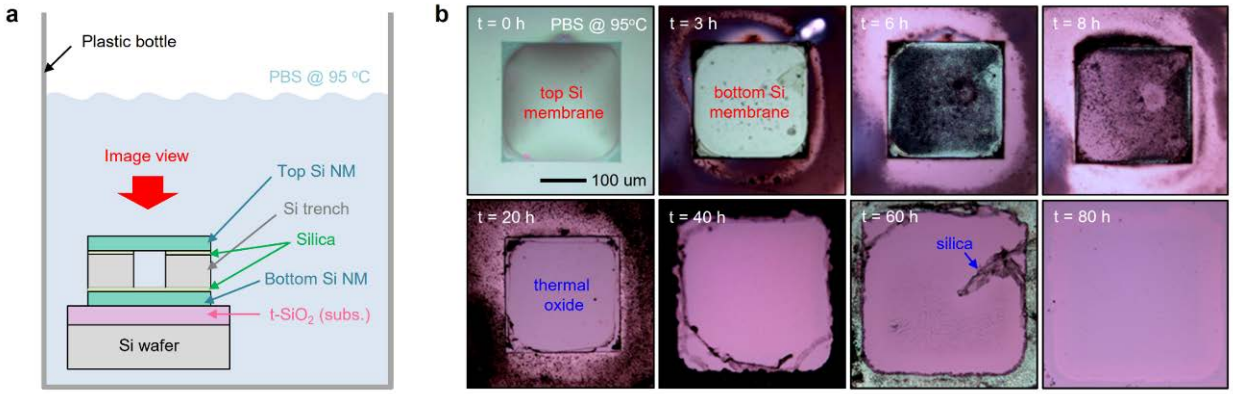

Figure 3.9 Dissolution of bioresorbable optical pressure sensor. a) Schematic illustration of the dissolution experiment set-up. b) Optical micrographs of bioresorbable optical pressure sensor at various stages of accelerated dissolution in phosphate buffered saline (PBS, pH 7.4) at T = 95ºC.

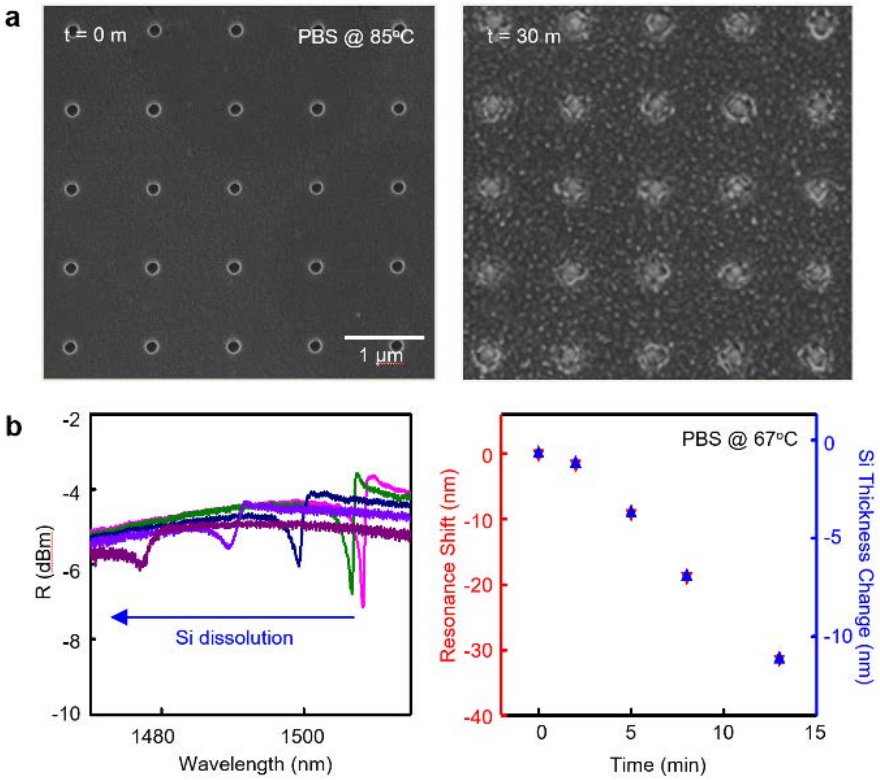

Figure 3.10 Dissolution of silicon photonic crystal microcavities fabricated on SOI wafer in phosphate buffered saline (PBS, pH ~7.4). a, Scanning electron microscopy (SEM) images of the device before (left) and after (right) dissolution in PBS at 85°C for 30 minutes. b, Blue shift of the optical spectrum with decrease in thickness of the silicon nanomembrane (left). Peak shift and silicon nanomembrane thickness as functions of time (right).

3.6 References

1 Kang, S.-K. *et al.* Bioresorbable silicon electronic sensors for the brain. *Nature* **530**, 71 (2016).

2 Hwang, S.-W. *et al.* Biodegradable Elastomers and Silicon Nanomembranes/Nanoribbons for Stretchable, Transient Electronics, and Biosensors. *Nano Letters* **15**, 2801-2808 (2015).

3 Yu, K. J. *et al.* Bioresorbable silicon electronics for transient spatiotemporal mapping of electrical activity from the cerebral cortex. *Nature Materials* **15**, 782 (2016).

4 Lee, G. *et al.* Fully Biodegradable Microsupercapacitor for Power Storage in Transient Electronics. *Advanced Energy Materials* **7** (2017).

5 Lee, C. H. *et al.* Wireless Microfluidic Systems for Programmed, Functional Transformation of Transient Electronic Devices. *Advanced Functional Materials* **25**, 5100-5106 (2015).

6 Hwang, S.-W. *et al.* A Physically Transient Form of Silicon Electronics. *Science* **337**, 1640-1644 (2012).

7 Sawyer-Glover, A. M. & Shellock, F. G. Pre-MRI Procedure Screening: Recommendations and Safety Considerations for Biomedical Implants and Devices. *Journal of Magnetic Resonance Imaging* **12**, 92-106 (2000).

8 Ellingsen, J. E. & Lyngstadaas, S. P. *Bio-Implant Interface: Improving Biomaterials and Tissue Reactions*. (CRC Press, 2003).

CHAPTER 4: PERSPECTIVE

4.1 Summary

Recent literature highlights bioresorbable implantable device technology, as a subset of a larger field known as ‘Transient electronics’, for which all of the constituent materials dissolve in biofluids at controlled rates to form biologically benign end products. Bioresorbable devices can reduce costs, patient distress, and risks of complication associated with surgical elimination procedures after useful timeframe, and they also minimize chances of infection or immune-mediated tissue reactions, all of which are associated with conventional standard permanent hardware. In this study we demonstrated materials, device structures, fabrication approaches, and encapsulation strategies for bioresorbable intracranial pressure sensors for treatment of traumatic brain injury or hydrocephalus. Our results on *in vivo* biodistribution and biodegradability of the devices, as well as *in vitro* and *in vivo* demonstrations of their use in monitoring of intracranial pressure highlight the key features and capabilities. We also proposed optical pressure sensors based on principles of Fabry-Perot interferometry as next type of bioresorbable implant that can avoid issues of MRI compatibility and damage due to normal or leakage current flow, which are inherent to implantable electronic sensors.

4.2 On-going/Future Work

Currently we continue to build on bioresorbable optical sensor research, to develop a fully bioresorbable optical pressure sensing systems by fabricating bioresorbable optical waveguides and fibers based on silicon nanomembranes or PLGA to replace the commercial non-resorbable optical fibers used in Chapter 3. Results of these on-going efforts appear below.

Bioresorbable Silicon Optical Waveguides

Schematic illustration of fabrication process of bioresorbable silicon optical waveguides appears in Figure 4.1. The process begins with photolithography on SOI substrates (top Si ~200 nm, buried oxide ~1 μm, Si wafer ~500 μm; SOITEC, France) using a MA/BA6 mask and bond aligner (SUSS MicroTec AG) (Fig. 4.1a) and positive photoresist AZ5214 (thickness 1.6 μm, Microchem). Subsequently, reactive ion etching process (Plasma-Therm RIE) removes the top silicon layer in regions not protected by the photoresist. Immersion in hydrofluoric acid (HF, 49%; J.T. Baker, Inc, USA) for 2 min partially undercuts the buried oxide layer (Fig. 4.1b). Spin-coating a layer of positive photoresist (PR, S1813, MicroChem Corp., spin condition: 4000 rpm with ramp 500 rpm/s for 30 s), flood exposing to ultraviolet light (10 mW/cm^2 for 12 s) followed by immersion in a developer (MF319, MicroChem, for 30 s) removes the PR everywhere except beneath the m-Si at the perimeter, partially undercut regions (Fig. 4.1c). The residual PR serves as anchor to tether the m-Si structure to the underlying substrate during the subsequent immersion into HF for 3 hours to fully undercut the m-Si (Fig. 4.1d).

A PDMS stamp allows retrieval of the m-Si structure from the source substrate, in a manner that exposed the backside to allow removal of residual photoresist by immersion in acetone. The PDMS stamp enables delivery of the m-Si onto a poly(lactic-co-glycolic acid) (PLGA) layer heated at 55^{o}C on a hotplate (Fig. 4.1e). This PLGA layer (10 μm thick) forms from slowly drying a solution of this material onto a hydrophobic surface prepared by immersion of a Si wafer into 5 vol% trimethoxymethylsilane in hexane for 30 min followed by rinsing with DI water. Another layer of PLGA (10 μm thick) laminated on top and then annealed by exposure to ethyl acetate vapor for 30 minutes (Fig. 3.2f) enables bonding to the underlying PLGA,

thereby encapsulating the m-Si waveguide. Finally, a laser milling process defines strips of PLGA with widths of 1 mm and the m-Si in the center.

Figure 4.2 illustrate a hybrid integration of silicon nanomembranes (Si NMs) with other organic and inorganic bioresorbable materials, which offers high performance, flexible electronic and photonic systems with proven biocompatibility and clinically relevant modes of operation, as an emerging type of biomedical implants that disappear, without risk to the patient, after a relevant operational time period. The technology of bioresorbable waveguides relies on methods including wafer-based microfabrication, transfer printing and polymer processing, for forming long, thin filamentary structures of monocrystalline Si from patterns in Si NM design to unfurl from dense, planar coiled layouts (Figs. 4.2a and b). The addition of a bioresorbable polymer as a cladding layer, offers extended, mechanically flexible, bioresorbable waveguides with extremely low propagation losses even when embedded in biological tissues. Figure 4.2c shows an image taken by infrared camera, which reveals near-infrared light (wavelength: 1550 nm) propagating through a waveguide (thickness 1.5 μm, width 50 μm).

Figure 4.3 shows photos and changes in intensity of transmitted light through silicon optical waveguide with PLGA cladding immersed in PBS at 70^{o}C, indicating complete dissolution within 10 days and linear decrease in light intensity throughout the dissolution process.

Biopolymer Optical Fiber

Bioresorbable optical fibers can form from biopolymers such as poly(D,L-lactide-co-glycolide) (PLGA) and poly(L-lactic acid) (PLA), which offer wide usage in conventional implantable devices and injectable products including bioresorbable sutures. Fabrication of

PLGA optical fibers is based on a thermal drawing process, which involves melting PLGA polymer crystalline powders at about 220°C, drawing out as fibers, and cooling down soft polymer fibers to allow crystalline-to-amorphous phase transition. Manipulation of drawing speed controls fiber diameters, optimized at about 220 μm for connection with standard optical measurement setups for biological research.

Figure 4.4 shows a photograph of a PLGA optical fiber with about 220 μm diameter. The cylindrical fiber structure serves as a waveguide with guided photons undergoing total internal reflection at interfaces between the PLLA polymer (refractive index n = 1.47 and transparent in the visible ranges) and outer media, such as air (n = 1.0), dermal tissues (n = 1.38–1.44), and brain tissues (n = 1.36–1.42). The 220 μm diameter Bioers can be coupled with ceramic ferrules and linked to external laser and/or light-emitting diode (LED)-based light sources. Figure 4.5 shows process of dissolution for PLGA optical fiber, with working time of around 2 days and full dissolution time of around 3 weeks.

Integration with Pressure Sensor

The next step in the development of a fully bioresorbable, optical sensing system involves integration of bioresorbable optical waveguides and fibers with pressure sensors. These efforts may require development of grating couplers to enhance transmission efficiency at the fiber-sensor interface, and use of bioresorbable polymers as adhesives to hold them together throughout their use. We're also searching for ways to realize wireless pressure monitoring, by improving the design of optical sensors to be less sensitive to incident angle of laser, which if possible would greatly enhance their applicability. A proposed future direction for electronic sensors include development of fully wireless sensing schemes, enabled by use of passive RF

circuits, and applying these platforms in other biological spaces such as the eye to demonstrate their biomedical utility.

4.3 Figures

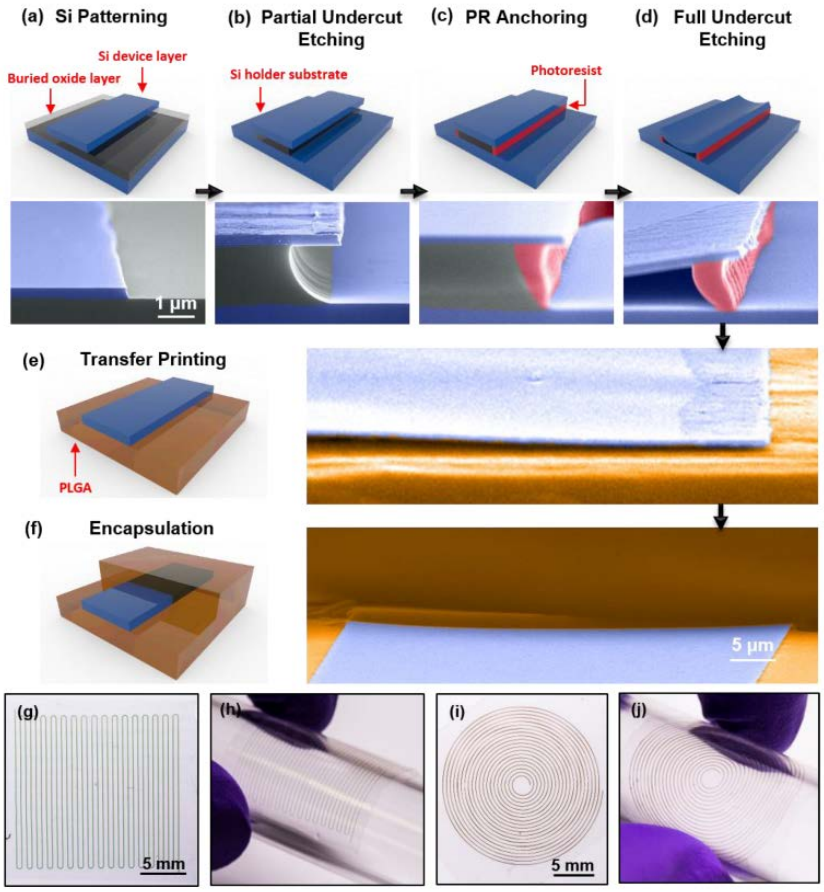

Figure 4.1 Schematic illustrations and colorized SEM images of the steps for fabricating flexible silicon transient optical waveguides. a, Photolithography and reactive ion etching define Si filamentary waveguides from the Si device layer (200 nm thick) of a silicon-on-insulator substrate. b, Controlled etching using hydrofluoric acid consumes the exposed buried oxide (BOX) layer and partially undercuts the BOX layer underneath the edges of the waveguides. c, Spin coating a positive photoresist (PR), flood exposing and inserting the substrate into a developer leaves a thin strip of PR underneath the edges of the waveguides. d, Further etching removes the remaining BOX layer, thereby leaving the waveguides supported only by the PR structures. e, A PDMS stamp allows retrieval of the waveguides and exposure of their back sides such that immersion in acetone eliminates any residual PR. Physical transfer integrates the waveguides onto a layer of PLGA. f, Lamination of another layer of PLGA on top and exposure to solvent vapors of ethyl acetate seals the PLGA layers to thereby encapsulate the waveguide. g,h, Optical images of a zigzag waveguide with 32 turning corners. The thickness, width and contour length of the Si core are 200 nm, 50 µm and 72.6 cm, respectively. i, j, Optical images of a spiral waveguide with base radius 1 mm, top radius 1 cm, and 20 turns. SEM images of (a)-(e) share the same scale bar. The colorized regions in the SEM images correspond to silicon (blue), buried oxide (gray), photoresist (red), and PLGA (brown).

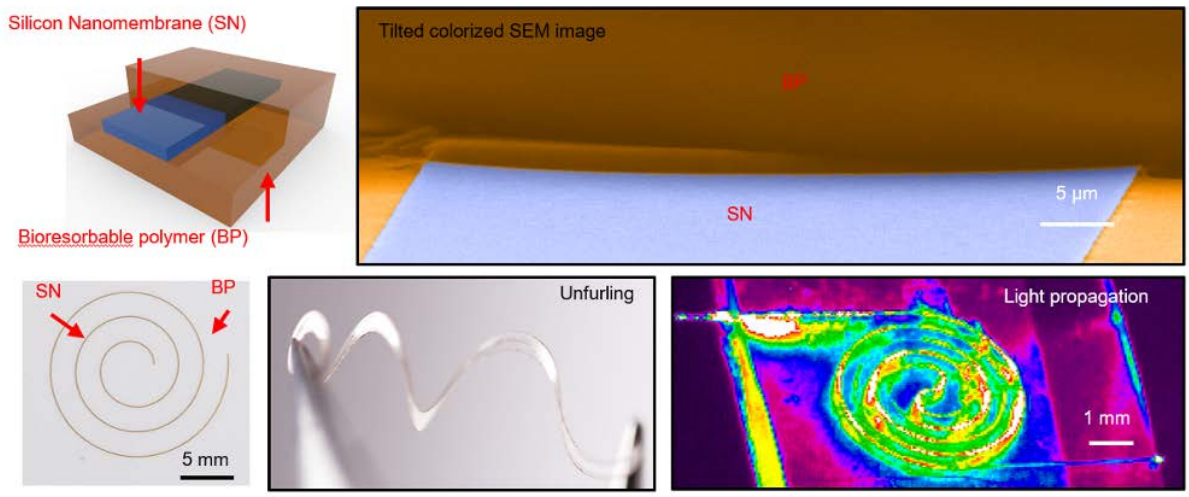

Figure 4.2 Bioresorbable optical waveguide consisting of filamentary silicon nanomembrane as core and PLGA as cladding. a, Schematic illustration (left) and colored scanning electron microscope (SEM) image of the device. b, Photograph of waveguide in normal (left) and unfurled (right) states, demonstrating high flexibility. c, Infrared image indicating light propagation through the waveguide.

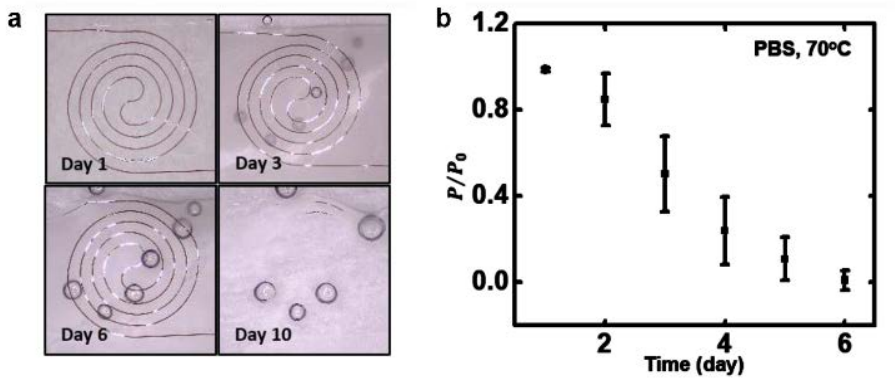

Figure 4.3 Dissolution of bioresorbable silicon waveguides with PLGA cladding in PBS at 70ºC. a, Photographs of the device indicating complete hydrolysis of silicon filaments within 10 days. b, Optical measurements of the waveguide through the dissolution process. P: measured output intensity, P_o: output intensity on day 1.

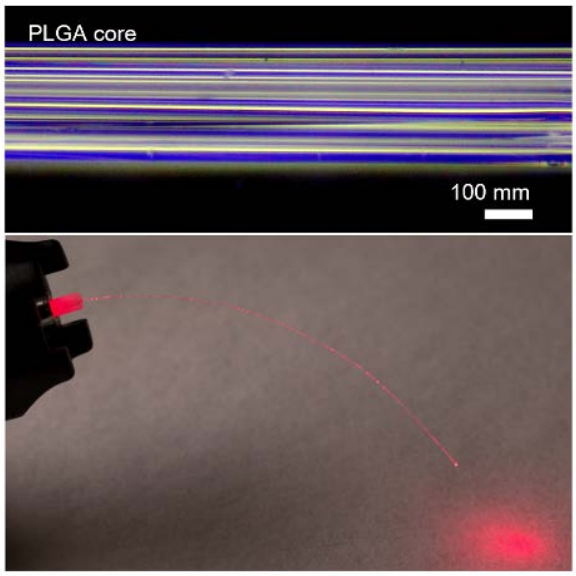

Figure 4.4 Bioresorbable optical fiber made of poly(lactic-co-glycolic acid) (PLGA). Optical microscopy image of PLGA fiber (top). Light transmission through PLGA fiber at light wavelength of 633nm (bottom).

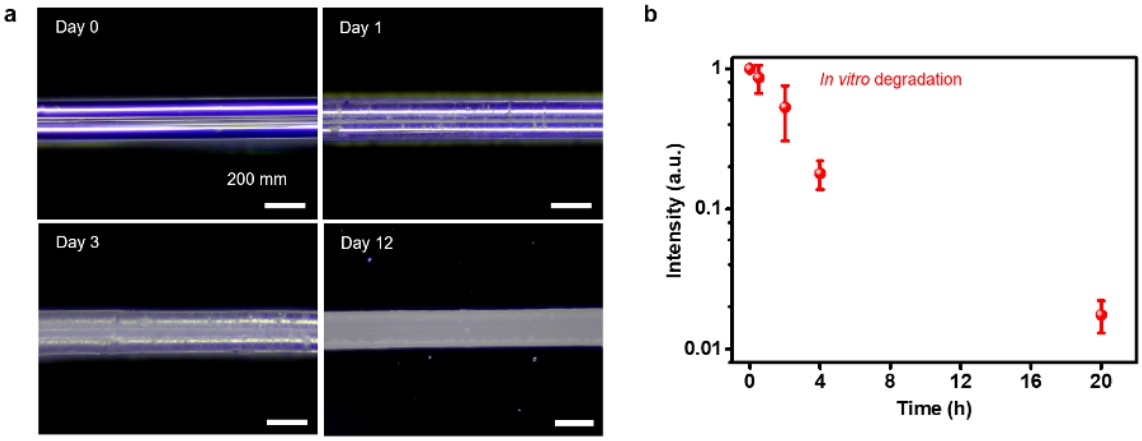

Figure 4.5 Dissolution of bioresorbable PLGA optical fiber. a, Optical images of PLGA fiber at various stages of dissolution in phosphate-buffered saline (PBS, pH~7.4, 37 ^{o}C). b, Intensity of transmitted light through the PLGA fiber in PBS at 37^{o}C. The transmission intensity decreases as the PLGA dissolves.